POLITECNICO DI MILANO

SCHOOL OF INDUSTRIAL AND INFORMATION ENGINEERING

MASTER OF SCIENCE IN AERONAUTICAL ENGINEERING

SCALE – RESOLVING SIMULATION METHOD APPLIED TO WIND TURBINE AIRFOIL EQUIPPED WITH CROPPED – DELTA VANE VORTEX GENERATORS

Supervisor : Prof. Riccardo MEREU

Master thesis of :

Teodor BABIĆ Matr. 840988

Accademic Year 2020 – 2021

Teodor Babić : *Scale - Resolving Simulation Method Applied to Wind Turbine Airfoil Equipped with Cropped – Delta Vane Vortex Generators* | Master of Science in Aeronautical Engineering,
Politecnico di Milano

Politecnico di Milano :
www.polimi.it

School of Industrial and Information Engineering :
www.ingindinf.polimi.it

Acknowledgments

Big thanks goes to professor Riccardo Mereu for alowing me to adress this specific topic and his assistance for the duration of the thesis. I also thank to CFDLab that permitted me to use the available calculation resources, regardless of the physical distance.

I am by far mostly grateful to God, who gave me the kind of family who were always on my side, no matter what, whose patience and time were always at my disposal, who always trusted me and had the understanding for any of my actions, not just for the duration of my thesis, but the whole degree time in Italy which wasn't short for sure. I was also surrounded by friends who turned out to be just the right people for me at just the right time and their appearance and company I know were direct gifts from God.

Хвала Вам.

Milan, July 2021 T. B.

Abstract

Global energetic sector has witnessed significant rise in exploatation of renewable energy sources in the last thirty years, where a notable portion occupies wind energy domain. The trend continues to grow, implying further developments in wind turbine design that is most evidently displayed by wind turbine dimensions, i.e. blade length. As blades become longer, maintaining the same aerodynamic performance in turbine root section becomes even more challenging. Consequently, drastic attention is directed towards airfoil design, the study of flow control devices and corresponding CFD simulation tools.

Most basic division of flow control devices is passive and active. While the latter enables highly appealing performance improvements, the need for energy source and controlling mechanisms poses an unavoidable drawback. In the field of passive control devices, arrays of vortex generators often represent the most economical option and extensive theoretical background is provided to give an insight of underlying physical mechanisms. Consequently, it is possible to determine the optimal choice in terms of geometry, dimensions and positioning of vortex generators on an aerodynamic surface.

CFD simulation is conducted for wind turbine airfoil DU 97 – W – 300 equipped with cropped – delta vortex generators in counter – rotating, common – downwash orientation. Simulation is performed for higher angles of attack, at Reynolds number $2 \cdot 10^{6}$, in condition of free boundary layer transition. Employed turbulence solver is Shielded Detached Eddy Simulation, a member of Scale – Resolving Simulation methods, in combination with $k - \omega$ SST and Transition SST models. Comparison of results from different turbulence models and span sensitivity analysis is carried out, before composing the resulting lift and drag curves. Postprocessing is mostly focused on flow differences between common – downwash cropped – delta array and previously simulated common – upwash delta vortex generators, proving the superiority of the former in terms of separation alleviation and stall delay.

Keywords : CFD, SRS, SDES, Wind energy, Passive control devices, Vortex generators

Nomenclature

α – Angle of attack

α_{crit} – Critical angle of attack

β – Inflow or incidence angle of vane vortex generator

γ – intermittency

μ – Dynamic viscosity coefficient

μ_t – Turbulence or ’eddy’ viscosity coefficient

ν – Kinematic viscosity coefficient

ρ – Density

σ – Prandtl number

τ_{ij}^{LES} – Sub – grid shear stress tensor

τ_{ij}^{t} – Turbulence or Reynolds shear stress tensor

ω – Specific dissipation rate of turbulence kinetic energy or turbulence frequency

b – Geometry span length

c – Airfoil chord length

d – Intra – vane spacing

h – Vane height

k – Turbulence kinetic energy

p - Pressure

u_i – Velocity component

v_∞ - freestream velocity

C_D – Drag coefficient

C_L – Lift coefficient

C_N – Normal force coefficient

C_T – Tangential force coefficient

D – Inter – vane spacing

L – Vane length

L_t – Turbulence length scale

M – Mach number

Re – Reynolds number

$\overline{Re}_{\theta,t}$ – Momentum – thickness Reynolds number

U_i – Reynolds – averaged velocity component

Acronyms

AJVG – Air Jet Vortex Generator
AoA – Angle of Attack
APG – Adverse Pressure Gradient
AR – Aspect Ratio
AVATAR – AdVanced Aerodynamic Tools for lArge Rotors (European Project)
BC – Boundary Condition
BL – Boundary Layer
CAS – Chinese Academy of Sciences
CD – Common – Downwash
CFD – Computational Fluid Dynamics
CoR – Co – Rotating
CtR – Counter - Rotating
CU – Common – Upwash
DDES – Delayed – Detached Eddy Simulation
DES – Detached Eddy Simulation
DNS – Direct Numerical Simulation
DU – Delft University
ELES – Embedded Large Eddy Simulation
FMG – Full MultiGrid
FPG – Favourable Pressure Gradient
FVM – Finite Volume Method
GIS – Grid – Induced Separation
LES – Large Eddy Simulation
MEMS – Micro – ElectoroMechanical System
NACA – National Advisory Committee for Aeronautics

NREL – National Renewable Energy Laboratory

PDE – Partial Differential Equation

PIV – Particle Image Velocimetry

RANS – Reynolds – Averaged Navier – Stokes

RSM – Reynolds Stress Model

RVG – Rod Vortex Generator

SAS – Scale Adaptive Simulation

SBES – Stress – Blended Eddy Simulation

SBVG – Sub – Boundary layer Vortex Generator

SDES – Shielded Detached Eddy Simulation

SIMPLEC – Semi – Implicit Method for Pressure Linked Equations – Consistent

SRS – Scale – Resolving Simulation

SST – Shear Stress Transport

TBL – Thermal Boundary Layer

URF – Under – Relaxation Factor

VBL – Velocity Boundary Layer

VG – Vortex Generator

VGJ – Vortex Generator Jet

WALE – Wall – Adapting Local Eddy - viscosity

WMLES – Wall – Modeled Large Eddy Simulation

ZLES – Zonal Large Eddy Simulation

ZPG – Zero Pressure Gradient

List of Figures

List of Tables

Contents

Introduction

Renewable energy sources have captured a special spot inside many international debates on global energy production and consumption in the last couple of decades. Renewable energy became the world’s fastest growing exploitation source, driven by rising electricity demand and economic policies of many countries. According to International Energy Outlook 2019 with projections to 2050 [1], worldwide renewable energy consumption should increase by 3% per year between 2018 and 2050.

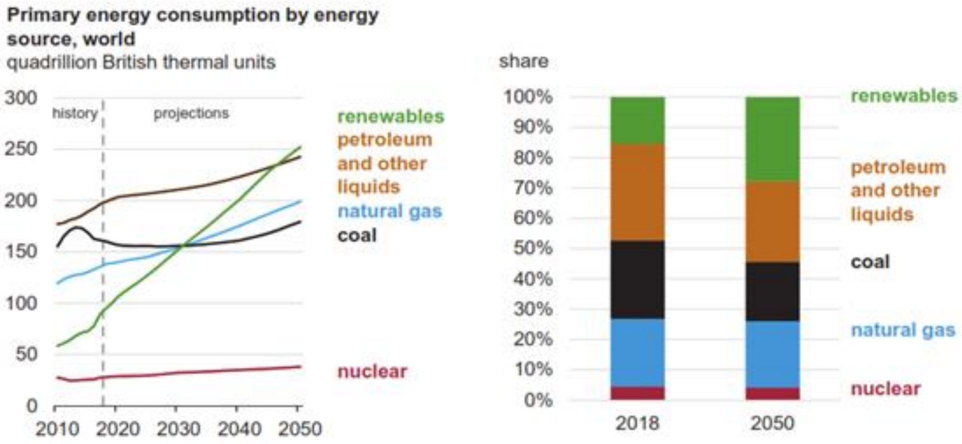

Figure 1 : Predictions of various energy sources consumption

In particular, electricity generation by wind and solar energy facilities should increase the most between 2018 and 2050, reaching 6.7 trillion and 8.3 trillion kWh, respectively, as these technologies become more cost competitive and ensure government supports. By 2050, wind and solar energy might account for over 70% of total renewables generation and surely represent a promising concept from engineering point of view.

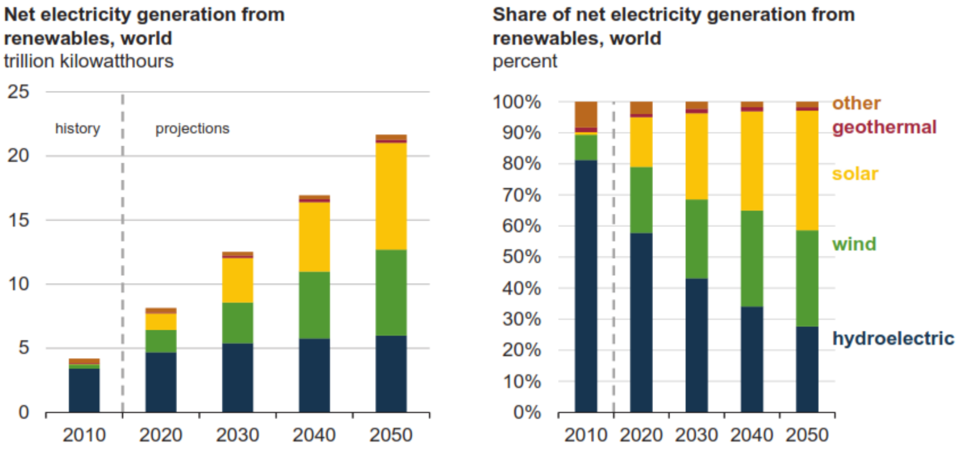

Figure 2 : Predictions of net electricity generation from renewable sources

The size of offshore wind turbines is expected to grow in size in an effort to take advantage of higher winds and achieve greater energy output by increasing swept area of the rotor. State – of – the – art wind turbines exceed 120m in diameter and represent massive challenge for today's standards. However, even larger turbines have been announced that should extend to 150 m in diameter and more, reaching nominal capacity of 10 MW.

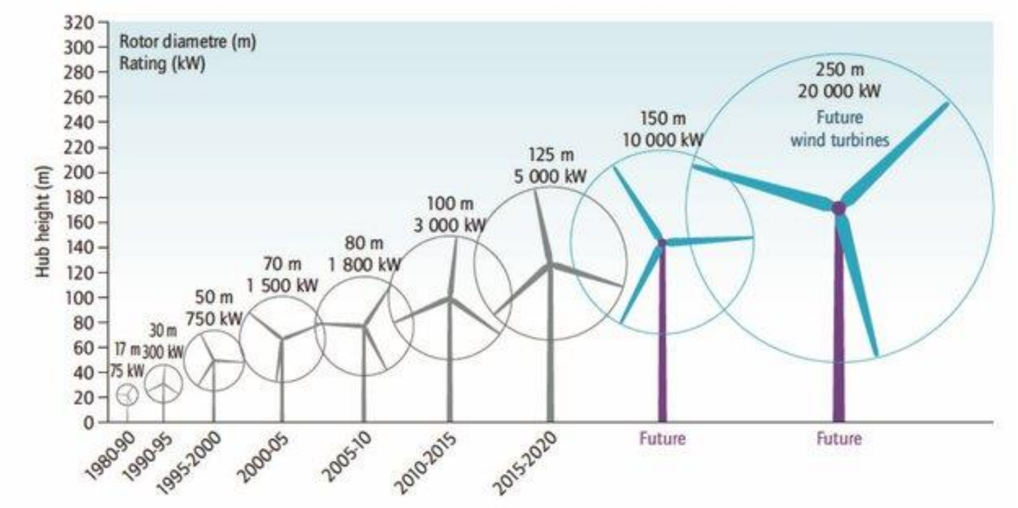

Figure 3 : Evolution of wind turbine size and future prospects

In addition to greater energy output, contribution to overall structural load is inevitable. Huge bending and twisting moments are encountered at blade – hub connecting segment, therefore, blade root section is composed of drastically thick airfoils. This makes the section prone to severe flow separation in the form of blade stall. Such phenomena manifest by notable lift drop and rise in drag force, causing a decrease in torque and turbine power output, additional structural and fatigue loads as well as noise pollution. As longer blades are expected in the near future, an even worse aerodynamic performance should not surprize anyone. In order to combat flow separation problems, flow control strategy is of utmost importance.

Although wind tunnels are well – known and broad aerodynamic testing facilities, they are a very time consuming and expensive option. On the other hand, numerical modeling of wind turbine airfoils comes as a relatively fast and economic choice, allowing more freedom for design alterations in preliminary design phase, but keeping in line with the actual, real – world physics of the flow.

Thesis objective and summary

Objective of the thesis is to conduct a theoretical study of state – of – the – art passive flow control devices and subsequent CFD simulation of flow around wind turbine airfoil DU 97 – W – 300, equipped with cropped – delta vortex generators. Ideally, passive control devices should be in line with optimal VG configuration that is previously determined from theoretical investigation. However, no experimental study of such configuration is available and choice must fall on the closest configuration for which experimental data do exist. Emphasis is put on critical and near – critical angles of attack, as those are best used to describe the development of massive flow separation. Adopted boundary layer regime is free or natural transition and Reynolds number is $2 \cdot 10^6$. Selected turbulence solver is Shielded Detached Eddy Simulation (SDES), combined with $k - \omega$ SST and Transition SST models, contrary to the usual practice of employing only the former when fully turbulent regime is imposed.

Brief summary of all chapters in the thesis is the following :

- **Chapter 1 - Fundamental concepts** gives a short explanation of aerodynamic forces and boundary layer physics ; special classification scheme for flow control devices is also provided that serves as introduction for the following chapter
- **Chapter 2 - Passive flow control** firstly explores different passive control options, considering devices that are not only present in wind energy sector, but can be mounted on other structures as well (e.g. aircraft) ; secondly, theoretical background behind the concept of vortex generator is provided and comparison analysis of different classes of vortex generators is conducted ; the chapter ends with a summary of most preferred vortex generator configurations and device parameters
- **Chapter 3 - Experimental benchmark** presents the experimental research that serves as validation source for numerical simulation ; specific VG configuration is chosen, which differs from the optimal configuration by the least of parameters
- **Chapter 4 - CFD background** discusses governing equations for viscous flow (i.e. conservation laws) and existing turbulence simulation methods ; special attention is payed to $k - \omega$ SST and Transition SST turbulence models and Shielded Detached Eddy Simulation ; the last section lists modern trends in numerical VG modeling
- **Chapter 5 - Pre – processing stage** elaborates pre – processing stage of CFD simulation process, starting with overview of different grid types and computational domain shapes, before analyzing the actual mesh used for computation ; section on mesh quality compares quality metrics between grids of different aspect ratios and simulation settings are explained in a separate section

- **Chapter 6 - Validation stage** presents a stage in which the results of simulation are compared to experimental values and errors on lift and drag coefficients are determined ; comparison of results obtained with SDES - Transition SST and SDES - $k - \omega$ SST models is available as well as span sensitivity analysis, before composing the resulting graphs of lift and drag coefficients
- **Chapter 7 - Inspection of simulated flow** is the post – processing stage where flows at different angles of attack are compared in terms of velocity and pressure fields, pathlines as well as turbulence structures within Q – criterion ; additionally, comparison between current simulation and a separate study with different VG configuration on the same type of airfoil is carried out.

Chapter 1 - Fundamental concepts

1.1 Components of aerodynamic force

Aerodynamic force exerted on a body immersed in airflow originates from pressure and shear stress distributions acting all over the exposed surface of the body. Pressure acts locally perpendicular and shear stress locally parallel to the surface. The net aerodynamic force R mathematically represents an integral of pressure and shear stress distributions over the total exposed surface area ($\vec{n}$ – normal unit vector, $\vec{t}$ – tangent unit vector) :

$$\vec{R} = -\iint_S p\vec{n}\,dS + \iint_S \tau\vec{t}\,dS$$

Typical body shape for the study of aerodynamics is airfoil. Figure 1.1 displays pressure and shear stress distributions around the contour of an airfoil.

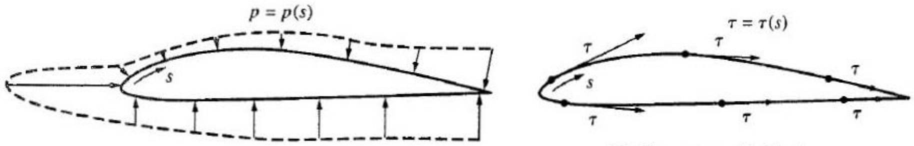

(a) Pressure distribution (schematic only; distorted for clarity)

(b) Shear stress distribution

Figure 1.1 : Pressure and shear stress distributions over an airfoil

By definition, component of aerodynamic force perpendicular to freestream velocity vector v_∞ is lift force L and component parallel to free – stream or relative wind direction is drag force D. Lift and drag act at specific point on a body called center of pressure (i.e. the location of resulting aerodynamic force R), however, lift and drag vectors are commonly shifted to a point 25% c from leading edge, as center of pressure varies with angle of attack. This gives rise to pitching moment $M_{c/4}$ that is always plotted in positive – pitch direction by convention, therefore taking negative values (figure 1.2). Alternatively, lift and drag can be moved to aerodynamic center, which is that point on a body about which aerodynamically generated moment is independent of angle of attack.

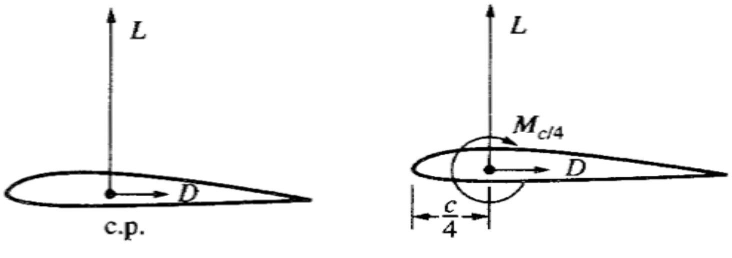

Figure 1.2 : Lift, drag and pitching moment at different positions along the chord

One more way of decomposing aerodynamic force is by introducing normal and axial components. Normal force N is perpendicular to airfoil chord c and axial force A is parallel to airfoil chord. Angle of attack (AoA) α is defined as the angle between the chord and freestream velocity, hence it is also the angle between lift and normal force as well as the angle between drag and axial force (figure 1.3). The relations between different sets of components of aerodynamic force are the following :

$$N = L\cos\alpha + D\sin\alpha$$

$$A = -L\sin\alpha + D\cos\alpha$$

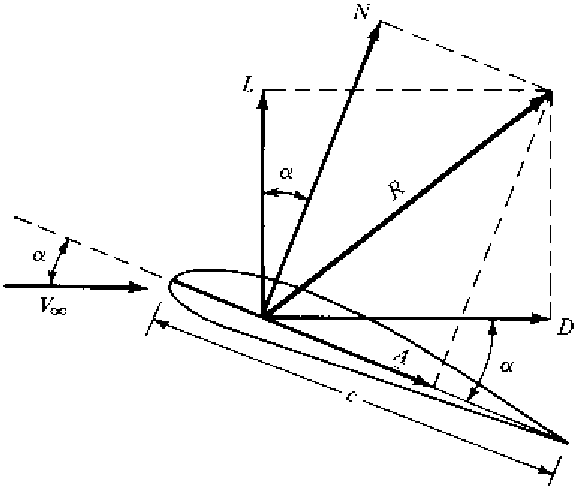

Figure 1.3 : Different components of aerodynamic force acting on an airfoil

Wind turbine is a mean of extracting mechanical energy from the air that is then converted to electricity by generator. Mechanical energy is extracted from airflow that passes through the rotor plane by creation of aerodynamic force, whose conventional components are lift and drag. As seen in the equation above, both forces contribute to a force normal to airfoil chord, giving rise to normal force distribution along the blade. Superposition of normal force distributions from each blade generates torque, which spins the turbine.

1.2 Viscous flow around airfoil

The flow of air around an airfoil can be approximated as :

- inviscid – flow region distant from the airfoil surface where the effects of viscosity are of secondary importance to the flow and are therefore discarded
- viscous – flow region in which effects of viscosity, thermal conduction and mass diffusion are important ; the flow can be distinguished into flow that remains attached to the surface and flow that separates and creates large wake of recirculating flow downstream the airfoil (figure 1.4).

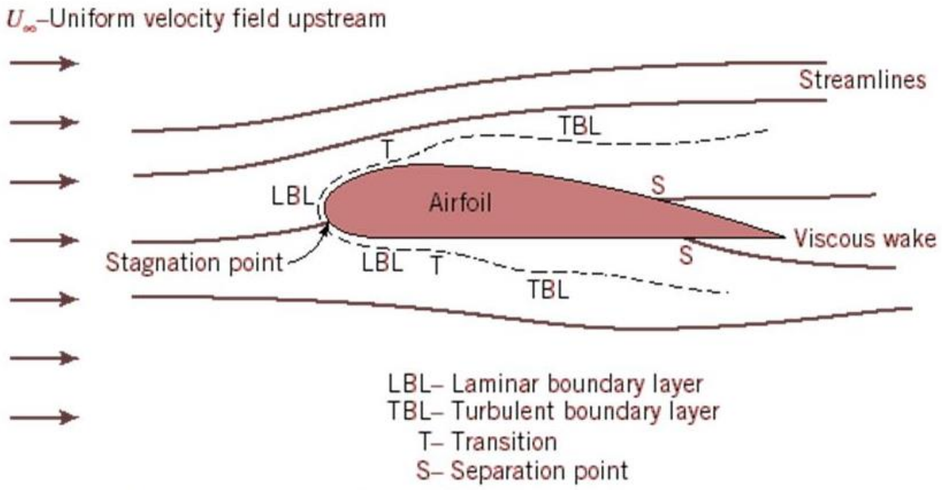

Figure 1.4 : Details of viscous flow around an airfoil

Strictly speaking, viscous flow emerges as either of the following types :

- laminar flow
- transitional flow
- turbulent flow or turbulence.

Laminar flow is a smooth and relatively slow flow, where streamlines have regular shape that is dictated by the flow geometry and where adjacent layers of fluid slide past each other in an orderly fashion. If the applied boundary conditions do not change with time, the flow is steady. It is commonly observed for $Re_x < Re_{crit}$, however it is also possible for low Reynolds and high Mach numbers simultaneously, as is the case with high – altitude hypersonic vehicles where laminar flow can be quite extensive. For local Reynolds numbers around Re_{crit} , laminar flow reaches a transition phase when flow becomes increasingly unstable and eventually transforms into turbulent flow.

There are many factors that encourage transition from laminar to turbulent flow. However, the most notable causes of flow transition can be listed :

- **increased surface roughness** – a technique often used during wind tunnel testing to ‘trip’ laminar flow to fully turbulent regime – forced transitions
- **increased freestream turbulence** – when two wind tunnels have different levels of freestream turbulence, generated data from one tunnel cannot be repeated in the other
- **adverse pressure gradient (APG)** – strongly favors flow transition, contrary to favorable pressure gradient (FPG) which tends to preserve initially laminar flow
- **flow heating** – if surface temperature is higher than temperature of adjacent fluid, heat is transferred to the flow and instabilities in laminar flow are amplified, hence favoring early transition ; in contrast, a cold wall tends to maintain laminar flow.

Unfortunately, there is no standard, general definition of turbulence that can satisfy all properties of turbulent flow. There are only attempts to give explanation that could approximately describe such physical phenomenon :

- turbulent flow is flow motion with infinite number of degrees of freedom
- turbulent flow (turbulence) is :
  - chaotic
  - unpredictable
  - random → due to random fluctuations
  - unsteady → even with imposed steady boundary conditions
  - three – dimensional → even in flows where mean velocities and pressures vary in only one or two space dimensions, since turbulent fluctuations always have spatial character
  - rotational → visualizations of turbulent flow reveal rotational flow structures, the so – called turbulent eddies, within a wide range of length scales

  flow where in each point of the flowfield each flow quantity is random in character and mean statistical values of flow quantities can be defined.

In aerodynamics, the most important form of viscous flow is boundary layer (BL) of which two kinds can be distinguished :

- velocity boundary layer (VBL)
- thermal boundary layer (TBL).

Velocity boundary layer (or just boundary layer) is a thin layer of moving fluid over a convex surface, where the effects of viscosity are of paramount importance and changes in direction perpendicular to the surface are far greater than changes in flow direction $\left(\frac{\partial}{\partial y} \gg \frac{\partial}{\partial x}\right)$. Velocity profile starts from the zero value at the wall (no – slip condition) and reaches 99% of free stream value v_∞ at a height that represents boundary layer thickness δ (figure 1.5). Boundary layer starts as laminar flow at the leading edge of the airfoil before transforming into turbulent flow by free (natural) or forced transition.

Turbulent boundary layer features higher – energy fluid elements from the outer regions of the flow positioned close to the surface. As a result, average flow velocity near solid surface is higher for turbulent flow compared to laminar boundary layer.

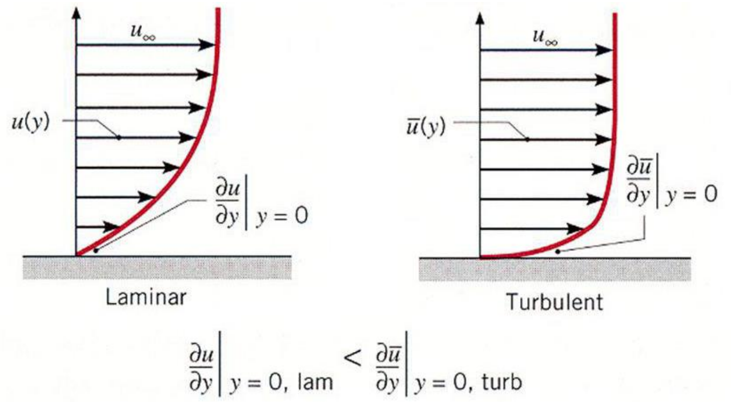

Figure 1.5 : Comparison of laminar and turbulent velocity profiles in boundary layer

Figure 1.5 shows that wall velocity gradient $(n = 0)$ is greater for turbulent BL, which is an important observation. Higher wall velocity gradient means frictional effects are more severe for turbulent flow, i.e. shear stress and aerodynamic heating are larger in turbulent boundary layer. Still, turbulent flow tends to separate at a later stage, separated region becomes smaller and overall, pressure drag is lower. It follows that laminar BL is more favorable for slender bodies (e.g. airfoil) as drag then mostly consists of skin friction, while for blunt bodies it is desirable to have turbulent BL for minimal separation and minimal pressure drag. For this reason the surface of golf ball is covered with dimples.

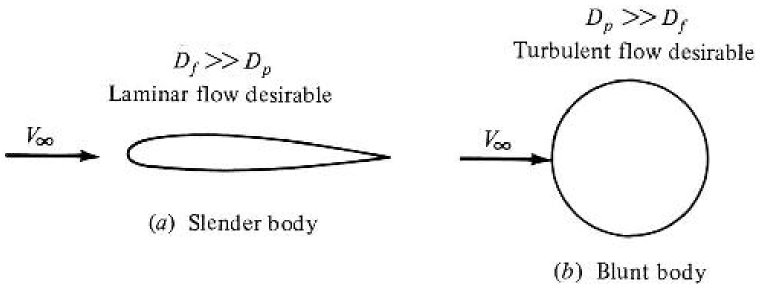

(*a*) Slender body

(*b*) Blunt body

Figure 1.6 : Skin friction and pressure drag on slender and blunt bodies

Attached flow over a convex surface, such as BL flow over suction side of airfoil, is explained by Coanda effect. Due to convex geometry of suction side, positive pressure gradient exists perpendicular to the surface, therefore, fluid element inside BL experiences a centripetal force. As centripetal force is indicative of curvilinear motion, the observed fluid element follows the curvature of airfoil, otherwise it would move tangentially along a straight line due to its inertia.

The problem represents positive pressure gradient downstream the surface, caused by geometry and angle of attack at which airfoil is positioned. Adverse pressure gradient together with shear stress distribution forces fluid inside boundary layer to decelerate and eventually run out of kinetic energy. The result becomes a chaotic motion downstream the airfoil. If velocity profile is observed, it is seen that velocities reduce and BL thickness increases, while separation happens at point where velocity gradient reaches zero – separation point. Finally, inside separated flow velocity profile is reversed (hence the name – region of reversed flow, figure 1.7) and large downstream wake of recirculating fluid is generated.

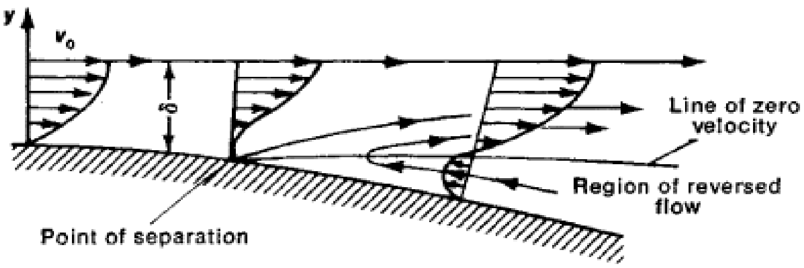

Figure 1.7 : Boundary layer velocity profile during flow separation

Separation may be also provoked by flow convergence and cross flow, as found, for example, on afterbodies and swept wings. Interference effects stand as another possible mechanism where boundary layers coincide with each other at junctions of different aircraft components (e.g. wing – fuselage). Flow separation due to shock wave is another possible cause that develops once critical Mach number M_{crit} is reached by aerodynamic surface. Since transonic speeds are not likely to occur at the root section of wind turbine blade, shock waves are not of primary concern.

Flow separation is manifested by rise in skin friction (higher mixing rates) and appearance of pressure or form drag due to new pressure distribution around airfoil. The onset of stall represents massive flow separation (i.e. almost complete BL separation, figure 1.8) that takes place at angles of attack above critical angle α_{crit}. Stall phenomenon explains further increase in drag and drastic drop of lift force (figure 1.9). Decrease in lift means a decrease in torque and less power output by wind turbine. On one hand, greater drag force mitigates the decrease in normal force magnitude caused by lift drop. On the other, structural load grows. Secondly, fatigue loads are experienced by the blade as lift and drag forces drop and recover in a cyclic manner as turbulence gusts periodically occur. Major part of the induced noise is attributed to stall as well.

The onset of stall causes similar problems with airplane wings. In addition to previously described complications, the controllability of an airplane can be jeopardized as the stall region spreads along the wing, eventually reaching control surfaces, e.g. ailerons. Nevertheless, critical angle of attack presents an important flow condition where maximum lift coefficient C_{Lmax} is achieved (figure 1.9), whether just airfoil itself or the whole aircraft is designed. Maximum lift coefficient often presents a necessary variable in estimating airplane perfomance parameters, such as minimum take – off and landing velocity, important for the choice of control surfaces :

$$v_{min} = \sqrt{\frac{2mg}{\rho C_{Zmax} S}}$$

Figure 1.8 : Flow structure of airfoil stall

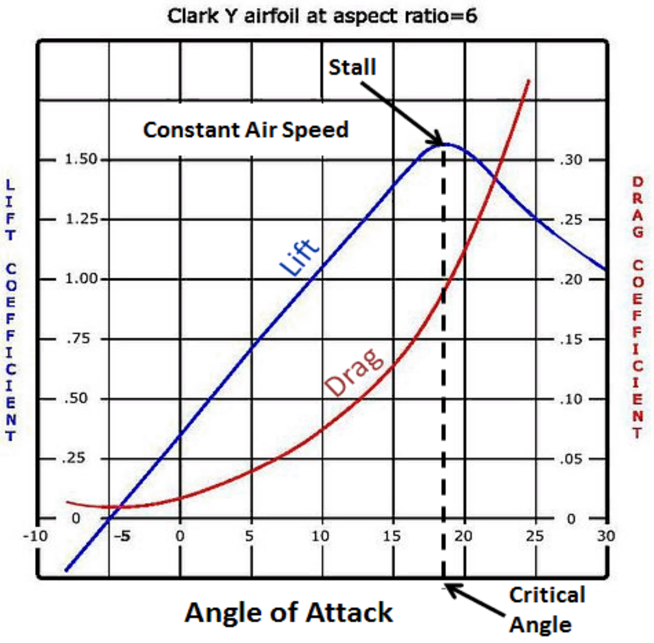

Figure 1.9 : Lift and drag coefficient curves with indicated stall condition for Clark Y airfoil

1.3 Flow control devices for wind turbines

Flow in boundary layer can be controlled through a passive method – does not require a controller or an active method – does require a controller and controlling sensors. Active flow control methodology branches into predetermined and interactive (figure 1.10). Predetermined control introduces steady or unsteady energy inputs without concern for the state of flow. There are no sensors required for this method and the control loop is open. In contrast, an interactive flow control system contains an actuator, controller and sensor and is able to operate in open – and closed – loop form. Open – loop form does not observe the output process that is being controlled and cannot determine if its input has achieved the desired goal. On the other hand, closed – loop control makes use of feedback to compare the actual with desired output, allowing minimization of error between the reference value and feedback signal.

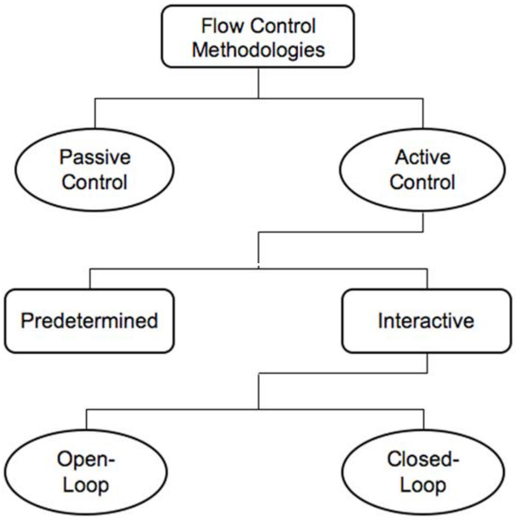

Figure 1.10 : Classification of flow control methodologies

In terms of lift enhancement, active control devices present better results than passive devices, enabling higher energy efficiency of wind turbines. However, an important fact remains that active devices require an energy source and controlling mechanism which requires to be integrated within the blades and regular maintenance is necessary. All in all, the use and further development of passive devices is more preferable. Research studies on passive flow control configurations are constantly undertaken, in order to reach performance improvements similar to active devices at distinctly lower cost. Upgrades of control devices may increase life – cycle and power production at reduced capital and maintenance costs, allowing greater competitiveness in price against conventional energy sources or renewable alternatives.

Wast number of flow control devices exists. Many of these have different mechanical and aerodynamic operating principles or are at different levels of maturity, since some devices are not yet tested on full – scale model or tests are performed for different structures apart from wind turbine. Therefore, it is difficult to carry out direct comparison. Instead, a five – layer classification scheme designed by Wood [5] and modified by Johnson et al. [6] is employed :

- 1st layer – according to necessity of energy source and controlling mechanism :
  - passive device (P) – improvement in aerodynamic effiency and loads reduction without external energy consumption :
    - fixed slat
    - fixed Gurney flap
    - flow vane
    - leading edge protuberances
    - fence
    - spoiler
    - serrated trailing edge
    - vortilon
    - vortex generators
    - etc.
  - active device (A) – improvement in aerodynamic effiency and loads reduction with external energy consumption or secondary power source :
    - slat
    - traditional trailing edge flap
    - non – traditional trailing edge flap
    - microtabs
    - active stall strips
    - stall ribs
    - devices based on BL blowing and suction
    - plasma actuators
    - synthetic jets
    - shape changing airfoil
    - etc.
- 2nd layer – according to technique :
  - geometric device (G) : moves a portion of airfoil external surface changing the section shape and attaching the airflow to the surface (e.g. vortex generators)
  - fluidic device (F) : changes the flow about the blade section by either adding air into or subtracting air from external flow (e.g. devices based on BL blowing and suction)
  - geometric and fluidic device (G / F) : combination of the mentioned types (e.g. synthetic jets)
  - plasma actuators (P)

- 3rd layer – according to location of device :
    - near leading edge (LE) (e.g. vortex generators)
    - near trailing edge (TE) (e.g. trailing edge flap)
    - near both leading and trailing edges (LE/TE) (e.g. devices based on BL blowing and suction)
    - in the mid – chord (MC) (e.g. shape changing airfoil)

- 4th layer – according to lift curve modifications :
    - concept of shifting the entire lift curve up or down by effectively changing airfoil camber (figure 1.11b) :
        - device for lift increase (I) (e.g. shape changing airfoil)
        - device for lift decrease (D) (e.g. active stall strips)
        - device for both lift increase and decrease (I/D) (e.g. trailing edge flap)
    - delaying stall (DS) concept where devices extend the lift curve to higher C_{Lmax} at higher critical angle of attack α_{crit} (figure 1.11a, e.g. vortex generators) ; this can be very useful as airfoil chord is then reduced for the same maximum lift (Corten's idea [7]) and is one of the reasons for sliced trailing edge on many wind turbine airfoils

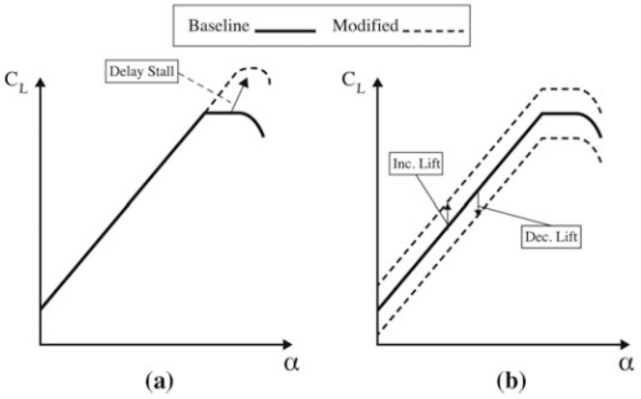

Figure 1.11 : Possible effects of flow control device on the lift curve

- 5th layer – according to time variation of device position :
    - steady device (S) – device position is at constant setting (e.g. vortex generators)
    - unsteady device (U) – device position varies about a nominal setting with time (e.g. synthetic jets)
    - device capable of steady and unsteady operations (S/U) (e.g. trailing edge flap).

Chapter 2 - Passive flow control

2.1 Overview of passive flow control devices

The last section of previous chapter provided an outstanding classification layout for flow control devices of various purpose, those used by aircraft and rotorcraft as well as wind turbines. Lists of active and passive control devices are non – exhaustive and can be regularly modified, since new ideas are constantly developed. Focus of the chapter is on passive control, so brief descriptions of several important concepts is given as a start.

Fixed slat – aerodynamic effect of the leading edge slot or fixed slat is often misinterpreted as being similar to a flow duct configuration. In reality, the operational principle behind it is a multifaceted flow interaction problem. It involves the reduction of pressure gradient on the main airfoil in combination with the modification of Kutta condition for the fore part of slotted airfoil (or the slat element). This leads to higher lift values at high AoA compared to clean airfoil as well as stall delay. Certain drag penalty does exist in case of fixed slotted airfoils, but maintaining a relatively high C_L/C_D ratio is still possible.

Figure 2.1 : Example of movable slat on a wing of an aircraft

Fixed Gurney flap – simple flat plate of the order of 1% c, positioned perpendicularly to the pressure or suction side at trailing edge. When properly sized, Gurney flap increases total lift of the airfoil, while reducing drag.

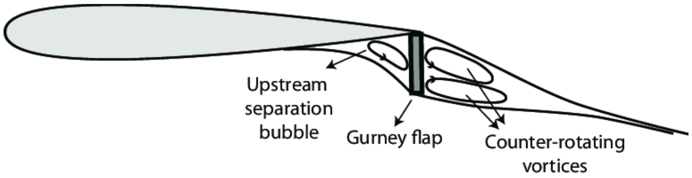

Figure 2.2 : Fixed Gurney flap and its effect on the surrounding airflow

Flow vane – a new passive flow control concept, developed by G. Pechlivanoglou [8]. General configuration includes a conventional wind turbine blade equipped with additional airfoil of smaller chord over the main profile. The gap between the profiles is approximately equal to chord length of upper profile. The function of upper profile is to induce a downwash at the trailing edge region of the main airfoil in order to suppress stall. This would increase the effective AoA range of the main airfoil and increase efficiency of the inner part of conventional blades that often operate in near stall conditions.

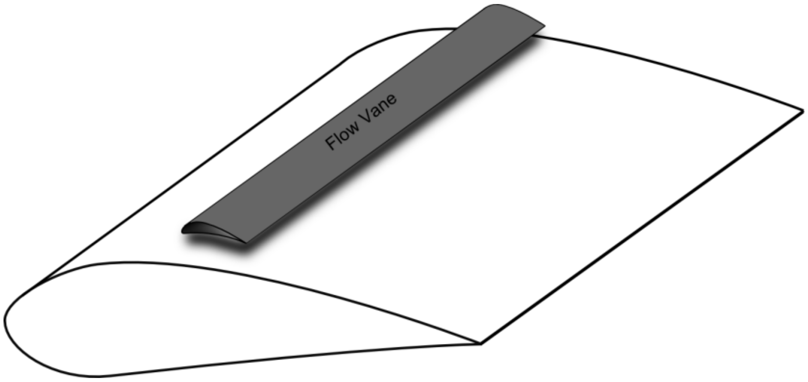

Figure 2.3 : Schematic representation of flow vane design

Fence – a fin – like vertical surface extruding from the suction side of a wing/blade. Its function is to control the airflow propagation in spanwise direction by disrupting it, in order to protect the outboard region from an inboard stall (figure 2.4). This way, aileron effectiveness is maintained during stall, enabling the pilot to keep a leveled flight and exit the stall safely. In case of wind turbines, disruptions in lift distribution can occur as a consequence of adverse Coriolis' effects. The extent to which the fence is able to mitigate undesirable BL flow directly relates to fence height. However, greater height implies greater parasitic drag as well as its negative effect on spanwise lift distribution.

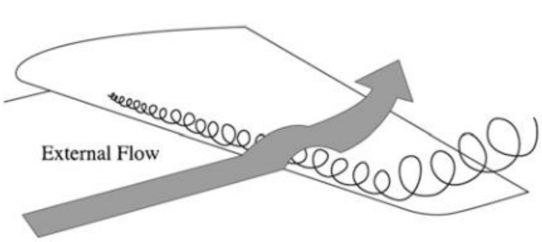

Figure 2.4 : Example of spanwise airflow along the wing

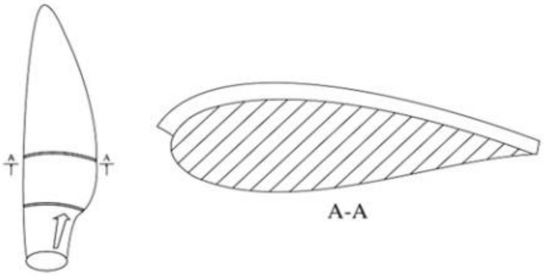

Figure 2.5 : Fence on a wind turbine blade

Spoiler – the root and transition blade segments, due to their particular cross section shape, do not contribute to the overall energy production of a wind turbine, moreover, energy output is decreased because of their contribution to structure’s drag. These sections often work in stall conditions, especially at high wind speeds. Therefore, it is desirable to think of a mechanism, such as spoiler, to increase the lift in these conditions and that way increase the power output. Spoiler is assembled in the inboard portion of a blade, that is, the region nearest to the hub and the transition region of the blade (figure 2.6). A realistic estimate of the potential performance improvement is about 1 – 1,5% of annual energy output compared to conventional wind turbine blades without spoilers.

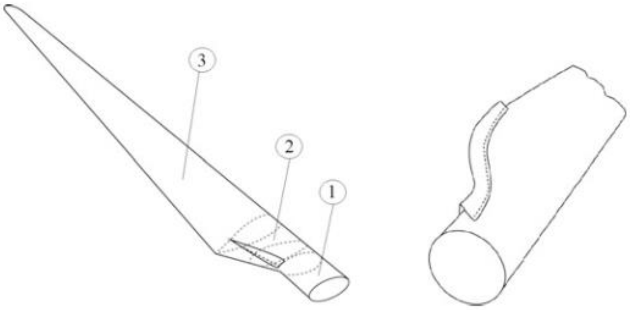

Figure 2.6 : Regions of wind turbine blade with spoiler device

Serrated trailing edge – originally, aerodynamic surfaces of wind turbine blades have sharp or moderately blunt trailing edges from which the wake is shed. The shedding of the wake and the confluence of flows from both pressure and suction sides are sources of aerodynamic noise, increased drag and reduced lift. It has long been recognized that noise may be reduced by modifying the trailing edge geometry, so the amount of vorticity that is scattered into sound is reduced. One alternative solution for this kind of problem is a patent called flexible serrated trailing edge, also known as Dino Tail (figure 2.7). However, such idea seems meaningful only for the outboard region, close to blade tip.

Figure 2.7 : Serrated trailing edge of wind turbine blade

Vortilon – creates of strong vortices that are able to stabilize the flow over the suction side of an airfoil, thus delaying stall (figure 2.8, left). Main benefit is the combination of strong flow stabilizing effects with small parasitic drag penalty. To achieve the creation of vortices at high AoA, vortilon has to be positioned at the pressure side, extending in front of the leading edge of the airfoil in order to intersect with the stagnation streamline at high AoA. The outward flow component, found on swept wings and rotor blades, in combination with the vortilon's location, initiates the formation of a strong vortex at the inboard side of the vortilon that re – energizes BL of the airfoil by free stream – – boundary layer mixing. Vortilons were invented by R.Shevell during the development of commercial twin – jet aircraft DC – 9 at Douglas Aircraft Corp. and since then vortilons have been frequently used on commercial and military aircraft.

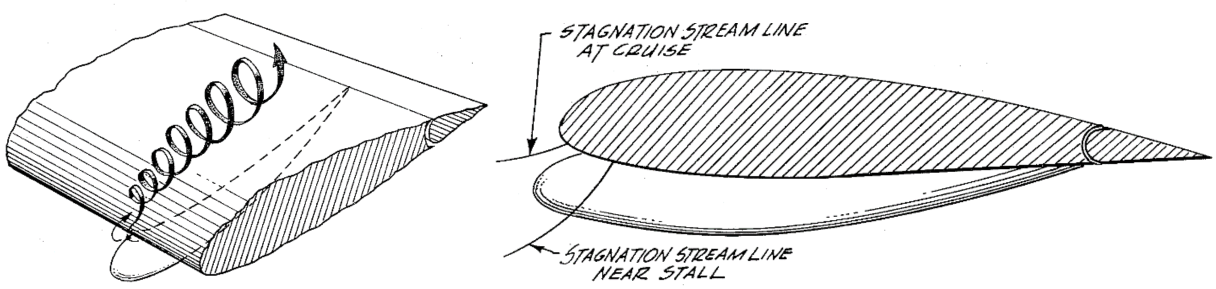

Figure 2.8 : Vortilon shape and location on a wing / blade airfoil

Vortex generator – the entire next section is devoted to the concept of vortex generator.

2.2 Definition of vortex generator (VG)

Passive flow control through generation of vortices in streamwise, longitudinal direction is common on many lifting surfaces, such as aircraft wing or wind turbine blade. Several devices which exploit this physical mechanism are shown below :

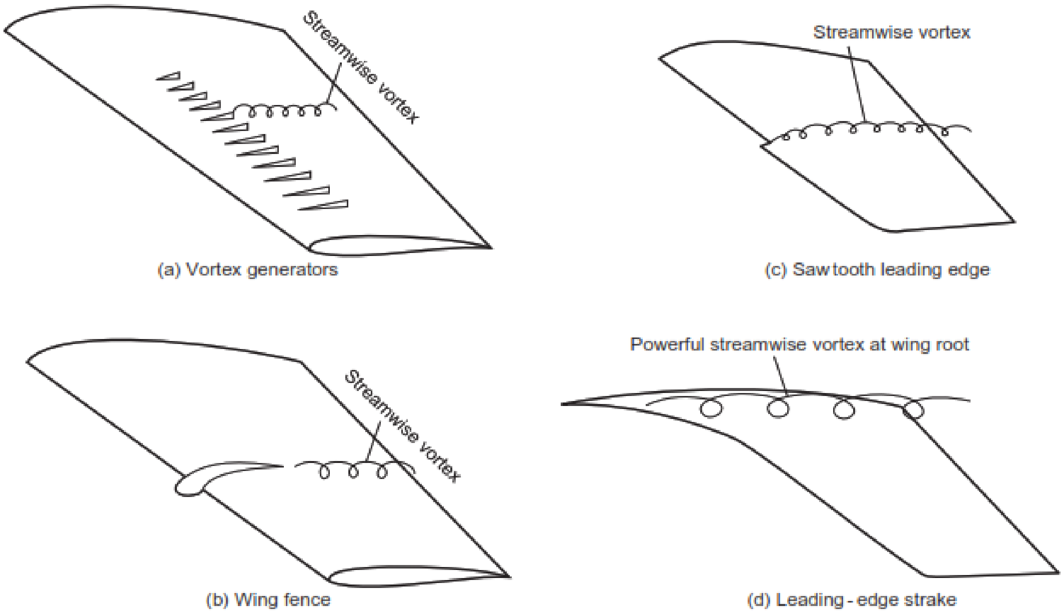

Figure 2.9 : Four common vortex – generating devices for controlling flow over swept wings []

Vortex generator (VG) is a passive flow control device which generates longitudinal vortices that increase the mixing between lower layers of external flow and boundary layer. Fluid particles with high momentum in external flow mix with the low – momentum viscous flow inside BL, hence, mean streamwise momentum of fluid particles in BL increases. In other words, momentum from external region is introduced into inner region of wall bounded flow. The process provides a continuous source of momentum to counter the natural momentum decrease inside boundary layer and the growth of thickness caused by skin friction and adverse pressure gradient.

Ultimate goal of vortex generators is delay or prevention of flow separation and eventual stall. Delay and prevention of stall rule out any abrupt change in performance and increase of structural and fatigue loads that lessen the strucutre lifespan. The fact airfoils are able to operate at higher C_L makes possible to have slender wings / blades (chord is shortened, explained in section 1.3), reducing the amount of material and structural weight. Sensitivity to roughness and noise are also mitigated by employing vortex generators.

First application of vortex generators came in 1947 by Harlan D. Taylor for elimination of diffuser separation [10]. The first time VGs were attached to a wind turbine blade was in 1982 by Boeing on Mod – 2 wind turbine of 2.5 MW [9].

Vortex generators come in different shapes and configurations, however, certain advantages and disadvantages are common :

- advantages:
  - passive control device ⇒ no energy source required
  - increase in lift ⇒ increase in torque and power that may be comparable to results obtained with active control devices
  - small size ⇒ large number of VGs along the wing / blade is possible
  - simple design ⇒ low production cost
  - attachment to the surface can be a post – production fix to blades that do not perform as expected, without any alterations to surface material
  - very simply replaceable at any time
- disadvantages:
  - additional parasitic drag to the blade due to presence of the control device
  - additional parasitic drag at cruise condition when stall suppression is not of primary concern, since no possibility of retracting VGs inside the wing
  - although lift is increased for higher of angles of attack, more abrupt stall than without vortex generators is possible
  - cannot be used for active stall control, a technology now being used for highly maneuverable fighter aircraft.

There are two main categories of VG application. First, VGs are used for flow separation control on various airfoils and wings. More precisely, this includes low – Reynolds number airfoil, high – lift airfoil, highly swept wings and transonic airfoil. Secondly, they are used for flow control in non – airfoil applications, such as aircraft interior noise reduction at transonic cruise, reduction of engine face – flow distortion in compact inlet as well as for more efficient overwing fairing. Numerous applications in turbomachinery and heat transfer devices are also worth mentioning.

Drawbacks of vortex generator concept have led to the development of air jet vortex generators (AJVGs) or vortex generator jets (VGJs). As much as interesting they might seem, AJVGs and VGJs are left for some other thesis discussion.

2.3 Classification of vortex generators

Vortex generators have been explored for more than fifty years for a broad range of applications. There are numerous studies on different vortex generator configurations and it is impossible to present all the types in a systematic manner. Hence, the following list of professor John C. Lin [11] is non – exhaustive, but contains the most relevant designs for industrial application nowadays.

Classification of vortex generators :

1) based on vortex direction :
   - **devices producing streamwise or longitudinal vortices** – all types under 2) and 3)
   - **devices producing spanwise or transversal, lateral vortices** :
     - spanwise cylinders
     - large – eddy break – up (LEBU) devices
     - elongated arches
     - Viet’s flappers
     - transverse grooves
     - etc
2) based on size :
   - **conventional size** – height of the order of boundary layer thickness
   - **low – profile, micro or sub – boundary layer size** – fraction of boundary layer thickness (usually 20 – 50%)
3) based on shape :
   - **vane type –** vertical planar objects attached to airfoil surface, have the most sub – divisions and are most prone to modifications ; their rather regular shape allows various mathematical modeling (e.g. lift and drag prediction for delta vane) and makes possible to analytically design new geometries ; sensitive to yaw of the local flow direction :

- based on cross section :
  - classically shaped
  - aerodynamically shaped :
    - symmetrical airfoil
    - asymmetrical or cambered airfoil

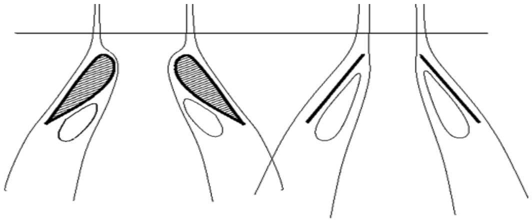

Figure 2.10 : Cambered vs flat plate cross section

- based on planform geometry – shape :
  - basic :
    - rectangular
    - trapezoidal or cropped – delta
    - triangular or delta
  - alternative :
    - gothic
    - parabolic
    - ogive

- based on array arrangement :
  - based on number of rows :
    - single row
    - multiple or tandem rows :
      - aligned
      - staggered
  - based on relative orientation :
    - counter – rotating (CtR) :
      - common upwash (CU)
      - common downwash (CD)
    - co – rotating (CoR)
    - biplane or alternate pairs

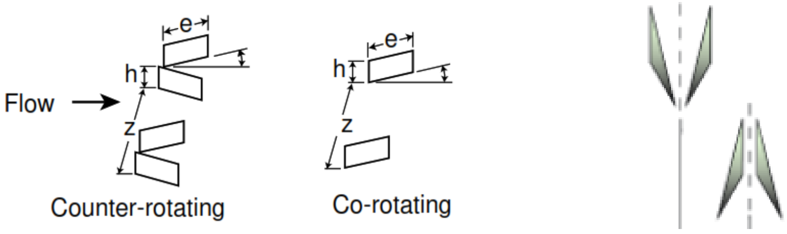

Figure 2.11 : Counter – / co – rotating (left) and common downwash / upwash arrays (right)

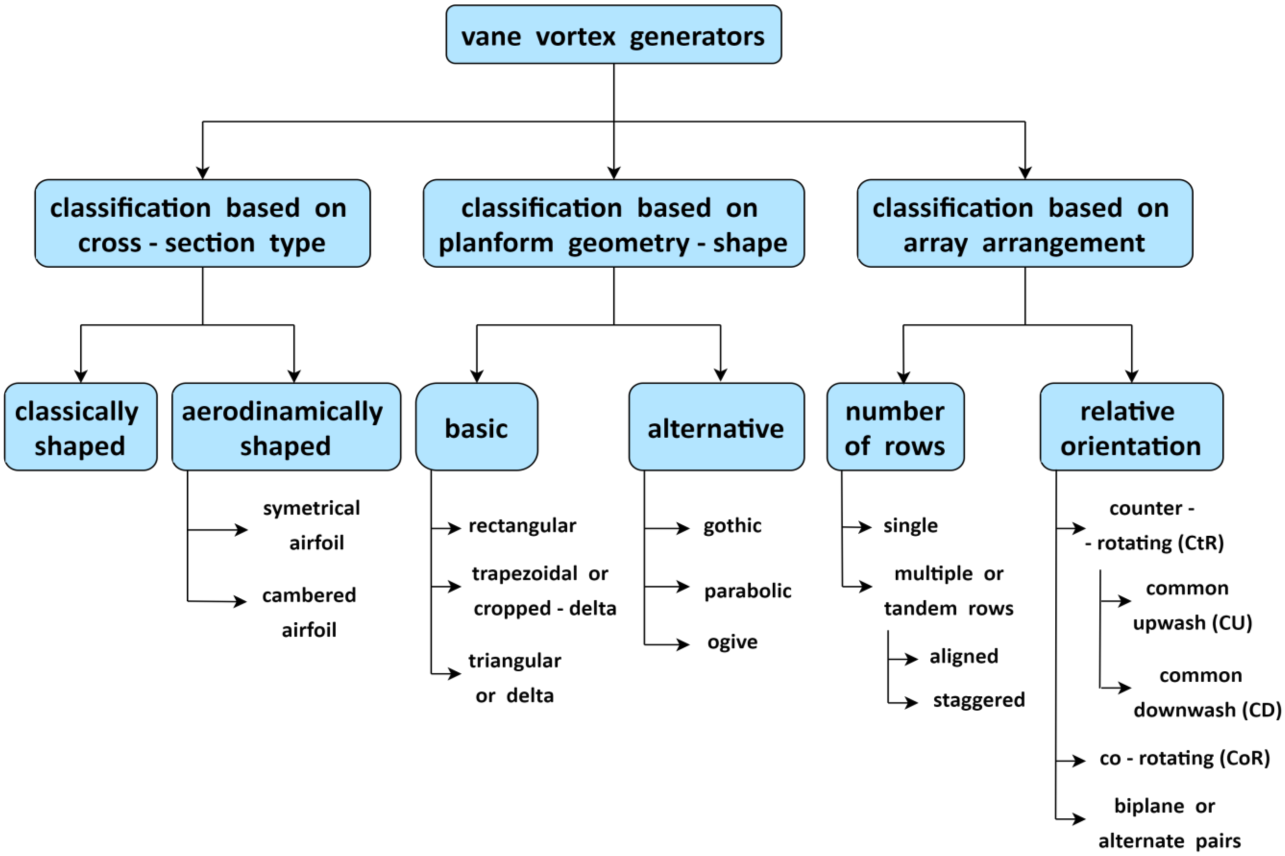

Figure 2.12 : Classification of vane vortex generators

- **wedge type** – basically, two joined delta vanes with material filling the space between them ; the only difference between two kinds of these VGs is direction of orientation:
  - forward wedge – ramp
  - backward wedge – triangular plow

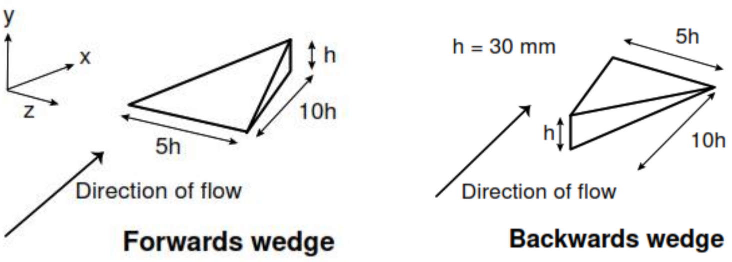

Figure 2.13 : Wedge type vortex generators

- **Wheeler type** – the basic shape is a modified V sign, with no material between branches in case of Wishbone type and with material in the space between branches in doublet type (needless to say, the shape is doubled, with rear VG starting in the aft part of frontal VG) :
    - Wishbone type
    - doublet type

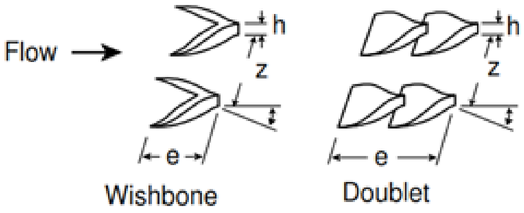

Figure 2.14 : Wheeler type vortex generators

- **hemispherical or obstacle type** – this kind of VG converts boundary layer vorticity, normal to the axis of the main flow, into streamwise vorticity ; the flow associated with the streamwise vorticity has been referred to as a 'secondary' flow ; in case of a bump obstacle VG, low – profile version is more appreciated (all VGs, especially low – profile, generate secondary flows near the wall, however, at least for the vane type, these flows are of secondary importance to the main vortex flow) :
    - cylindrical or Dowel type
    - 'bump' type

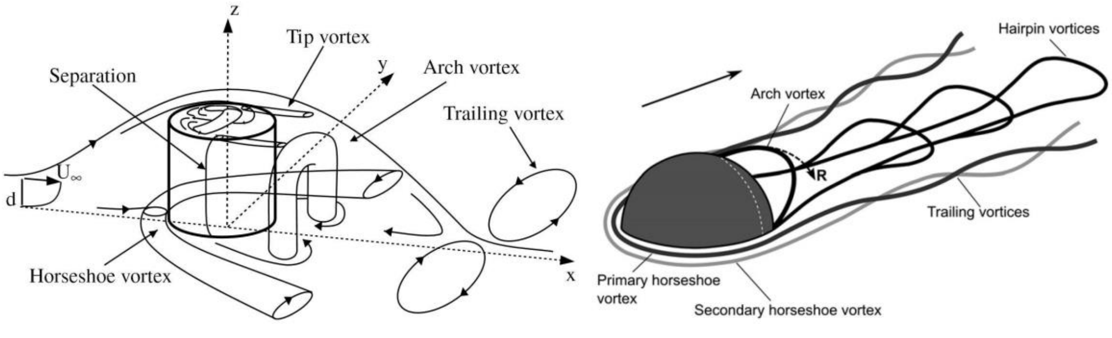

Figure 2.15 : Cylindrical or Dowel type (left) and 'bump' type (right) VGs

- **rod type** – compared to classical vanes, parasitic drag is much smaller ; simple geometry of rod vortex generator (RVG) allows combination with MEMS (Micro – electromechanical systems) technology that deploys the rod when needed, although this requires a controlling mechanism :

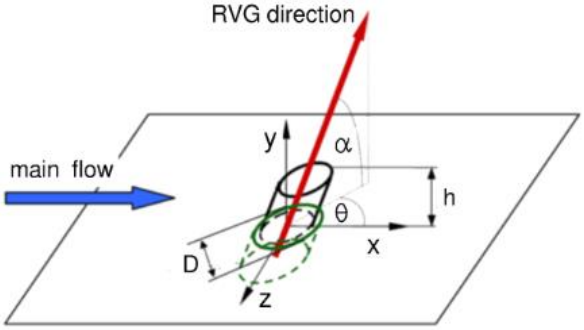

Figure 2.16 : Rod vortex generator with possibility of retraction

- **wing type** – small plate or wing held in the stream with each one set at an angle of incidence to it in order to produce a pair of opposite trailing vortices; the plane of the wing is usually placed parallel to the main surface, either just above it or just ahead of it, so that vortices trail over the surface from its leading edge ; insensitive to yaw of the local flow direction, differently from vanes, very useful where the local flow direction is not known or a subject to change :
    - according to location :
        - at leading edge
        - on suction side
    - according to relative positioning :
        - counter – rotating
        - biplane
        - twisted strip

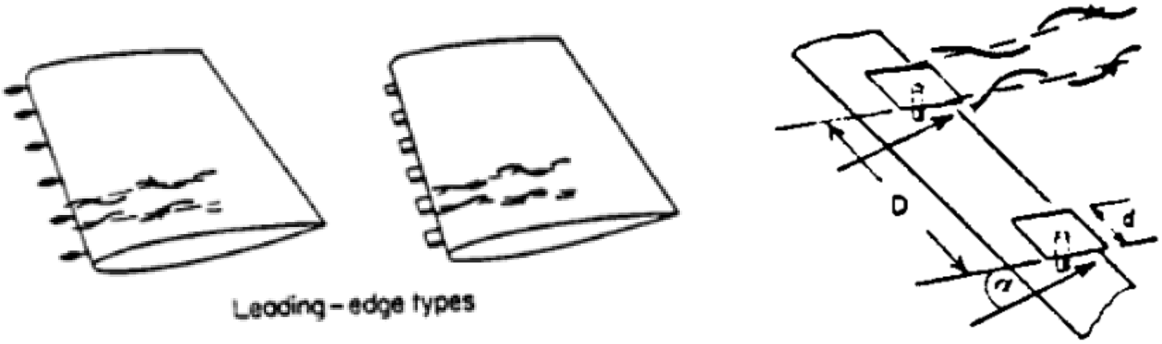

Leading – edge types

Figure 2.17 : Wing type VGs on leading edge and airfoil surface

2.4 Comparison between classes of vortex generators

Streamwise vortices vs. spanwise vortices

Professor Lin in his report [11] elaborated that devices generating vortices in spanwise direction generate vortices of less strength, thus, less effective than in case where streamwise direction is followed. Moreover, since these devices require more complete spanwise coverage, higher pressure drag is obtained. Thus, more preferred choice in aeronautical and wind engineering are devices producing streamwise or longitudinal vortices.

Conventional size vs. low – profile VGs

Although larger dimensions mean increase in circulation, to which vortex strength is directly proportional, one must also pay attention to adverse effects caused by such dimensions. Drag increase is one example, which rises with VG height and length. Therefore, not only the increase in critical angle and maximum lift coefficient is what matters, but also the new aerodynamic efficiency $\frac{C_L}{C_D}$ of the airfoil has to be considered.

Obviously, low – profile VGs give less parasitic drag (smaller dimensions), but smaller decrease in pressure drag (sooner flow separation, less separated flow recovered) than conventional VGs. Also less increment in lift force of airfoil equipped with flow devices is evident. Nevertheless, Lin found that low – profile vane type VGs are still able to recover as much as 90% of the separated region. Effectiveness of low – profile VGs is at least partially attributed to the full velocity profile of a turbulent boundary layer (figure 2.18). Even for relative height of only 20%, local velocity is over 75% of the free stream velocity value. Any further increase in height provides only a moderate increase in local velocity, but notably increases the device drag.

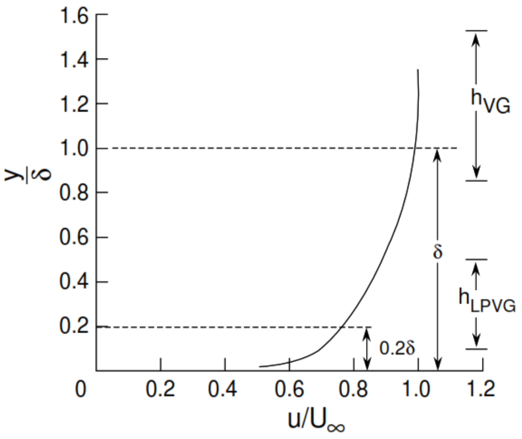

Figure 2.18 : VG height relative to turbulent boundary layer velocity profile

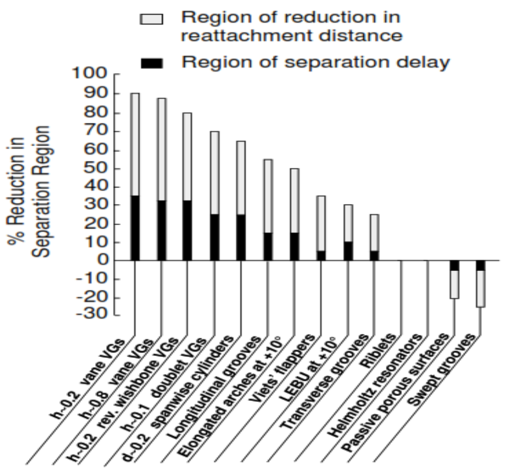

Figure 2.19 : Relative effectiveness in flow separation control vs device category

Despite very promising vorticity characteristics, the generated vortices have reduced downstream coverage due to smaller dimensions of VGs. In order to exploit their strength as much as possible, the distance that vortices cover from VG trailing edges to separation baseline needs to be reasonably short and approximately constant over time. This is not necessary for conventional VGs. Hence, if low – profile VGs are mounted, the separation line must be relatively fixed.

Conventional size VGs also have the tendency (at least the vane type) to generate highly three – dimensional attached flow and pockets of recirculating fluid. Although the flow seems attached, stability of the flow is compromised. This also gives rise to severe skin friction due to high degree of mixing. Therefore, although flow separation delay and lift performance increment are highly desirable features of conventional VGs, significant contribution to parasitic drag, high friction as well as flow instability cannot be ignored. On the other hand, vortices coming from low – profile generators exert their influence on the flow where matters – within BL and are strong just enough to push back flow separation, without unnecessarily persisting inside boundary layer.

Comparison on the basis of VG shape

Concept of wing – type VGs can hardly be imagined in low – profile version due to relatively complex design, while production / installation expenses are high and the device drag is not helping at all. Obstacle type VGs feature the already mentioned problem of secondary flows that cannot be discarded as in case of other VG types. As far as rod VGs are considered, their simple design, combined with notably low device drag, seem promising at first, however, their optimal use eventually involves some implementation of active control mechanisms.

Lin has systematized different VG types as well. Wheeler Wishbone VGs perform the best in terms of separation delay and reduction in reattachment distance when $h/\delta \sim 0.2$ and are comparable to vane VGs of $h/\delta \sim 0.8$ (figure 2.19). In fact, in the range 0.2 – 0.8 vanes are always a more viable option. When the relative height falls to 10% of boundary layer thickness, Wheeler doublet VGs are more effective than vanes due to their extended device chord length (double rows).

Wedge and vane VGs (figure 2.20) are further compared by analyzing vortex strength and vortex decay rate as first criteria. Backwards wedge or triangular plow exhibits the highest decay rate due to high proximity of generated vortices to the surface (wall shear is drastically increased). Decay rate of joined vanes is explained by interference effects between adjacent vortices (vanes are connected), whereas interference is less damaging for spaced delta vanes that have the lowest decay rate. Vortices of joined vanes are the strongest in immediate vane vicinity, further downstream the strongest vortices are generated by spaced vanes, followed by joined vanes and ramp.

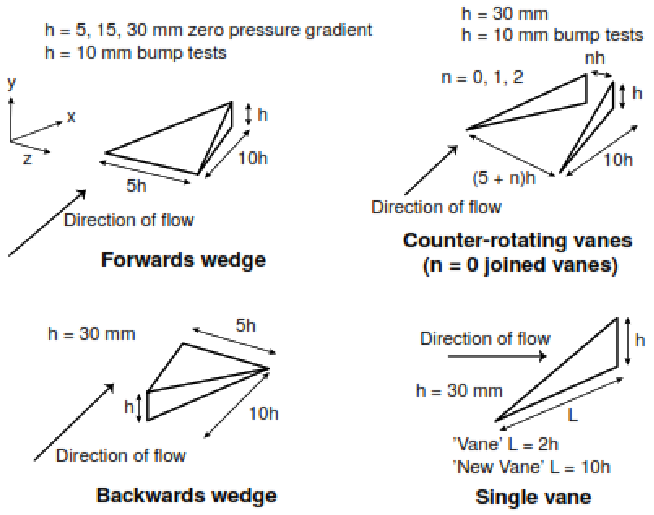

Figure 2.20 : Different low – profile, micro – or SBVGs

The order in terms of parasitic or device drag is different for zero and adverse pressure gradients. Drag measurements in ZPG indicate that ramp generates about 40% of drag generated by spaced vanes. Measurements in APG found that by increasing the gap ratio *n*, device drag of spaced vanes reduces accordingly.

The comparisons are clearly in favor of spaced counter – rotating (CtR) vane VGs. Although delta vanes are considered, it will be shown that similar conclusions hold also for some other vane types.

Performance parameters for different low - profile VG types	Vortex strength	Vortex decay rate	Device drag	
			ZPG	APG
Spaced vanes	highest	lowest	higher	lowest
Joined vanes	higher	lower	lower	lower
Forwards wedge (ramp)	lower	higher	lowest	higher
Backwards wedge (wedge)	lowest	highest	highest	highest

Table 2.1 : Performance comparison of most common low – profile VGs

2.5 Comparison between classes of vane vortex generators

Counter – rotating (CtR) vs. co – rotating (CoR) array of vane VGs

Counter – rotating array dissociates upward and downward momentum transport (figure 2.21). High momentum flow is transported downwards to the wall around the line of symmetry of each VG pair. Low momentum flow is transported upwards to the free stream between two different VGs. Drawback of this mechanism is high damping between vortices. In spite of higher efficiency in momentum transfer than co – rotating system, it has been observed that vortices move away from the wall region. This appeared for vortices embedded in a ZPG boundary layer and for an equidistant spanwise spacing between the vortices. Results of studies reviewed in [11], show that in APG condition, counter – rotating array of vortices stays near the wall, even far downstream. It was estimated that vortex life distance is around 100h, while the effectiveness of vortices of SBVGs to be in range $17 < \Delta X_{VG}/h < 52$. CtR array with common upwash (CtR – CU) proves ineffective compared to common downwash (CtR – CD) array due to premature vortex ejection.

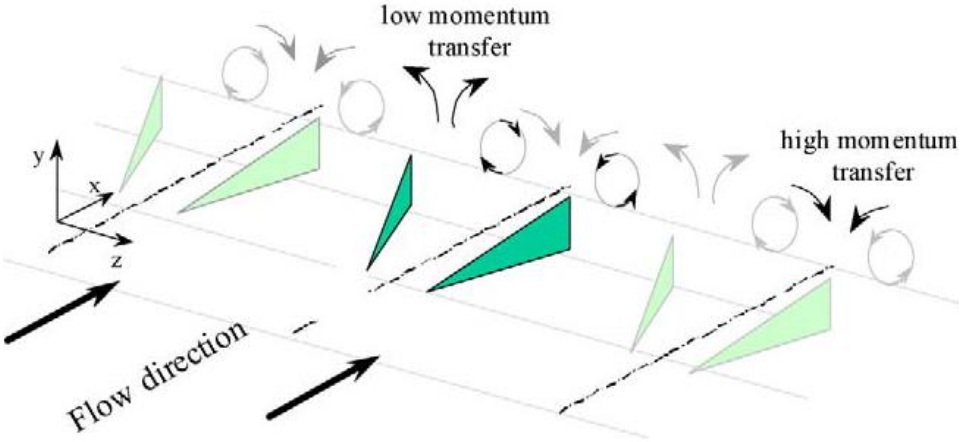

Figure 2.21 : Counter – rotating arrays of vane vortex generators

Co – rotating array transports low momentum fluid upward (away from the wall) and high momentum fluid downwards between two adjacent streamwise vortices (figure 2.22). For small values of spanwise spacing, these opposite phenomena reduce the effectiveness and persistence of the vortices. Besides, a co – rotating array of vortices induces its own spanwise displacement by self induction while developing downstream. A major advantage of co – rotating system is that, usually, vortices do not move away from the surface.

Paths of the vortices play a significant role in the mixing effect. CoR array produces mixing over a more spanwise range than a CtR array, however, the rate of mixing in a CtR array is much higher and skin friction is found to be 100% larger than in CoR array.

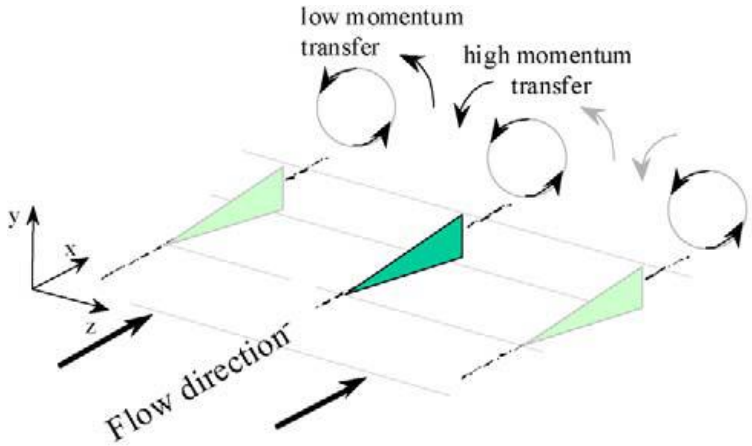

Figure 2.22 : Co – rotating (CoR) arrays of vane vortex generators

Counter – rotating array tends to be more effective in controlling predominantly 2D, streamwise flow separation, while for three – dimensional, spanwise separation (on swept wings or inside compact duct inlets) co – rotating array performs better. CtR array is more efficient in short distances, while CoR is less effective in immediate downstream region, but its vortices are able to persist further downstream than in CtR solution.

Counter – rotating arrangement is primarily implemented where a more complete suppression of the actual separation is necessary, for separations on ailerons and for other uses in which a greater maximum effectiveness is required.

The relative insensitivity of the effectiveness of co – rotating array to local flow direction makes them particularly suitable for swept wings. In fact, co – rotating arrangement is preferred for applications with strong boundary layer cross – flow, such as swept wings at cruise condition when a natural spanwise boundary – layer drift occurs, hence, to give a reduction to the component of the wing pressure drag that is due to BL growth. Another point is the redirection of the flow from locations where BL separation is highly undesirable (control surface on an aircraft wing).

Biplane or alternate pair array of vane VGs

Represents a combination of two counter – rotating arrays (CU and CD) in the same row (figure 2.23). Vortices originating from d_2 system of vanes tend to move downward (towards wall surface), while vortices generated by d_1 system tend to move upward (away from the wall). As a result, vortices of d_1 system go below vortices of d_2 system ('upper' vortices) and most of the pertinent mixing is then carried by d_1 system ('lower' vortices). Upper vortices tend to improve the mixing and help in removal of low energy air that is thrown up by the lower vortices further into the stream. Biplane array accelerates normal development of paths of lower vortices and reduces vertical and lateral drifts of both vortex systems.

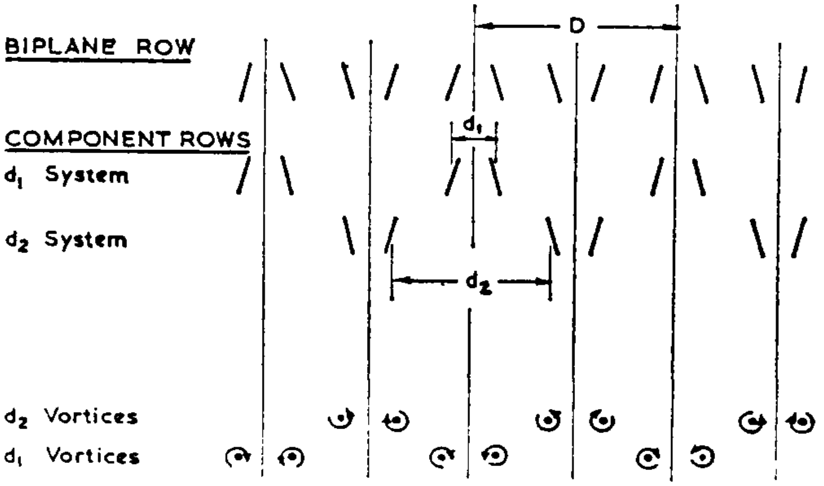

Figure 2.23 : Biplane or alternate pair system of vane VGs

However, this is achieved at the expense of damping between adjacent vortices, which implies a reduced effective streamwise range. Additional problem of local obstruction to the flow, hence, the "spoiler" effect and severe device drag (more vanes are present), can be reduced by staggering the two rows, preferably with the d_2 system just ahead of the d_1 system.

Biplane vortex generators are probably best designed by choosing first a CtR array to suit the particular application in mind and then adding the second CtR array. The interaction effect can be controlled to some extent by altering the relative vortex strength of the two systems, preferably by increasing that of d_1 – system relative to that of d_2 – system.

Addition of extra VGs required to convert a regular CtR array with large *D/d* to a biplane system nearly always results in some increase in maximum effectiveness. When *D/h* is small the range of effectiveness might be reduced. With large *D/h*, the range is not curtailed very significantly. However, the magnitude of improvement is never very large and is gained only at the expense of extra drag.

Single vs. multiple or tandem rows of vane VGs

Effective streamwise range could be increased by adding one or multiple rows of vanes at suitable distance from the first row. However, drag of the whole installation increases significantly and there are certain practical difficulties as well. Vortex generators of the second row have either to be carefully placed laterally to allow the vortices from the front row to pass between them or to be far enough downstream to allow them to pass over the top of VGs ; if this is not met, vortices from both rows are weaker from second row onwards.

This mutual interference between the vortices of tandem rows is even more difficult to avoid for CoR arrays because of the lateral displacement of vortices. However, multiple rows are seldom necessary, since CoR arrays generate vortices strong enough to be relatively streamwise persistent.

Zhang et al. [] determined the best option for second row of vane VGs is the same lateral position as the first row (figure 2.24). Second row is a remedy only for post – stall behavior of the clean airfoil, as lift coefficient is drastically improved. However, at angles of attack prior to stall, C_L is decreased. Single row doesn’t cure the deep – stall region, but C_{Lmax} and lift coefficient in pre – stall as well as in mild – stall region are higher than the effect of two rows (figure 2.25).

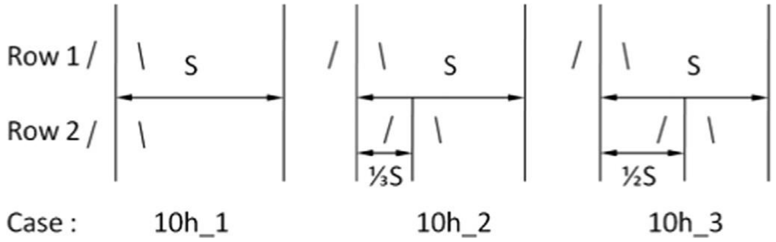

Figure 2.24 : Options for the second row of VGs

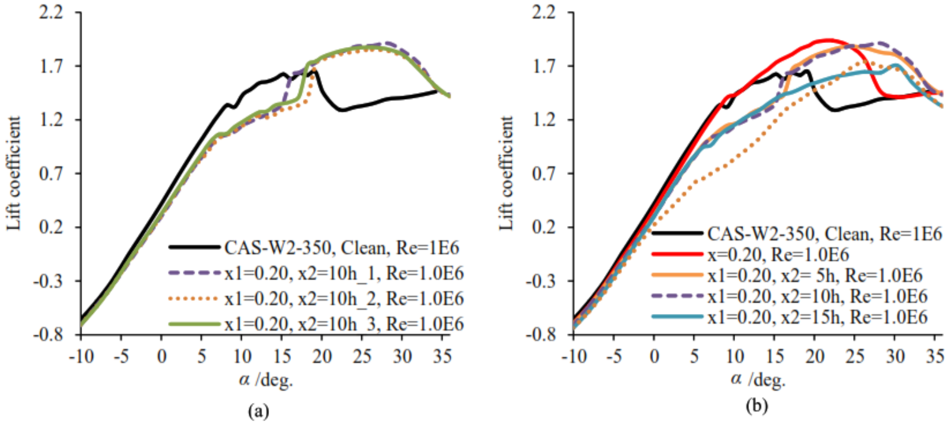

Figure 2.25 : Effects of lateral (a) and longitudinal position (b) of 2nd row of VGs on lift coefficient of CAS – W2 – 350 airfoil, an extract from [16]

Comparison of planform geometries – shapes of vane VGs

Physical quantities that describe vortex dynamics are vortex strength (represented by either peak vorticity or circulation), vorticity decay rate, longitudinal and lateral trajectories and dimensions of vortex core.

Vortex strength is inversely proportional to vane aspect ratio (or directly proportional to vane relative length l/h). Lower aspect ratio causes stronger vortices and larger aspect ratio creates weaker vortices due to predominantly 2D behavior of the flow along the vane height (except near the tip). One way of decreasing aspect ratio for a given planform shape and height is increasing vane length (very appealing as downstream vortex range increases). However, longer vane turns out to generate larger vortex cores that are, as such, prone to early viscous dissipation. Additionally, device drag increases when planform surface increases. Balance between high and low aspect ratio should be sought and in [15] suggest AR = 0.5 (or l/h = 2) for triangular vanes in APG. Another way of decreasing aspect ratio is increasing vane taper (i.e. increase in upper vane edge). This is also beneficial for vortex stability (i.e. steadiness of vortex strength and position with changing flow conditions). However, greater taper ratio increases device drag (larger planform surface as sweepback is decreased), so compromise must be reached in this approach as well.

The choice of vane planform also depends on the value of local Mach number and is certainly influenced by Mach number greater than 1. In this case it is desirable that vane is free from shock wave effects at the vane tip and presence of sweep angle seems useful.

Most complete description of planform geometry influencing vortex dynamics is obtained experimentally. It is possible to make use of study by H.J.Shim et al. [17] where wake characteristics of vane VG attached to a flat plate were extracted through stereo – PIV measurements in cross flow planes positioned downstream (figure 2.26). Only basic planform geometries had been investigated : triangular or delta, trapezoidal or cropped – delta and rectangular vane.

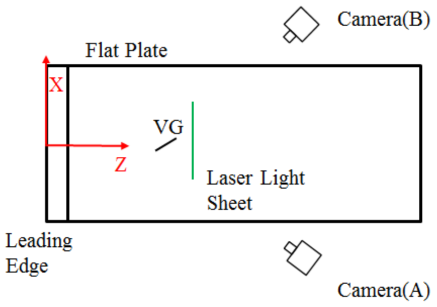

Figure 2.26 : Schematic of measurement system

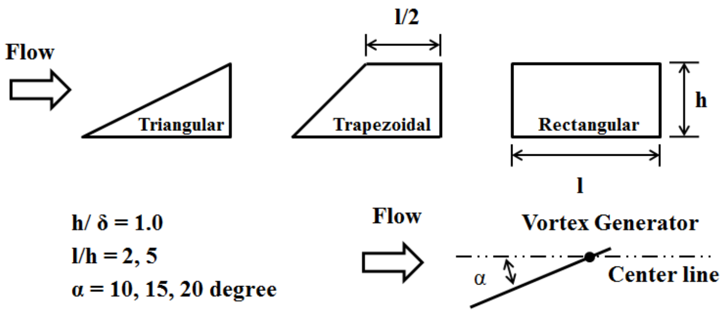

Figure 2.27 : Basic geometries of vane vortex generators and test conditions

Firstly, the most apparent conclusions are drawn by referring to the results on wake characteristics of basic vane geometries (listed in Appendix A) :

- initial vortex of rectangular vane has the greatest size and triangular vane generates the smallest size vortex
- for l/h = 2 rectangular vane generates the highest peak vorticity at all β ; triangular vane generates higher peak vorticity than trapezoidal, contrary to theoretical expectations, however, the values are obtained in ZPG condition (flat plate)
- for l/h = 5 rectangular vane generates the highest peak vorticity only at $\beta = 10°$, while at 15° and 20° the largest peak vorticities are induced by trapezoidal and triangular vanes, respectively ; this is explained by viscous dissipation taking place very early (due to size of vortex cores) with rectangular vane at β = 15°, whereas at 20° dissipation happens very early with trapezoidal vane as well
- vortex decay is influenced by vane length and inflow angle, but no general tendency is captured ; it also depends on the vane shape
- vertical position of streamwise vortex center is higher at all downstream stations for rectangular and trapezoidal vanes than with triangular vane.

Secondly, special table is created by listing all vortex parameters and parameters describing vane geometry. Relations between the parameters are then carefully identified and inserted in the table.

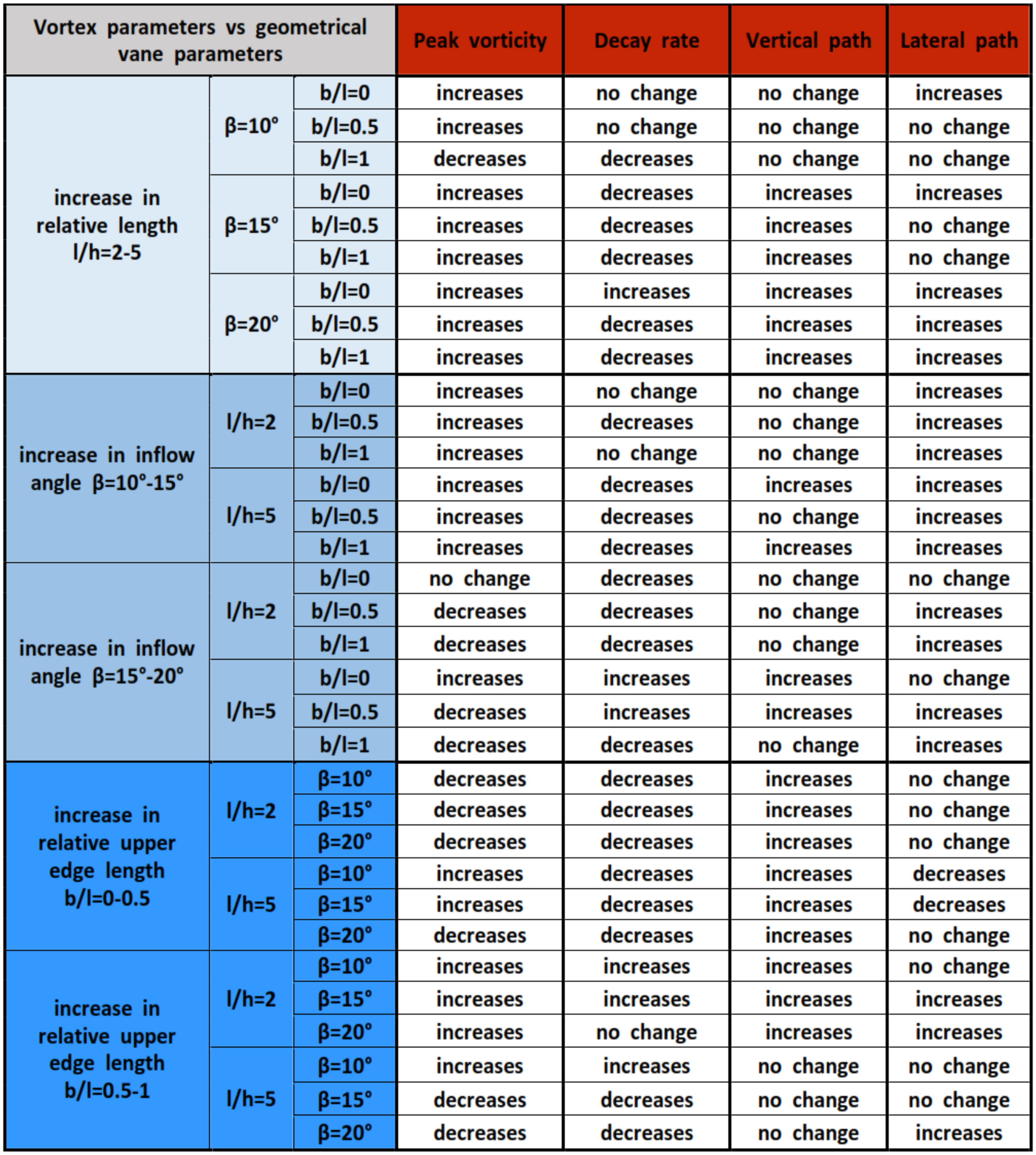

Vortex parameters vs geometrical vane parameters			Peak vorticity	Decay rate	Vertical path	Lateral path
increase in relative length l/h=2-5	β=10°	b/l=0	increases	no change	no change	increases
		b/l=0.5	increases	no change	no change	no change
		b/l=1	decreases	decreases	no change	no change
	β=15°	b/l=0	increases	decreases	increases	increases
		b/l=0.5	increases	decreases	increases	no change
		b/l=1	increases	decreases	increases	no change
	β=20°	b/l=0	increases	increases	increases	increases
		b/l=0.5	increases	decreases	increases	increases
		b/l=1	increases	decreases	increases	increases
increase in inflow angle β=10°-15°	l/h=2	b/l=0	increases	no change	no change	increases
		b/l=0.5	increases	decreases	no change	increases
		b/l=1	increases	no change	no change	increases
	l/h=5	b/l=0	increases	decreases	increases	increases
		b/l=0.5	increases	decreases	no change	increases
		b/l=1	increases	decreases	increases	increases
increase in inflow angle β=15°-20°	l/h=2	b/l=0	no change	decreases	no change	no change
		b/l=0.5	decreases	decreases	no change	increases
		b/l=1	decreases	decreases	no change	increases
	l/h=5	b/l=0	increases	increases	increases	no change
		b/l=0.5	decreases	increases	increases	increases
		b/l=1	decreases	decreases	no change	increases
increase in relative upper edge length b/l=0-0.5	l/h=2	β=10°	decreases	decreases	increases	no change
		β=15°	decreases	decreases	increases	no change
		β=20°	decreases	decreases	increases	no change
	l/h=5	β=10°	increases	decreases	increases	decreases
		β=15°	increases	decreases	increases	decreases
		β=20°	decreases	decreases	increases	no change
increase in relative upper edge length b/l=0.5-1	l/h=2	β=10°	increases	increases	increases	no change
		β=15°	increases	increases	increases	increases
		β=20°	increases	no change	increases	increases
	l/h=5	β=10°	increases	increases	no change	no change
		β=15°	decreases	decreases	no change	no change
		β=20°	decreases	decreases	no change	increases

Table 2.2 : Summary of relations between vortex parameters and geometrical vane parameters according to results of H.J.Shim et al. [17]

Particular set of vane vortex generators that also drives attention are vanes of alternative planform geometry. It consists of gothic, parabolic and ogive vane VGs (figure 2.28). Gothic shape is created by blending a 40° initial leading edge sweep. Ogive shape has the same area as delta VG, but the leading edge is smoothed by a sinusoidal curve. As the name suggests, parabolic planform follows parabolic curve along its upper edge.

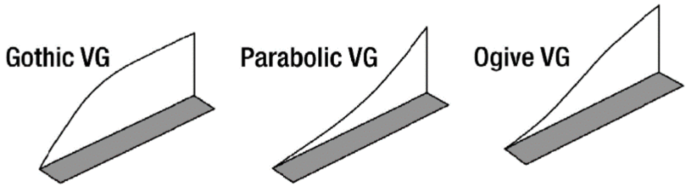

Figure 2.28 : Alternative shapes of vane type VGs

The inverse proportionality between vortex strength and aspect ratio applies to alternative shapes as well. Accordingly, gothic vane is the most suitable, while parabolic vane generates the weakest vortices. Parabolic shape also affects the stability of vortices due to zero – length of tip chord. This is also true for ogive shape, but to a lesser extent.

Unfortunately, performance comparison studies between basic and alternative vane VG shapes are sparse, therefore, little can be said on the advantages and drawbacks of implementing alternative planform geometries. As there are no sharp points present, gothic vane VGs produce more stable vortices and less device drag than popular trapezoidal VGs and represent frequent passive control solutions for aerodynamic surfaces.

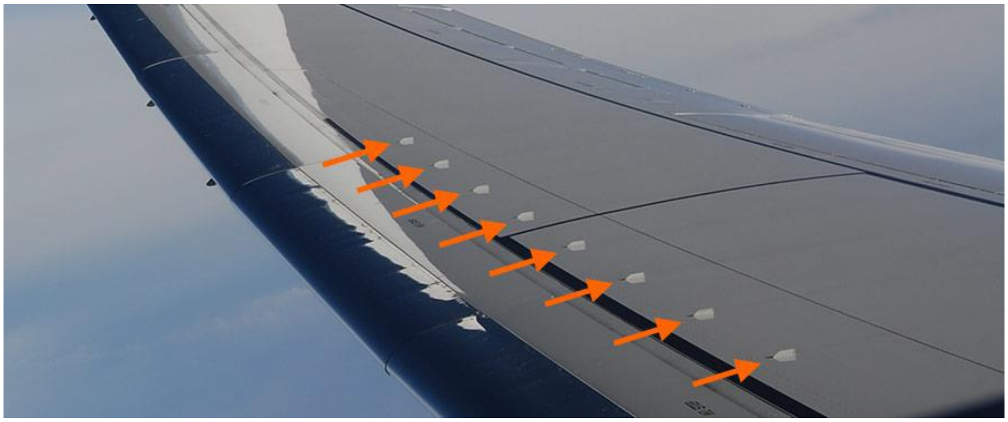

Figure 2.29 : Gothic vane vortex generators on aircraft wing

Aerodynamically shaped vs. classically shaped cross – section of vane VGs

Particular pressure distribution of aerodynamic shape generates weaker and smaller vortices compared to vortices of classical vanes. Vortices exhibit lower lateral and vertical paths, meaning high predictability of streamwise movement and greater skin friction coefficient, respectively. Aerodynamically shaped VGs (figure 2.30) produce more stable vortices, observed by non – oscillating vertical paths in BL. Airfoil cross – – section also ensures lower device drag than flat plate cross – section, since this shape exhibits less flow separation. Depending on the airfoil cross – section of vane VG, a risk of flow instability may exist, as laminar bubbles tend to appear on the suction side of certain airfoils. These can be controlled by careful adjustment of the inflow angles and inspection of the separation between vanes in VG pair.

In general, chordwise placement of vortex generators depends on whether the goal is only a high C_{Lmax} or also C_L/C_D matters. Often, VGs are used to increase lift at the inner sections where drag is less important, but by maintaining C_L/C_D close to clean airfoil VGs can be used further outboard (e.g. to prevent the outboard sections going in and out of stall in turbulent wind gusts, resulting in C_L that is close to C_{Lmax} and a blade of smaller chord). In an appropriate configuration, classically shaped vane VGs increase C_{Lmax} and α_{crit}, but C_L/C_D is decreased due to additional drag. According to Hansen [19], it is undoubtedly possible to obtain a distinctly higher C_{Lmax} and α_{crit} by using aerodynamically shaped VGs, but also to achieve maximum aerodynamic efficiency comparable to clean airfoil.

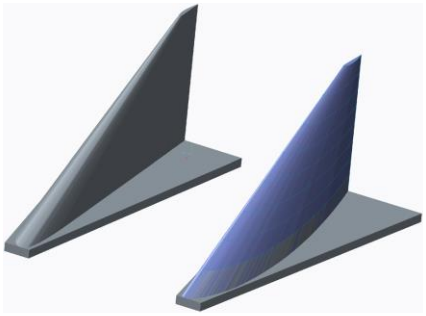

Figure 2.30 : CAD drawing of aerodynamically shaped VGs – – trapezoidal vanes of high aspect ratio

Comparisons of various classes of vane vortex generators have led to more or less genuine results as far as array configurations are considered. Vane VGs are positioned in a single row array that can be arranged in two ways : counter – rotating (CtR) or co – rotating (CoR). Counter – rotating array has two orientations, one with shorter distance between trailing edges of VG pair → common – upwash (CU) and one where shorter distance is between leading edges of VG pair → common – downwash (CD) array. Things are not straightforward with the choice of vane planform geometry. While the array type (CtR – CU, CtR – CD, CoR) depends on the specific purpose of the flow control device (beginning of section 2.5), the correct choice among triangular (delta), trapezoidal (cropped – delta), rectangular or some alternative shape of vane VGs is best determined through a particular parametric analysis. Widespread implementation of aerodynamically shaped vortex generators might represent a future trend, but nowadays they remain largely unexplored and should be subject of more experimental and numerical investigations.

Of course, the performance of passive control device also depends on array parameters. These are determined through similar analyses as well, however, certain trends can be captured by considering recent applications that may serve as guidelines for the actual investigation. This is the subject of the next section.

Configuration parameters of vane vortex generators :

- geometric parameters :
    - planform geometry
    - height h
    - length L
    - cropped edge length b
    - inflow (or incindence) angle β
- array parameters :
    - array type
    - chordwise placement $\left(\frac{x}{c}\right)_{VG}$
    - intra – vane spacing d
    - inter – vane spacing D

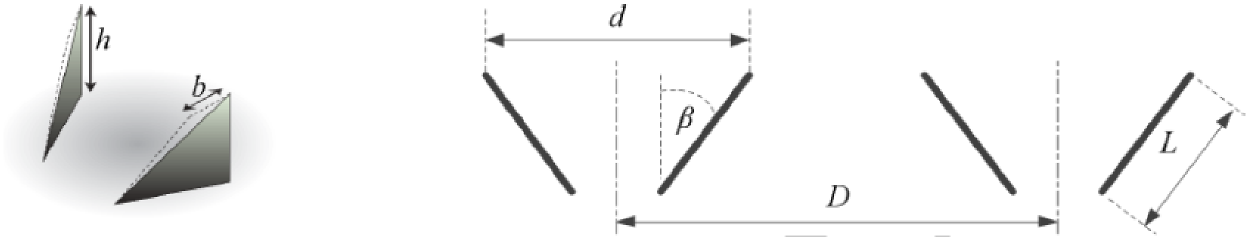

Figure 2.31 : Schematic of triangular vane VG array with configuration parameters

2.6 Airfoil application of vane vortex generators

Figure 2.32 is an example of a wind turbine blade. As already explained in section 1.1, different airfoils are installed as cross – sections from the blade root to tip. The most apparent geometrical feature that varies along the blade span is airfoil thickness.

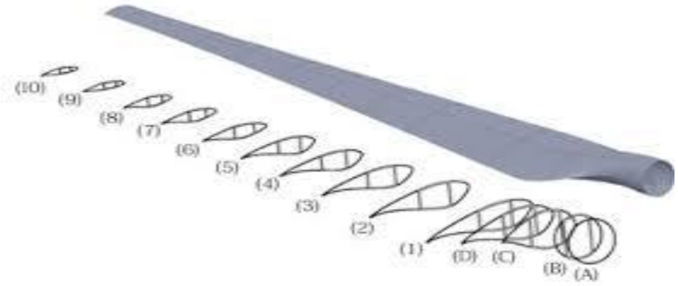

Figure 2.32 : Wind turbine blade and airfoils corresponding to blade cross sections

The idea is to inspect the available parametric analyses on airfoils equipped with vane VGs for each thickness family and try to extract general trends for parameters of configurations of vane VGs. For that purpose, table 2.5 was created to summarize the relevant studies. In order to have a more precise comparison of different parametric studies, similarity parameter of Reynolds number needs to be of the same order of magnitude for each case (table 2.6). Ideally, airfoil geometry (referring to relative thickness and airfoil family) should also be taken into account. However, this turned out to be possible for two or three airfoils only, which had been already situated in the first table. In several cases, airfoil performance data improved by the use of VGs are either not complete or not available.

In this manner, we focus on airfoil types equipped with passive flow control devices, in the range of 18 – 35% relative thickness, which are indicative of cross – sections in each blade region. The considered airfoils are (next page) :

- **$(d/l)_{max} = 15\%$:**
  - NACA 4415
- **$(d/l)_{max} = 18\%$:**
  - NACA $63_{(3)}$ – 418
  - NACA $63_{(3)}$ – 618
- **$(d/l)_{max} = 21\%$:**
  - DU 93 – W – 210
  - NREL S809
- **$(d/l)_{max} = 25\%$:**
  - DU 91 – W2 – 250
- **$(d/l)_{max} = 30\%$:**
  - DU 97 – W – 300
  - FFA – W3 – 301
- **$(d/l)_{max} = 35\%$:**
  - CAS – W2 – 350
  - FFA – W3 – 360

Airfoil	Re	Vane geometry	Vane array	$(x/c)_{VG}$ [%]	h/c [%]	l/h	β [°]	d/h	D/h	ΔC_{Lmax}	$\Delta\alpha_{critical}$ [°]	$\Delta(C_L/C_D)_{max}$
NACA 4415*	215000	trapezoidal	single row CtR-CD	20	3.333	3	20	3	5			
NACA $63_{(3)}$-418	3000000	triangular	single row CtR-CD	60	0.833	2	18	2.5	6	0.22	-2	9
NACA $63_{(3)}$-618	1200000	triangular	single row CtR-CD	20	1.667	2.1	18	3	8	0.41	6.5	-14
_DU 93-W-210_	1000000	triangular	single row CtR-CD	20	0.625	3.4	20	5	10	48.77%	10	821.86%
NREL S809	1000000	rectangular	double row CtR-CD	10 & 40	1	2.1	18	3	6	0.61	4	
_DU 91-W2-250_	900000	triangular	single row CtR-CD	20	0.5	2	18	3	5		7.95	
_DU 97-W-300_	2000000	trapezoidal	single row CtR-CD	20	0.769	3	12	3.5	7			
FFA-W3-301	3000000	triangular	single row CtR-CD	20	1	3.8	15.5	7	9	0.85	6.5	
CAS-W2-350	1000000	triangular	single row CtR-CD	20	0.625	4.1	14	4	8			
FFA-W3-360	3000000	triangular	single row CtR-CD	20	1	3.8	15.5	7	9	0.9	7	

Table 2.3 : Summary of parametric analyses of controlled airfoil flows presented in section 2.6

Airfoil	Re	Vane geometry	Vane array	$(x/c)_{VG}$ [%]	h/c [%]	l/h	β [°]	d/h	D/h	ΔC_{Lmax}	$\Delta\alpha_{critical}$ [°]	$\Delta(C_L/C_D)_{max}$
NACA $63_{(3)}$-618	1200000	triangular	single row CtR-CD	20	1.667	2.1	18	3	8	0.41	6.5	-14
_DU 93-W-210_	1000000	triangular	single row CtR-CD	20	0.625	3.4	20	5	10	48.77%	10	821.86%
NREL S809	1000000	rectangular	double row CtR-CD	10 & 40	1	2.1	18	3	6	0.61	4	
_DU 91-W2-250_	900000	triangular	single row CtR-CD	20	0.5	2	18	3	5		7.95	
CAS-W2-350	1000000	triangular	single row CtR-CD	20	0.625	4.1	14	4	8			

Table 2.4 : Summary of parametric analyses of controlled airfoil flows of same order of magnitude of Reynolds number

Table 2.5 supported by more precise table 2.6 point to several notable patterns in the application of vane vortex generators on an airfoil :

- single row, counter – rotating, common – downwash (CtR – CD) is the dominant array
- triangular (delta) and trapezoidal (cropped – delta) vanes are the dominant geometries
- the most common chordwise placement is 20%
- maximum relative height is 3.33% (h = 5mm) meaning that low – profile vortex generators are preferred
- relative length or vane aspect ratio is in the range $\frac{l}{h} = 2 - 4$
- inflow angle or incidence angle is in the range $\beta = 12° - 20°$
- relative intra – vane spacing is in the range $\frac{d}{h} = 3 - 7$
- relative inter – vane spacing is in the range $\frac{D}{h} = 5 - 10$
- for $\frac{d}{h} = 3 - 5$ it is not uncommon to have as a trend $\frac{D}{h} = 2\frac{d}{h}$

These deductions should be taken with great caution. It is always wise to perform parametric analysis on the application of specific vane VG on particular airfoil in order to obtain a clear picture of the influence of passive control device on aerodynamic behavior. The ranges of values obtained by this critical analysis should serve as starting points for experimental / numerical investigation and as worthy hints as to which values should parameters of optimal VG configuration have by as the result of parametric study.

Chapter 3 - Experimental benchmark

3.1 Wind tunnel facility and airfoil model

Research analysis that serves as experimental benchmark for the thesis is the article "Experimental parameter study for passive vortex generators on a 30% thick airfoil" by D. Baldacchino et al [25].

The DU 97 – W – 300 airfoil was tested in the closed loop, low turbulence tunnel at Delft University of Technology. The test section is octagonal, measuring 1.80m x 1.25m and 2.60m long. The model had a chord c = 0.65m, a thick trailing edge of 1.7 % chord and spanned the height of the test section, giving an aspect ratio of approximately 1.92. A traversable wake rake for assessing the total drag was positioned approximately at 60% c downstream the airfoil trailing edge. All polars were acquired at $Re_c = 2 \cdot 10^6$ (M = 0.13), for which the tunnel turbulence levels were below 0.1%. Model blockage in the test section was around 10% near C_{Lmax} for the uncontrolled airfoil. Polars were acquired in the smooth or free (natural) transition regime, as well as in rough or forced transition. The latter was enforced using ZigZag (ZZ) tape (figure 3.2) on airfoil upper surface along the entire span. Thickness of this strip was 0.17 mm, with a width of 11 mm and its leading edge fixed at 5% chord from the airfoil leading edge.

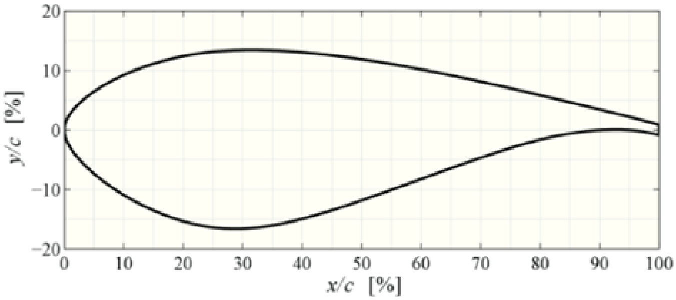

Figure 3.1 : DU 97 – W – 300 model profile

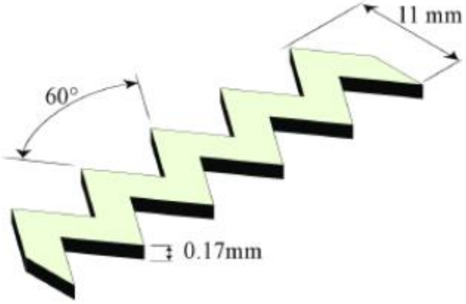

Figure 3.2 : ZigZag tape geometry

As already noticed, the data gathering was conducted in two flow regimes in order to mimic more realistically the real operating conditions : smooth and rough blade regime. Smooth blade means a new, clean blade, with a perfectly smooth surface finish, so that transition from laminar to turbulent boundary layer takes place spontaneously – free or natural transition. Rough blade regime is justified by degradation of blade surface finish through time. Turbine blade faces atmospheric agents and impacts from various particles that eventually worsen the quality of the surface. A blade with a rough surface promotes the tripping of BL because of flow instabilities due to newly created micro – cavities. This way, stall onset is very likely to occur, which is detrimental to aerodynamic performance of the blade and wind turbine in general, as explained before.

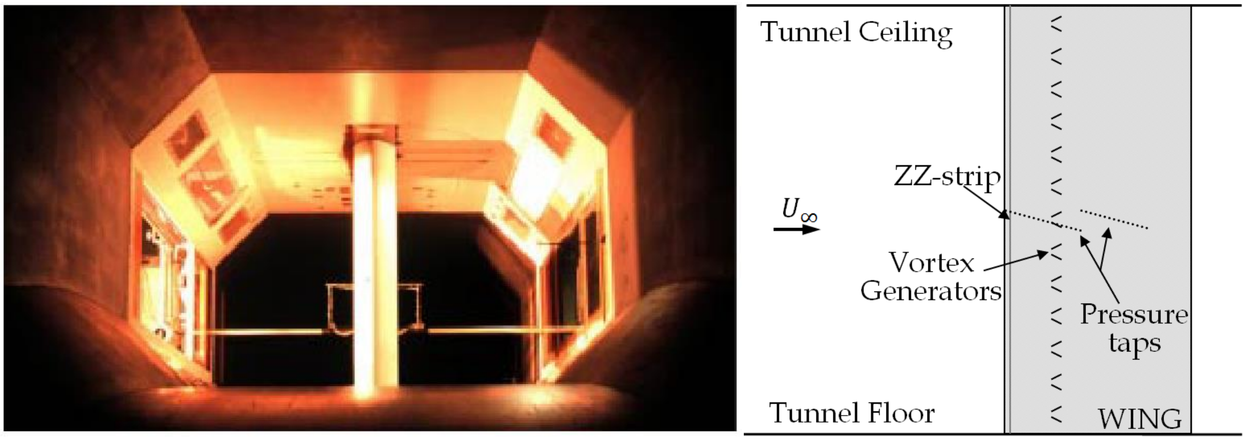

Figure 3.3 : Test – section and setup schematic for DU97 – W – 300 airfoil

The normal and tangential airfoil loads (C_N and C_T) were determined through the model and wake rake pressure measurements, acquired through a DTC INITIUM data acquisition system. A total of 102 surface pressure taps surrounded the airfoil model, including one in the mid – section of the blunt trailing edge. The wake rake was fitted with 67 total pressure and 16 static pressure tubes. Lift coefficient was evaluated with :

$$C_L = \frac{C_N}{\cos\alpha} - C_D \tan\alpha$$

where C_D was determined from the wake rake or model pressure drag. The final lift and drag coefficients were obtained after modification through wind tunnel corrections for model and wake blockage as well as streamline curvature.

3.2 Vortex generator configurations

The following robust base design for separation control was defined :

- $h \approx \delta$, $L = 3h$, $\beta = \pm 15°$, delta wing planform at $x/c = 20\%$, measured between the airfoil and VG strip leading edges
- $d = 3.5h$, $D = 7h$, counter – rotating, common downwash (CtR – CD) array

Design variants were obtained by modifying these parameters relative to the base design. Three vane heights were investigated, with an additional smaller ($h/\delta < 1$) and larger ($h/\delta > 1$) variant. These were in turn tested at different chordwise positions, in the range $10\% < x/c < 50\%$, within clean and rough conditions. The remaining variants were only measured in a clean boundary layer at $x/c = 20\%$, with vane angles $10° < \beta < 25°$ and vane lengths $2h < L < 5h$. A cropped – delta variation was designed such that $b = 0.2L$, resulting in a 20% increase of the vane planform. The configuration was also varied with a larger spacing $D = 10h$, and ensuing CoR and CtR common upwash variants.

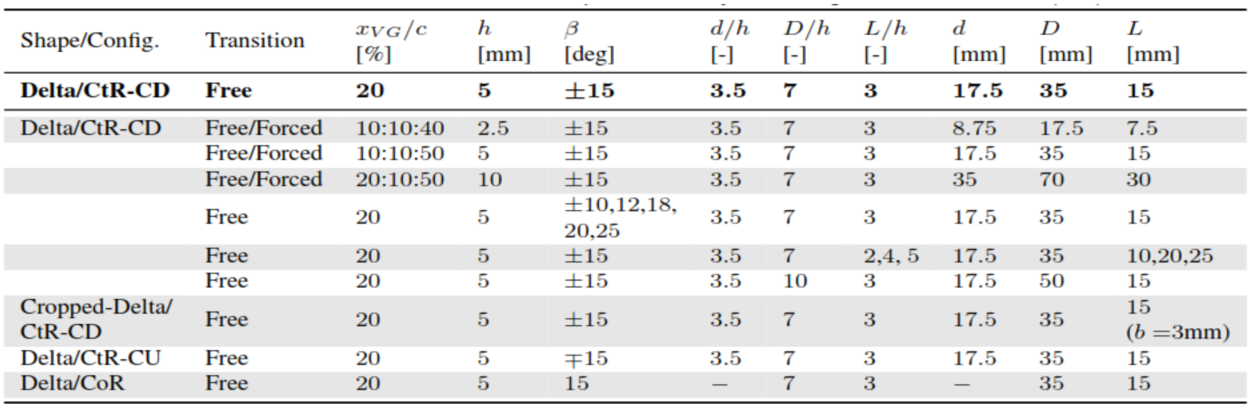

Shape/Config.	Transition	x_{VG}/c [%]	h [mm]	β [deg]	d/h [-]	D/h [-]	L/h [-]	d [mm]	D [mm]	L [mm]
Delta/CtR-CD	**Free**	**20**	**5**	**± 15**	**3.5**	**7**	**3**	**17.5**	**35**	**15**
Delta/CtR-CD	Free/Forced	10:10:40	2.5	± 15	3.5	7	3	8.75	17.5	7.5
	Free/Forced	10:10:50	5	± 15	3.5	7	3	17.5	35	15
	Free/Forced	20:10:50	10	± 15	3.5	7	3	35	70	30
	Free	20	5	$\pm 10,12,18,$ 20,25	3.5	7	3	17.5	35	15
	Free	20	5	± 15	3.5	7	2,4, 5	17.5	35	10,20,25
	Free	20	5	± 15	3.5	10	3	17.5	50	15
Cropped-Delta/ CtR-CD	Free	20	5	± 15	3.5	7	3	17.5	35	15 (b =3mm)
Delta/CtR-CU	Free	20	5	∓ 15	3.5	7	3	17.5	35	15
Delta/CoR	Free	20	5	15	–	7	3	–	35	15

Table 3.1 : Dimensions of different VG configurations (base design in bold)

Referring to specific RFOIL calculations, based on BL displacement and momentum thickness δ^* and θ, the final sizing was arbitrarily referred to $(\alpha, x/c) = (16°, 20\%)$ position, residing ahead of the separation line, where $\delta \approx 3.8$mm. Due to manufacturing constraints, VG heights of 2.5, 5 and 10mm were chosen.

The vortex generator profiles were individually formed and attached to mounting strips, spanning the length of the wing. The vanes and mounting strips were manufactured from 0.2mm spring steel and material thickness was accounted for VG heights.

3.3 Concluding statement

Inspection of experimental results of different VG configurations (table above) allowed Mosca [30] to specify the parameters of an optimal VG configuration. Therefore, parameter values correspond to no single configuration, but result from the whole set of experimentally tested VG pairs. Optimal vane VG configuration is given by :

- geometric parameters :
  - trapezoidal or cropped – delta vane
  - height h = 5mm
  - length L = 3h = 15mm
  - cropped edge length b = 0.2L = 3mm
  - inflow or incidence angle $\beta = \pm 12°$
- array parameters :
  - chordwise position $\left(\frac{x}{c}\right)_{VG} = 20\%$
  - intra – vane spacing d = 3.5h = 17.5mm
  - inter – vane spacing D = 7h = 35mm

In the long run, CFD simulation of flow around airfoil equipped with optimal VG array should be realized. For the purpose of this thesis, it is sufficient to try to simulate flow around airfoil equipped with VG array that is most similar to the optimal configuration and was actually tested in wind tunnel. Ideally, the whole AoA range should be simulated, however, the main focus is on pre – stall and post – stall behavior where the most complicated flowfield is expected. The configuration which differs from the optimal one by the least of parameters is case 038 from [27]. The only difference is the value of vane inflow angle β and the state of free BL transition (clean condition) instead of forced transition (tripped condition – fully turbulent BL), which is more realistic everyday scenario.

Case 038 VG configuration is given by (see Appendix C for experimental data) :

- geometric parameters :
  - trapezoidal or cropped – delta vane
  - height h = 5mm
  - length L = 3h = 15mm
  - cropped edge length b = 0.2L = 3mm
  - inflow or incidence angle $\beta = \pm 15°$
- array parameters :
  - chordwise position $\left(\frac{x}{c}\right)_{VG} = 20\%$
  - intra – vane spacing d = 3.5h = 17.5mm
  - inter – vane spacing D = 7h = 35mm

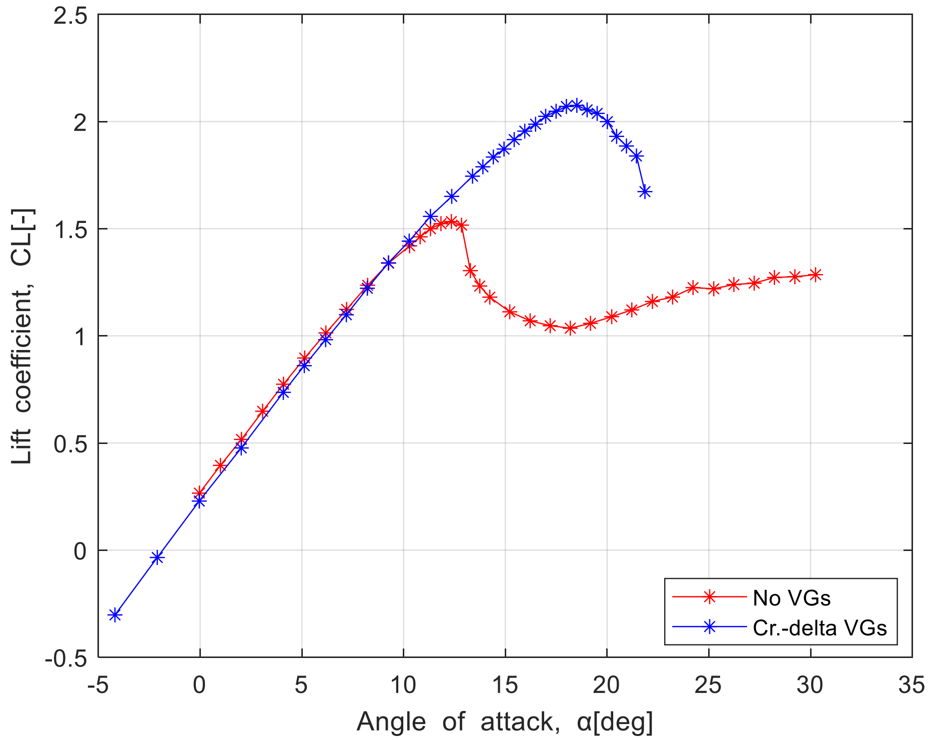

Figure 3.4 : Lift coefficient curves for clean and airfoil with cropped – delta VGs (cases 001 and 038 respectively, free BL transition [27])

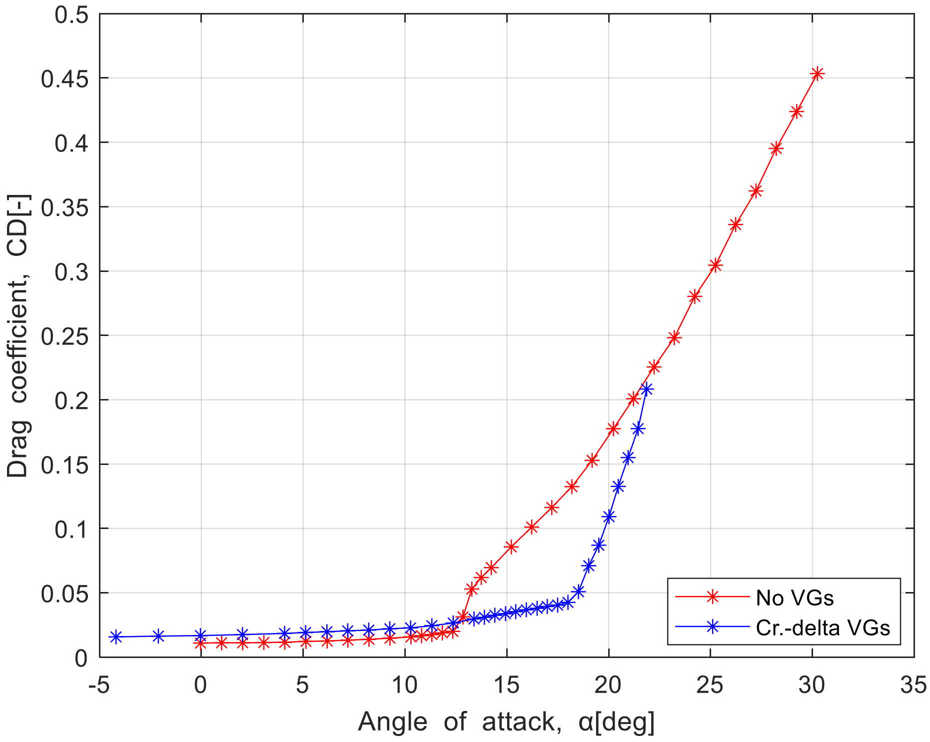

Figure 3.5 : Drag coefficient curves for clean and airfoil with cropped – delta VGs (cases 001 and 038 respectively, free BL transition [27])

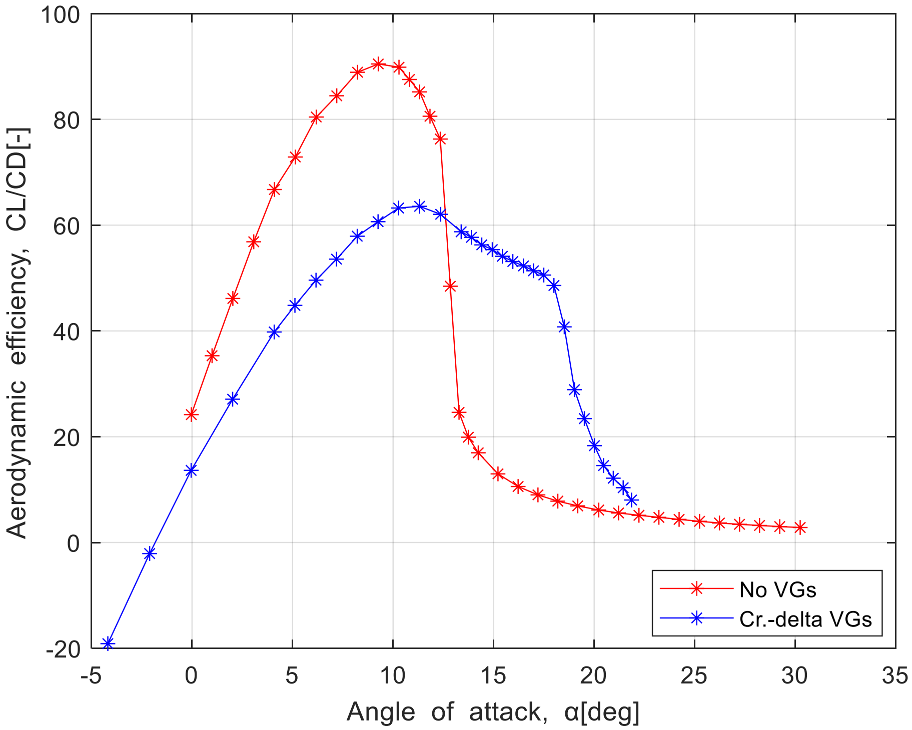

Figure 3.6 : Aerodynamic efficiency curves for clean and airfoil with cropped – delta VGs (cases 001 and 038 respectively, free BL transition [27])

Chapter 4 - CFD background

4.1 Governing equations for viscous flow

Every fluid motion can be described by conservation laws. Conservation laws are physical statements in the form of partial differential equations (PDEs) and represent a starting point of every analytical and numerical investigation. They are the following :

- **conservation of mass :** mass of a fluid body in conserved → **mass balance equation** (***continuity equation***)
- **conservation of** (**linear**) **momentum :** the rate of change of linear momentum of a fluid body is equal to the sum of external forces acting on fluid body (***Newton's Second Law***) → **momentum balance equation** (***Navier – Stokes*** (***NS***) ***equations***)
- **conservation of** (**total**) **energy** : the rate of change of total energy of a fluid body is equal to the sum of the rate of change of heat to / from and the rate of change of work done on / by fluid body (***First Law of Thermodynamics***) → **energy balance equation**

Mass and energy balance equations contain only scalar quantities, whereas momentum balance equation is in vector form or expressed by three scalar equations (for each direction). Conservation laws form a system of five PDEs supplemented by auxiliary conditions (initial (ICs) and boundary conditions (BCs)). The system becomes mathematically closed by introducing Stokes hypothesis on shear stress (indicative of Newtonian fluid) and thermal and calorical equations of state, thus, a system of seven equations with seven unknown variables (i.e. flow quantities) is achieved.

In the study of incompressible flow, pressure and velocity fields are found by considering only mass and momentum balance equations. If the flow is isothermal (no heat transfer is present), the system consists of four PDEs that correspond to four unknowns – velocity components for each direction u_i ($i = 1,2,3$) and pressure p (assuming constant viscosity μ and negligible body forces) :

$$\frac{\partial u_i}{\partial x_i} = 0$$

$$\frac{\partial u_i}{\partial t} + \frac{\partial}{\partial x_j}\left(u_i u_j\right) = -\frac{1}{\rho}\frac{\partial p}{\partial x_i} + \nu \frac{\partial^2 u_i}{\partial x_j^2}$$

Computational fluid dynamics (CFD) makes use of conservation law equations through finite volume method (FVM). This way, set of differential equations is transformed into a set of algebraic equations that are far more appropriate for the processor to solve.

4.2 Turbulent flow simulation methods

There are three simulation methods for turbulent flow (figure 4.1) :

- Direct Numerical Simulation (DNS)
- turbulence models for Reynolds – Averaged Navier – Stokes (RANS) equations → → RANS method
- Scale – Resolving Simulation (SRS)

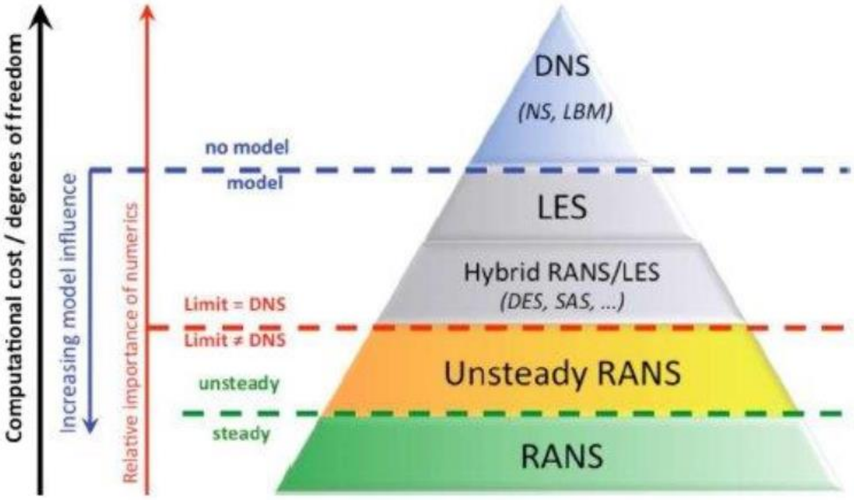

Figure 4.1 : Hierarchy of turbulence simulation methods

Direct Numerical Simulation (**DNS**) provides full description of turbulent flow (mean flow and all turbulent velocity fluctuations) by solving the unsteady Navier – Stokes equations on spatial grids that are sufficiently fine to resolve the Kolmogorov length scales (scales at which energy dissipation takes place) and with time steps sufficiently small to resolve the period of the fastest fluctuations. Using DNS, flow quantities usually not available in experiments are easily computable and various turbulence models can be tested. On the other hand, very high order methods employed in the process have very low flexibility and robustness, while computational costs as well as memory storage requirements are proportional to Re^{3}. Also, initial and boundary conditions have to be specified for all resolved scales.

Given the fact that DNS is feasible only for simple geometries at low turbulent Re, it is a versatile research tool only, not suitable for practical, industrial flow computations. Some of the largest DNSs to date are the simulation of homogeneous isotropic turbulence (HIT) at Re = 13.700 with $69 \cdot 10^{9}$ points on spatial grid and turbulent channel flow at Re = 90.000 with approximately $18 \cdot 10^{9}$ grid points.

RANS method is focused on the mean flow and the effects of turbulence on mean flow properties. Before numerical methods, Navier – Stokes equations are averaged wrt time or Reynolds – averaged, giving rise to extra terms in the new set of equations due to interactions between turbulent fluctuations. These terms are called Reynolds, turbulent or 'eddy' stresses and require additional equations in order to have a closed system. The manner in which additional PDEs are formed is called turbulence modeling.

RANS method allows flow symmetry to be fully exploited and is the only solving approach where steady state solutions are achievable (e.g. steady 2D flow). On the other hand, accuracy for certain classes of flow can be an issue. According to Menter [29], RANS models have shown their strength essentially for wall – bounded flows where the calibration based on the law – of – the – wall provides a sound foundation for further refinement. Their performance is far less accurate for free shear flows (simple self – similar flows, flows with strong swirl, massively separated flows (deep airfoil stall), etc.). Troublesome result interpretations of unsteady state computations are not uncommon.

Unlike DNS, computational cost and memory requirements only loosely depend on Re and low order numerical methods (such as second – order) are feasible. However, previous method directly deals with governing equations, whereas in RANS approach all turbulent fluctuations are modeled. Moreover, models are expected to represent even the geometry – dependent, energy – containing, possibly anisotropic large scales (model tuning is required). Still, RANS method remains as the most widely used approach for simulation of industrial flows and the most investigated turbulence solution technique.

The effects of fluctuations on the mean flow are assessed by using Reynolds decomposition, through which Reynolds – averaged Navier – Stokes equations are derived (again, constant viscosity and negligible body forces are assumed) :

$$\frac{\partial U_i}{\partial x_i} = 0$$

$$\frac{\partial U_i}{\partial t} + \frac{\partial}{\partial x_j}\left(U_i U_j\right) = -\frac{1}{\rho}\frac{\partial P}{\partial x_i} + \nu \frac{\partial^2 U_i}{\partial x_j^2} + \frac{1}{\rho}\left[\frac{\partial}{\partial x_j}\left(-\rho\overline{u_i' u_j'}\right)\right]$$

Closure of the system of equations is achieved by adding a specific number of equations that balance off the newly – formed turbulent or Reynolds stresses τ_{ij}^t. The process of turbulence modeling is realized by either of the following approaches :

- Boussinesq hypothesis → turbulent stresses are proportional to mean rates of deformation and stresses are expressed in terms of dynamic turbulent (eddy) viscosity coefficient μ_t and specific turbulent kinetic energy k as the unknowns :

  $$\tau_{ij}^{t} = -\rho\overline{u_i' u_j'} = \mu_t\left(\frac{\partial U_i}{\partial x_j} + \frac{\partial U_j}{\partial x_i}\right) - \frac{2}{3}\rho k\delta_{ij}$$

  additional equations represent transport equations for k and flow quantities related to μ_t (mixing length l_m, viscosity parameter $\tilde{\nu}$, dissipation rates ε and ω) ; RANS models based on Boussinesq hypothesis (eddy viscosity models or first order models) are classified on the number of equations that are suplementing the starting set (zero – equation or algebraic, one – equation and two – equation models)

- stress transport models (second order models) → exact transport equations are formulated for all Reynolds stress components R_{ij} ; knowing that one equation must stand for turbulence dissipation rate ε , the total number of equations of turbulent model is seven ; classification is based on the nature of additional equations (algebraic or differential (PDEs)).

For the purpose of present work, two eddy viscosity or first order turbulence models are important :

- **Menter's $k-\omega$ SST (Shear Stress Transport) model** → extension of $k-\omega$ BSL (baseline) model by including viscosity limiter μ_t that allows more accurate calculation of wall shear stress, hence better prediction of flow separation on surface in adverse pressure gradient (e.g. airfoil) ; previously, BSL version was developed to address high sensitivity of solution values obtained with standard $k-\omega$ model to free – stream values of turbulence intensity and length scale (applied at inlet) :

  $$\frac{\partial}{\partial t}(\rho k) + \frac{\partial}{\partial x_j}(\rho k U_j) = \frac{\partial}{\partial x_j}\left[\left(\mu + \frac{\mu_t}{\sigma_k}\right)\frac{\partial k}{\partial x_j}\right] + P_k - D_k$$

  $$\frac{\partial}{\partial t}(\rho\omega) + \frac{\partial}{\partial x_j}(\rho\omega U_j) = \frac{\partial}{\partial x_j}\left[\left(\mu + \frac{\mu_t}{\sigma_\omega}\right)\frac{\partial\omega}{\partial x_j}\right] + P_\omega - D_\omega + C_\omega$$

  where σ stands for Prandtl number, P is production term, D dissipation term and C is the so – called "cross – diffusion" term that arises from the mathematical procedure used to obtain the ω equation ; the main purpose of the model lies in external aerodynamics and turbomachinery problems at high Reynolds numbers

- **transition SST or $\boldsymbol{\gamma - \overline{Re}_{\theta,t}}$ model** → derived by coupling the equations of $k - \omega$ SST model with two other transport equations, for turbulent intermittency γ (percentage of time that turbulent fluctuations are locally present in BL, being zero in laminar part and one in fully turbulent region, therefore it is used to control the development of flow transition) and transition onset criteria in terms of momentum – thickness Reynolds number $\overline{Re}_{\theta,t}$:

$$\frac{\partial}{\partial t}(\rho\gamma) + \frac{\partial}{\partial x_j}(\rho\gamma U_j) = \frac{\partial}{\partial x_j}\left[\left(\mu + \frac{\mu_t}{\sigma_\gamma}\right)\frac{\partial\gamma}{\partial x_j}\right] + P_\gamma - D_\gamma$$

$$\frac{\partial}{\partial t}(\rho\overline{Re}_{\theta,t}) + \frac{\partial}{\partial x_j}(\rho\overline{Re}_{\theta,t}U_j) = \frac{\partial}{\partial x_j}\left[\left(\mu + \frac{\mu_t}{\sigma_{\theta,t}}\right)\frac{\partial\overline{Re}_{\theta,t}}{\partial x_j}\right] + P_{\theta,t}$$

where P_γ stands for production term that controls the length of transition region, D_γ stands for dissipation term that allows BL to re – laminarise by dissipating intermittency fluctuations and $P_{\theta,t}$ is another production term ; the starting equations for k and ω are modified in the sense that production and dissipation terms in k – equation are altered as well as blending function inside ω – equation ; this way, the model is able to implement $k - \omega$ SST approach in fully turbulent flow region and still account for turbulent nature in the laminar and transition BL segments (figure 4.2).

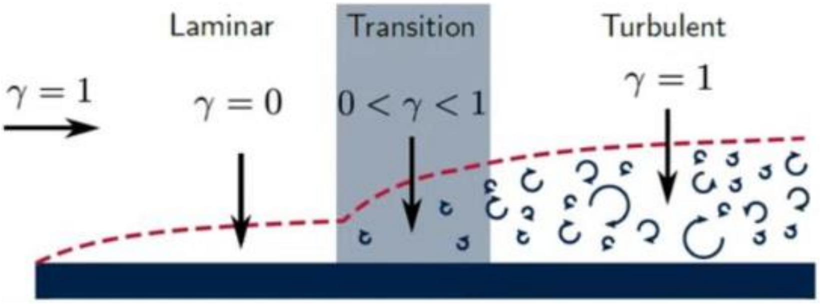

Figure 4.2 : Regions of boundary layer on a flat plate and corresponding values of turbulent intermittency

Transition SST turbulence model is mainly intended for aerodynamics and turbomachinery problems at moderate Reynolds numbers ($\sim 10^5$). However, the model is successfully employed at high Reynolds numbers ($\sim 10^6$) at lower angles of attack of controlled flow around airfoil in free BL transition (Mosca [30]) and can be considered for near – stall angles in the same regime. On the downside, transition SST model is one of the most expensive turbulence models in terms of computational cost per iteration, alongside Reynolds Stress Model (RSM) and transition $k - kl - \omega$ model.

Scale – Resolving Simulation (**SRS**) is the third method for turbulence simulation, seen as a way to bypass the flaws of RANS approach. Namely, SRS is capable of providing additional information that RANS simulation is not, even in case where RANS model is, in fact, capable of computing the correct time – averaged flow field (e.g. acoustic simulations, vortex cavitation, etc.). Secondly, the lack of accuracy, which is evident even with the most advanced Reynolds Stress Models (RSM) when used for basic self – similar free shear flows, is circumvent.

The most apparent novelty with SRS is **Large Eddy Simulation** (**LES**), which has been the most widely used SRS model for couple of decades. It is an approach that deals with resolving only the large turbulent scales and models the small ones. Such concept is justified by the fact that large scales are problem – dependent and difficult to model, whereas smaller scales become more and more universal and isotropic and can be modeled easily. The actual procedure starts with filtering of unsteady Navier – Stokes equations over a finite spatial region (e.g. grid volume) that is aimed at only resolving the portions of turbulence larger than the filter width (i.e. grid size). Basically, the finer the grid, the finer the dimension of resolved eddies. Filtered Navier – Stokes equations for incompressible flow (assuming constant viscosity and negligible body forces) are :

$$\frac{\partial \overline{U}_i}{\partial x_i} = 0$$

$$\frac{\partial \overline{U}_i}{\partial t} + \frac{\partial}{\partial x_j}\left(\overline{U}_i\,\overline{U}_j\right) = -\frac{1}{\rho}\frac{\partial \overline{P}}{\partial x_i} + \frac{1}{\rho}\left(\overline{\tau}_{ij} + \tau_{ij}^{LES}\right)$$

$$\tau_{ij}^{LES} = \rho\overline{U}_i\,\overline{U}_j - \rho\overline{U_i U_j}$$

The additional sub – grid stress tensor, despite the difference in derivation, is modeled like in RANS approach using a first order model :

$$\tau_{ij}^{LES} = \mu_t\left(\frac{\partial \overline{U}_i}{\partial x_j} + \frac{\partial \overline{U}_j}{\partial x_i}\right)$$

Employing a first order model, filtered NS equations become identical to RANS equations with turbulence stresses modeled according to Boussinesq hypothesis. Therefore, the same momentum balance equations are used for RANS, LES or some intermediate mode, which depends on the level of eddy viscosity coming from a corresponding turbulence model. This is a huge benefit that marks the basis for the creation of hybrid RANS – LES models.

Classical LES model that is most widely used is the Smagorinsky model from 1963 (Δ is a measure of grid size, S the strain rate scalar and C_S is a constant) :

$$\mu_t = \rho(C_S\Delta)^2 S$$

whose main deficiency is that eddy viscosity does not go to zero for laminar flows, hence, model also requires a near – wall damping function in viscous sublayer of turbulent BL. Several models that take this into account have been developed (such as WALE model).

LES is not an appropriate tool for wall – bounded flows at moderate to high Re. The reason is that boundary layer thickness reduces with Reynolds number, making room for smaller and smaller scales that need to be resolved by LES. Small turbulent scales demand high grid resolution near the wall, thus causing LES to be prohibitively expensive in terms of computational cost. Coping with such resolution doesn't mean available computers lack the capacity to perform the computations, only that necessary CPU time and memory requirements make such simulations beyond routine, everyday usage. The situation for low Re is often equally unfavorable, since the effects such as laminar – – turbulent transition take place and have to be captured.

LES is most versatile when used for simulating free shear flows with small scales of low importance and industrial flows not involving wall boundary layers, in other words, wall – bounded flows in strongly reduced geometries, preferably at low Re. Basically, wherever small turbulent scales are irrelevant or not present at all, LES might be an appropriate tool. At relatively low Re, LES can be useful in turbomachinery for analysis of flows of blade cooling holes or air – jet vortex generators (AJVG). Also, there are flows of very low Re where LES method is applied. Here, boundary layers are likely laminar and turbulence forms only in separated fluid layers and detached flow regions (e.g. flow around valve).

Other SRS models can be roughly termed as **hybrid or combined RANS – LES models**, which are not new models in the strict sense, but allow the combination of existing turbulence solvers in different portions of the flowfield. This way, it is possible to define models for accurate simulation of wall – bounded shear flows, with RANS model employed for boundary layer and LES for external flow (SAS, DES, SDES, SBES models, etc). When only boundary layers are analyzed, Wall – Modeled LES (WMLES) is useful, which applies a RANS model to the innermost part of wall BL and LES to the main part. For large domains, it is frequently necessary to cover only a small portion with SRS models, while the majority of the flow is captured by employing RANS approach. In such cases, Zonal or Embedded LES (ZLES, ELES) are applied as they allow beforehand specification of the region where LES is required.

S.Passoni had successfully implemented DES and SDES models for flow simulation around 30% thick airfoil for cases with and without vortex generators [31].

Detached Eddy Simulation (**DES**) was the first SRS model utilized for industrial purpose. Its convenience lies in the ability to switch between RANS turbulence model for the region of boundary layer and LES mode for the region of free shear flow, based on the grid resolution provided. Essentially, the switch criterion is :

$$C_{DES}\Delta_{max} > L_t \ \rightarrow \ RANS$$

$$C_{DES}\Delta_{max} \leq L_t \ \rightarrow \ LES$$

$$\Delta_{max} = max(\Delta_x, \Delta_y, \Delta_z) \rightarrow \text{maximum edge length of local cell}$$

For boundary layer this criterion states that RANS approach is preserved as long as boundary layer thickness is lower than maximum edge length ($\Delta_{max} > \delta$, satisfied by the implemented mesh). This limiter embodied in L_t is included in numerical solution process through dissipation term Y_k inside k – equation of a corresponding two – equation first order model :

$$E_{DES} = \rho \frac{k^{3/2}}{min(L_t, C_{DES}\Delta_{max})} = \rho \frac{k^{3/2}}{L_t min(1, C_{DES}\Delta_{max}/L_t)} = \rho \frac{k^{3/2}}{L_t} max\left(1, \frac{L_t}{C_{DES}\Delta_{max}}\right)$$

Unfortunately, DES limiter can be activated by grid refinement inside attached boundary layer, thus causing flow separation at various locations, depending on the grid spacing. This is called Grid – Induced Separation (GIS) and is the reason behind the formulation of **Delayed – Detached Eddy Simulation** (**DDES**), regardless of RANS model employed. DDES introduces function F_{DDES} that enables better control of switching between RANS and LES modes ($F_{DDES} = 1$ inside BL and $F_{DDES} = 0$ away from the wall):

$$E_{DDES} = \rho \frac{k^{3/2}}{L_t} max\left(1, \frac{L_t}{C_{DES}\Delta_{max}}(1 - F_{DDES})\right)$$

However, also the limit for DDES is frequently reached and GIS once again poses a serious problem. Solution may be found in **Shielded Detached Eddy Simulation** (**SDES**) that makes use of an additional sink term in the k – equation (not modifying an existing sink term as in case of DES and DDES) and includes a shielding function f_S :

$$\varepsilon_{SDES} = \rho\beta^* k\omega F_{SDES}$$

$$F_{SDES} = max\left(\frac{L_t}{C_{SDES}\Delta_{SDES}}(1 - f_S), 1\right) - 1$$

Shielding function f_S is formulated so that it provides essentially asymptotic shielding on any grid. This function enables much stronger shielding than F_{DDES}, which implies that natural shielding of the model based on the mesh length definition Δ can be reduced. However, strong f_S might also pose a problem as it can prevent activation of LES mode inside separated flow with low turbulence levels (e.g. mildly stalled airfoil).

The length scale Δ_{max} can be problematic for cells with high aspect ratio where the spanwise grid spacing is much higher than in other two dimensions. This causes a slow transition from RANS to LES mode with turbulence being resolved later in the domain. In order to address this issue, the mesh length scale used in SDES becomes:

$$\Delta_{SDES} = max\left(\sqrt[3]{V}, 0.2\Delta_{max}\right)$$

Classical LES grid length scale corresponds to first value, whereas second is the maximum edge length (as in DES) multiplied by 0.2, so that maximum length is reduced five times and the influence of high aspect ratio is seriously limited. This more robust definition allows faster transition from RANS to LES, since $\Delta_{SDES} < \Delta_{max}$ and the condition $C_{SDES}\Delta_{SDES} \leq L_t$ that triggers LES mode is more likely to achieve than $C_{SDES}\Delta_{max} \leq L_t$.

4.3 Modern trends in numerical modeling of vortex generators

The most common methods for numerical modeling of vortex generators are :

- **Fully resolved approach** → geometry of VGs, represented as surfaces (zero – – thickness), is captured by flow domain mesh, becoming highly refined in the zone around the flow device ; naturally, this method comes at very high computational cost, but provides the most accurate results

- **BAY model** → developed by Bender, Anderson and Yagle (1999), it simulates the presence of VGs in computational domain by adding specific source terms (i.e. body forces) to momentum balance equations corresponding to those cells which accommodate the locations of VGs ; accordingly, there is no need for representing VG geometry in the mesh.

Apart from other roles, European project AdVanced Aerodynamic Tools for lArge Rotors – AVATAR was aimed to give a summary of state – of – the – art knowledge on modeling capabilities of flow control devices suitable for wind turbine application (task 3.1) [32]. The accuracy of CFD simulations of thick airfoil for 10+ MW wind turbines was compared with experimental results for both clean and controlled profile. As part of AVATAR, Baldacchino et al. [33] investigated the validity of several numerical codes, having experimental data of DU97 – W – 300 airfoil as benchmark. The solvers employed for numerical simulations of clean and controlled airfoil in tripped conditions were :

- **EllipSys** → an incompressible RANS solver with Menter's $k - \omega$ turbulence model that is able to simulate VGs with fully resolved approach → Ell – FR and with BAY model → Ell BAY ; one vane of a VG pair is simulated and a 3D, low aspect ratio ('strip') model is obtained

- **VGFlow** → Navier – Stokes equations are slightly modified which results in a system of vortex lines released from VG positions in order to simulate physical presence of devices ; the equations are spanwise averaged and a 2D problem is reached.

Chapter 5 - Pre – processing stage

5.1 Geometry and computational grid

There are four main categories of grid or mesh which covers the flow domain :

- structured
- block – structured
- unstructured
- hybrid .

Structured grid is the most straightforward grid category that is used to represent the solution domain. It consists of families of grid lines with the property that members of one family do not mutually intersect, but intersect each member of other families only once. In this manner, computational cells that provide the most accurate results are created. Moreover, the number of grid points surrounding an interior grid point or node is fixed, giving rise to high convergence rate. Structured grids are based on mapping of flow domain onto a computational domain of rather modest geometry. However, viable mapping for complex geometry often remains a burdensome and practically impossible process.

In an attempt to overcome difficulties experienced with a structured arrangement, **block – structured grid** can be employed for certain complex geometries. As the name suggests, solution domain is divided into regions or blocks, with each block meshed separately, possibly having different mesh structure and, in some cases, different coordinate system. Interfaces of adjacent blocks can have matching or non – matching grids on both sides that must be properly treated in a fully conservative manner (i.e. by proper interpolation of flow quantity values). If the blocks are mutually overlapping, such grid is named composite or chimera grid.

Unstructured grid exhibits no implicit structure of coordinate lines and is considered as the limiting case of block – structured type where each cell represents a block. Discrete control volumes take any polygonal/polyhedral shape, with no restrictions on the number of adjacent cells meeting at a point (2D problem) or along a line (3D problem). Mesh elements take triangular and quadrilateral shapes if 2D flow is analyzed, otherwise tetrahedral, pyramidal, prismatic and hexahedral elements are present. Introduction of unstructured mesh is justified by possibility of fitting flow domains of complex geometry, without spending a great deal of time on mesh generation and mapping (especially if triangular/tetrahedral mesh is expected). This is further simplified by automatic generation techniques originally developed for FEM, while mesh refinement and adaption are also simpler to perform.

Hybrid grid encompasses both triangular and quadrilateral (if 2D flow) or tetrahedral and hexahedral cells if 3D flow is simulated (structured + unstructured grid, basically). Quadrilateral/hexahedral cells can be imposed near wall surface for better resolution necessary for proper boundary layer representation, while triangular/tetrahedral cells can be employed in outer domain for more efficient computation process. Hybrid mesh is the mesh category of choice for the current flow simulation.

Flow simulations around an airfoil feature the two most common grid topologies :

- **CH – type** → flow domain is shaped as letter ‘C’ in the frontal portion, while grid refinement imitates letter ‘H’ in rectangular – shaped wake region (figure 5.1, left) ; although highly precise, the refinement extends to domain boundaries and causes excessively large number of cells, making CH – type a relatively expensive option
- **O – type** → flow domain is shaped as a circle around the airfoil or as letter ‘O’ (figure 5.1, right) ; grid is refined towards the airfoil, therefore it doesn’t affect the number of cells in the way it does for CH airfoil grid.

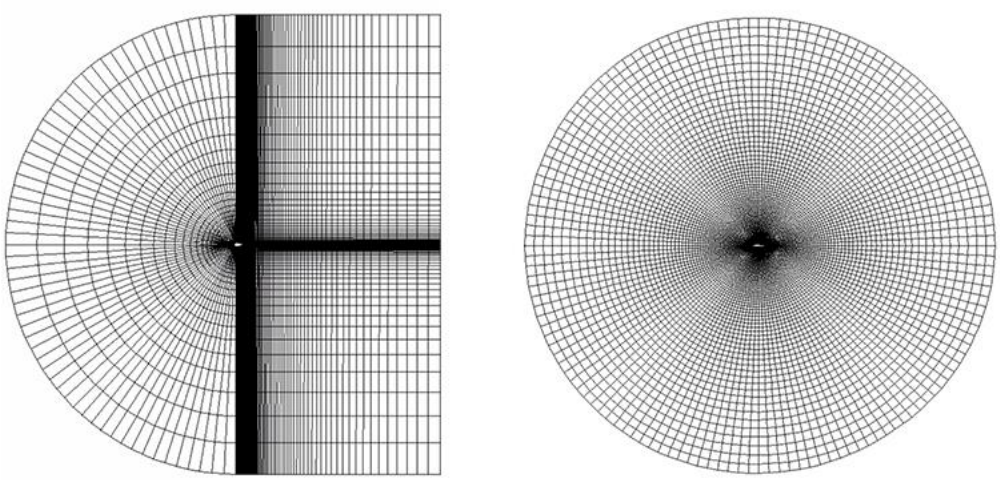

Figure 5.1 : The most common airfoil grid topologies : CH – type and O – type

Garbaruk et al. [34] with the help of ANSYS team managed to obtain the most accurate results for NACA 0021 airfoil at 60° by using SAS – SST model and O – type grid with hexahedral cells (AR = 4 with 1.9 million cells in total). In another work, Xu et al. [35] analyzed NREL S809 airfoil (used for wind turbines) for angles of attack up to 90°, employing DDES – SA model and O – type hexahedral mesh again (AR =1 with 860k cells). Chosen airfoil grids are in line with properties of different topologies explained above, hence O – type is the grid of choice also in this work.

The geometry has a diameter of 26 m, ensuring a diameter – to – chord ratio of 40, which is in line with best practice advice that a ratio greater than 30 is desired. Sufficiently high value of domain diameter allows proper development of all relevant flow structures that are essential for validity of flow variable values (accurate estimations of C_L and C_D).

Flow domain consists of two parts :

- **VG domain** → to avoid fully resolved meshing approach that would result in huge number of cells (since $h \sim \delta$), VGs were incorporated as zero – thickness surfaces inside two blocks of a structured, five block part ; the reason for having two blocks for vortex generators lies in their trapezoidal shape that is viewed as triangle + + rectangle, however both segments are meshed with very fine triangular cells inside flow volume discretized by triangular prisms (figure 5.3) ; non – conformal mesh interfaces are imposed onto boundaries of the part in order to avoid extensively high number of cells ; the part features spanwise resolution of 0.13% and first layer thickness as inflation option (first layer height 1.e – 005 mm, 6 maximum layers and 1.2 growth rate)

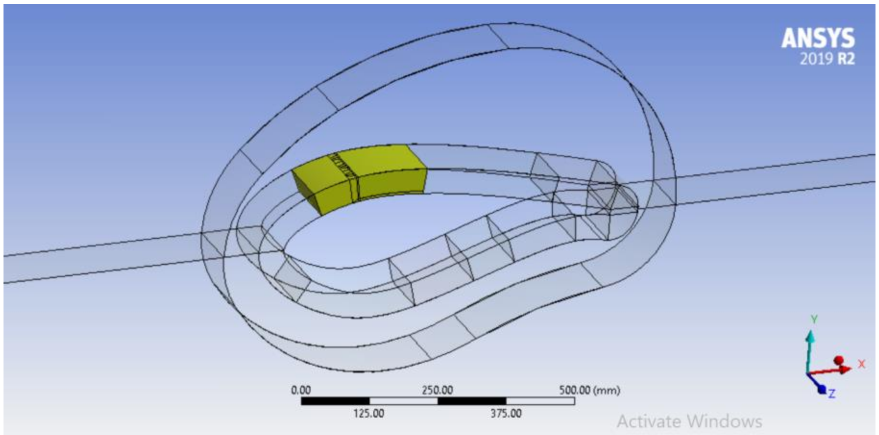

Figure 5.2 : Part VG domain

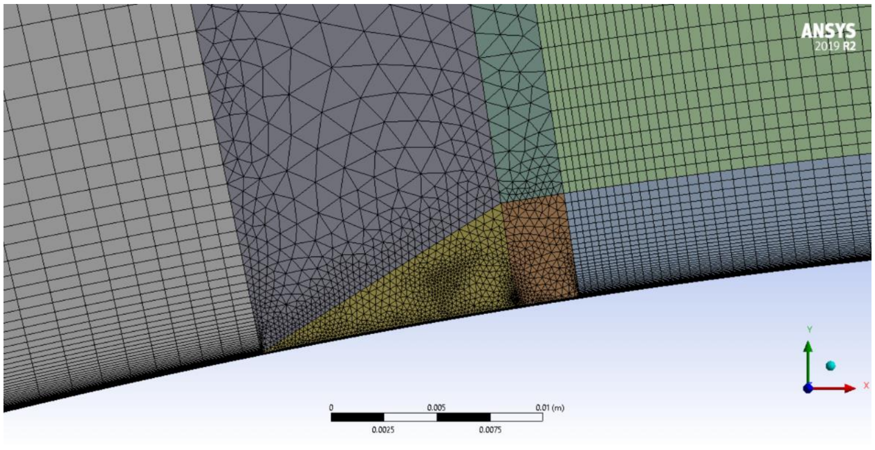

Figure 5.3 : Mesh around trapezoidal VGs

- **Domain** → majority of flow domain, consists of three subdomains :

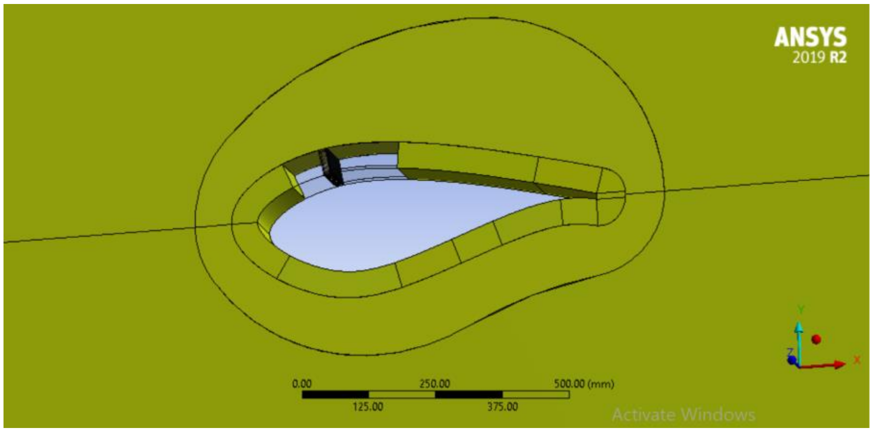

Figure 5.4 : Part Domain

- **inner** – entity comprising of 12 bodies, a block – structured mesh for a better fit inside the 5 cm thick region used to cover boundary layer ; the mesh is divided into 61 layer in the normal direction with a growth ratio of 1.1 ; the first element thickness is 0.01 mm, thus $y^+ \leq 2$ on average is assured ; the airfoil curvature has been discretized by elements of equal length of 5.85 mm, except for frontal part where edge sizing was imposed with element size of 6.5 mm

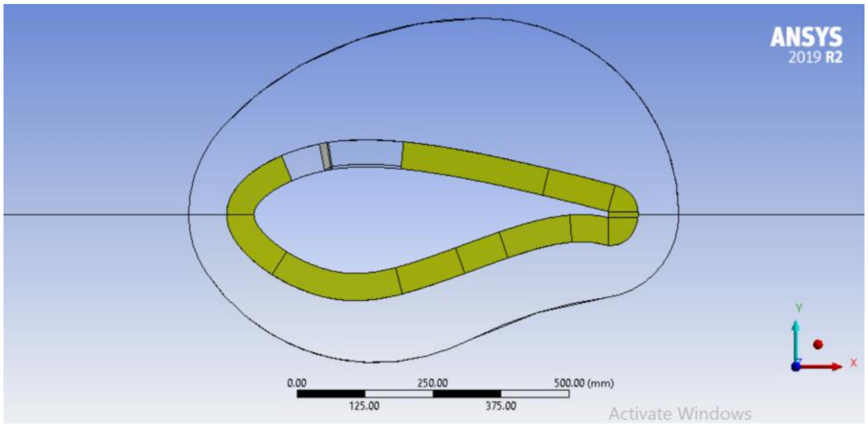

Figure 5.5 : Inner subdomain of Domain part

- **middle** – two bodies, an unstructured mesh whose cells tend to keep approximatelly the same size, necessary for correct turbulence simulation up to the same length scale in the whole subdomain ; since this is where flow detachment predominantly takes place, tubulence must be simulated on a thoroughly assessed grid, i.e. the growth ratio should not be too high as it may negatively affect the accuracy, as the resolved length scale becomes too coarse very fast

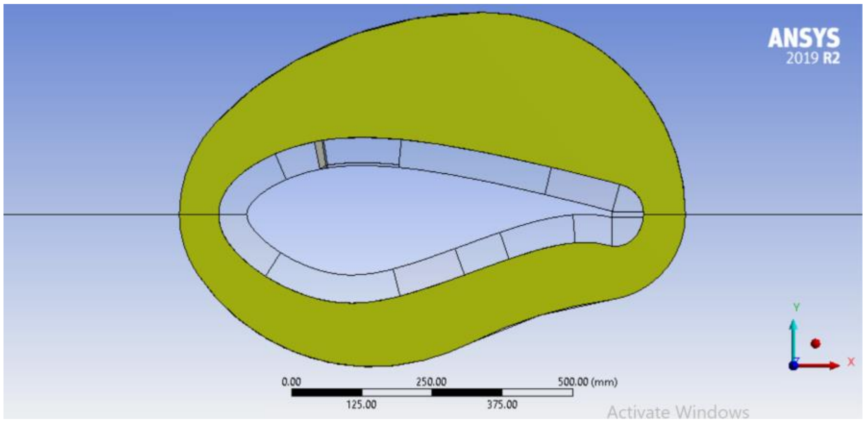

Figure 5.6 : Middle subdomain of Domain part

- **outer** – again two bodies, but structured, hexahedral mesh, with 62 layers in radial direction and a growth ratio of 1.08 to ensure slow mesh coarsening.

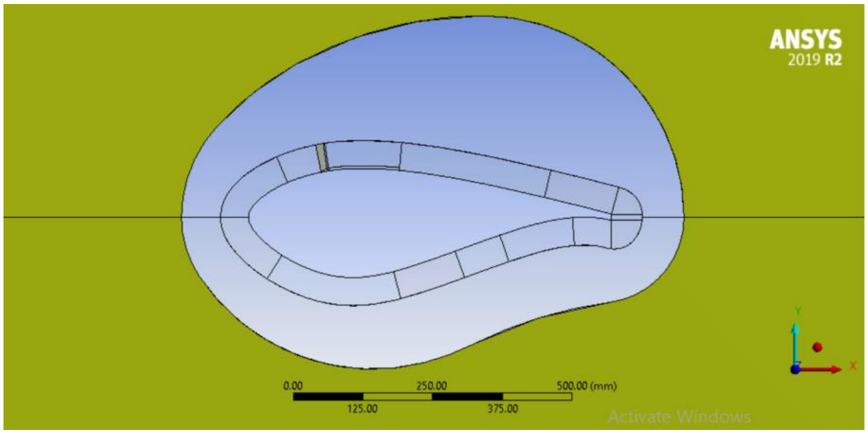

Figure 5.7 : Outer subdomain of Domain part

Although the entire geometry couldn't be covered, figure 5.8 displays the mesh domain with every block.

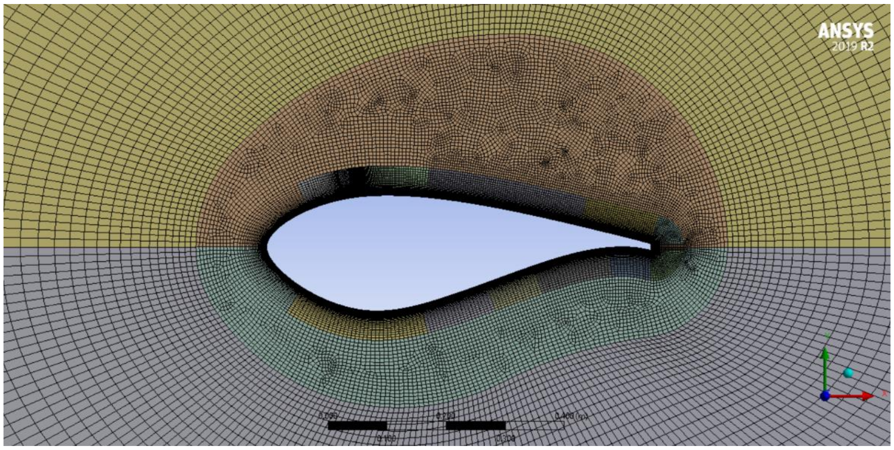

Figure 5.8 : Flow domain mesh used for simulation

Spanwise resolution of mesh retained resolution of 0.58% of chord length, a percentage already proven for controlled airfoil flow. Aspect ratio AR of the model is important for accurate evaluation of all quantities of interest, especially when SRS methods are utilized. If domain is too narrow, the formation of three – dimensional flow structures is jeopardized, while too wide domain is highly computationally expensive. Except at very high angles, airfoil equipped with vane VGs avoids the formation of larger turbulent structures due to vortices generated by control devices. An already established value of AR = 0.16 is adopted. This is represented by three VG pairs that implies span length of 0.105 mm (figure 5.9). As span width sensitivity analysis was necessary for angles higher than critical AoA, five more models of different aspect ratios were adopted. Table 5.1 gives a summary of most important mesh characteristics for created geometries.

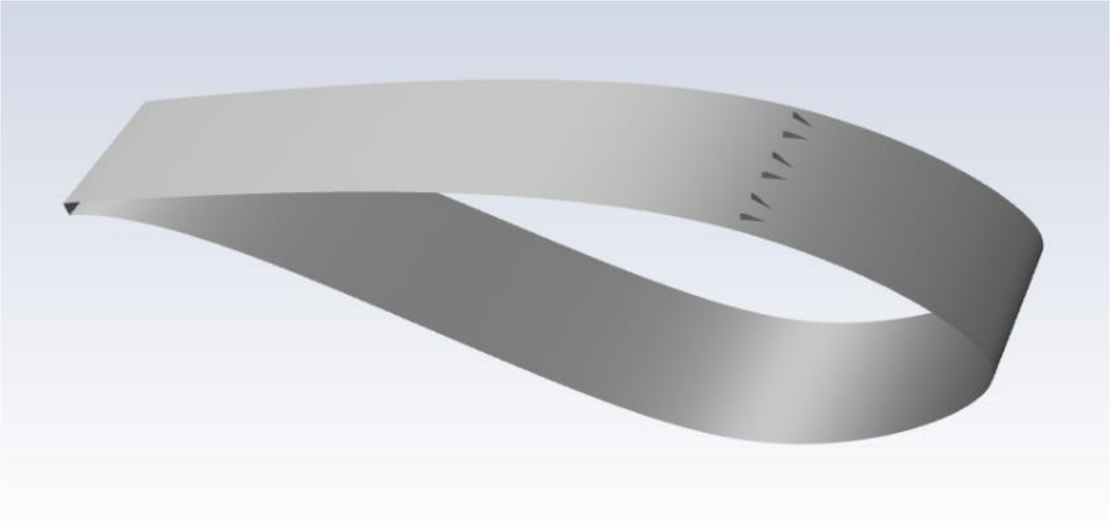

Figure 5.9 : Airfoil DU97 – W – 300 equipped with three pairs of cropped – delta vane VGs – AR = 0.16

Mesh characteristics	AR = 0.16	AR = 0.215	AR = 0.27	AR = 0.32	AR = 0.38	AR = 0.48
Span [mm]	650	650	650	650	650	650
Chord length [mm]	105	140	175	210	245	315
First Layer Thickness [mm]	0.01	0.01	0.01	0.01	0.01	0.01
No. of Z - elements in VG domain	120	160	200	240	280	360
Spanwise resolution in VG domain [%]*	0.1346	0.1346	0.1346	0.1346	0.1346	0.1346
No. of Z - elements	28	37	46	56	65	84
Spanwise resolution [%]**	0.5769	0.5821	0.5853	0.5769	0.5799	0.5769
No. of elements in VG domain	1079983	1271063	1610157	1769560	2083009	2726542
No. of elements	2192395	2747881	3444499	4010456	4683009	6081250

*,** - percentage of chord length

Table 5.1 : Mesh characteristics of airfoil geometries of different span

5.2 Mesh quality

Simulation results of flow variables are affected by quality of computational grid or mesh. In particular, poor quality mesh can jeopardize convergence speed and existence in general, not to mention too simple description of flow physics that implies inaccurate values. Mesh quality is never expressed by one criterion, it is always assessed through different geometrical parameters whose values are found in precisely defined ranges for good quality grid. However, the range of values of particular quality criterion originates from different standards and is valid only for certain codes, hence it should not be considered as a general rule. The following quantities can be regarded as the most important quality criteria :

- **equiangle skewness** → cell shape deviation from a corresponding equiangle one :

$$max\left[\frac{\vartheta_{max}-\vartheta_e}{180°-\vartheta_e},\frac{\vartheta_e-\vartheta_{min}}{\vartheta_e}\right]$$

with ϑ_{max} and ϑ_{min} being the greatest and lowest angle of a cell, respectively, where ϑ_e is the angle of a corresponding equiangular face or cell (e.g. 60° for triangle and 90° for square) ; equiangle skewness takes values between 0 and 1, while good quality mesh should have value lower than 0.85 for triangular, quadrilateral and hexahedral cells and 0.9 for tetrahedral cells

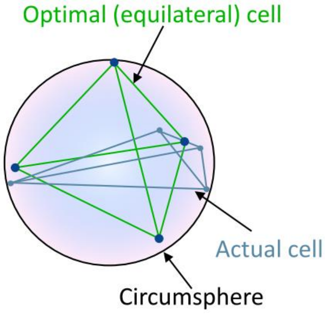

Figure 5.10 : Graphical explanation of equiangle skewness for tetrahedral cell

- **orthogonal quality** → misalignment between vectors that link the centers of two adjacent cells and the normal to the shared face :

$$min\left[\frac{\mathrm{A}_i\cdot\mathrm{f}_i}{|\mathrm{A}_i|\cdot|\mathrm{f}_i|},\frac{\mathrm{A}_i\cdot\mathrm{c}_i}{|\mathrm{A}_i|\cdot|\mathrm{c}_i|}\right]$$

computed for each face i where A_i is the face normal vector, f_i is vector that links the centroid of the i – th cell to the center of that face and c_i is vector from the centroid of the cell to the centroid of the adjacent cell ; values are ranged between 0 and 1 (worst and best condition, respectively) and should be greater than 0.01 to avoid calculation problems.

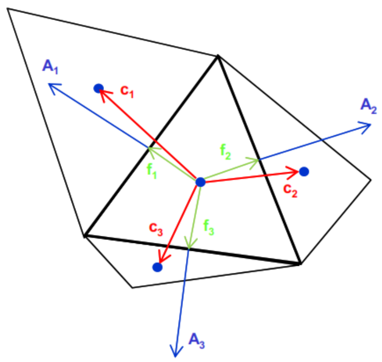

Figure 5.11 : Graphical explanation of orthogonal quality

- **aspect ratio** → definition for triangular / tetrahedral cell is the ratio between radii of circles / / spheres that circumscribe (R) and inscribe (r) the cell, divided by factor of 2 for triangular and factor of 3 for tetrahedral elements ; aspect ratio of quadrilateral / hexahedral cell is the ratio between maximum and minimum average length of cell edges in a specific coordinate direction local to the cell ; the best cells take value of 1 for aspect ratio, while values above 10 are indicative for poor quality elements.

Table 5.2 gives a summary of mesh quality parameters or metrics. Average equiangle skewness is very low, while maximum skewness is slightly lower than 0.9 limit, however, very low standard deviation suggests that only a handful of cells feature skewness values far from average. Average orthogonal quality is 1, which is highly desirable and minimum value is constant for each mesh and greater than 0.01 limit.

Metric		AR = 0.16	AR = 0.215	AR = 0.27	AR = 0.32	AR = 0.38	AR = 0.48
Equiangle Skewness	Maximum	0.89522	0.89703	0.89523	0.89703	0.89703	0.89704
	Minimum	5.97E-06	1.16E-05	1.27E-05	5.96E-06	5.74E-06	5.70E-06
	Average	9.72E-02	9.51E-02	9.47E-02	9.32E-02	9.39E-02	9.28E-02
	Standard deviation	0.1066	0.10295	0.1022	0.1007	0.1033	0.1023
Orthogonal Quality	Maximum	1	1	1	1	1	1
	Minimum	4.73E-02	4.73E-02	4.73E-02	4.73E-02	4.73E-02	4.73E-02
	Average	0.9519	0.9514	0.9519	0.9532	0.952	0.9529
	Standard deviation	8.71E-02	8.80E-02	8.64E-02	8.63E-02	8.85E-02	8.78E-02

Table 5.2 : Mesh quality metrics

As far as maximum cell aspect ratio is considered, the grids take values around 450 that is a value much greater than recommended. However, due to very high number of cells and tendency for precise meshing of boundary layer portion of the grid, such values do not pose a significant concern.

5.3 Simulation settings

CFD simulation of controlled airflow is performed on ANSYS Fluent 2020 R2 software that is included in standard ANSYS 2020 R2 package. The setup procedure consists of nine steps :

1) solver type → the flow experienced by root sections of wind turbine blade is essentially incompressible, supported by experimental findings of case 038 – velocities at different angles of attack imply average Mach number of 0.135 that falls within incompressible domain of subsonic flow ; therefore, preferred solver type is pressure – based transient

2) turbulence model → as already explained in section 4.2, turbulence models of choice are Transition SST and $k - \omega$ SST, with SDES option is turned on in both cases ; all other options are left as default

3) material properties → fluid material is left as air and dynamic viscosity coefficient is calculated for each angle of attack as $\mu = \rho v_\infty c/Re$; since expression derives from the definition of Reynolds number, we maintain the same experimental and numerical values and ensure dynamic similarity between experiment and numerical simulation

4) operating and boundary conditions → as the wind tunnel is operating at atmospheric conditions, operating pressure of 101325 Pa and operating temperature of 288.15 K are unchanged, although the latter is of little relevance as incompressible isothermal flow is assumed ; four types of boundary conditions are specified :

   - velocity inlet → uniform velocity profile is given by specifying velocity components for each AoA ($v_x = v_\infty \cos\alpha$ and $v_y = v_\infty \sin\alpha$) ; the wind tunnel that was used has a turbulence intensity always below 0.1%, therefore, a value of 0.07% is chosen ; on the other hand, turbulent length scale is estimated as 0.06% as for airfoil simulations it is suggested to choose 10% of airfoil chord; in cases where Transition SST model is turned on, intermittency value must also be inserted, however as the domain inlet corresponds to free – stream, a value of 1 remains (freestream also features turbulence kinetic energy and specific dissipation rate and needs to be fully represented by $k - \omega$ SST, to which Transition SST model reduces when $\gamma = 1$)

   - pressure outlet → gauge pressure is left as zero, while backflow turbulent intermittency, intensity and length scale assume the same values as velocity inlet for the same reasons

   - wall → refers to airfoil and VG surfaces ; the type is left as stationary and 'no – – slip' condition is imposed

   - periodic → refers to lateral sides of computational domain ; this is done in line with practical advice to have no constraints imposed on resolved turbulence

5) solution algorithm and discretization schemes → among several solution algorithms available within pressure – based solver, SIMPLEC is the standard choice for external aerodynamics problems ; employed discretization schemes are listed below (second order upwind scheme for momentum equation for the initial steady simulation) :

Variable	**Discretization scheme**
Gradient	Least Squares Cell Based
Pressure	Second Order
Momentum	Bounded Central Differencing
Turbulent kinetic energy	Second Order Upwind
Specific dissipation rate	Second Order Upwind
Turbulent intermittency	Second Order Upwind
Momentum – thickness Reynolds number	Second Order Upwind
Transient Formulation	Bounded Second Order Implicit

Table 5.3 : Spatial discretization schemes used for transient simulations

6) under – relaxation factors (URFs) → value assigned to pressure and momentum is 0.85, while 0.9 is inserted for turbulent kinetic energy, specific dissipation rate, turbulent intermittency and momentum – thickness Reynolds number ; the rest of available quantities (density, body force and turbulent viscosity) are left with default value of 1

7) residuals and monitors → it is important to set residuals convergence criterion to none; apart from physical quantities of interest (lift and drag forces), monitor of area – weighted average of velocity magnitude is also included, as this enables better insight on reaching stable flow sooner

8) initialization → full multigrid (FMG) initialization is used as it is useful for complex flowfields involving large pressure and velocity gradients on large meshes ; it solves the flow problem on a sequence of coarser meshes before transferring the solution onto actual mesh

9) run calculation → firstly, time step size is set as $\Delta t = 0.0001$ s implying Courant number of 0.007, a value smaller than value encountered with clean thick airfoil due to refined cells around very small vortex generators ; secondly, number of iterations per time step is set to 25 as previous simulations were optimized for that number of outer iterations; each transient simulation is initialized with a steady RANS simulation.

Chapter 6 - Validation stage

6.1 Discussion on the choice of turbulence model

Aerodynamic performance of any aerodynamic surface (e.g. blade or wing) is greatly influenced by the roughness state of the surface. Imperfections such as cracks, rifts, corrosion effects or any other form of micro – cavities and surface deterioration give rise to instability of the passing fluid and cause early transition from laminar to turbulent boundary layer flow. Such conditions are typical operating conditions to which blade surface undergoes after certain period of exploitation, therefore many numerical simulations are performed in this regime – fully turbulent or tripped conditions. However, certain attention is also payed to smooth surface conditions, which correspond to flow regime where boundary layer spontaneously transforms into turbulent state without any external factors – condition of free or natural transition. In this case skin friction is lower and flow separates at later stage, hence pressure drag is also smaller. Airfoil critical angle and corresponding lift coefficient (C_{Lmax}) are higher, while lift drop and drag rise in stall region are less drastic than in fully turbulent regime. Free transition was the adopted regime for experimental testing of cropped – delta VG configuration on DU97 – W – 300 airfoil, whose lift and drag values serve as validation benchmark of present CFD simulation.

Free transition regime for DU97 – W – 300 airfoil with delta VGs was simulated in the work of Mosca [30], who adopted Transition SST turbulence model and obtained sufficiently accurate values of aerodynamic coefficients at angles predominantly in linear region of lift curve (C – H computational grid and AR = 0.027). However, the model failed to capture correct stall behavior (figure 6.1).

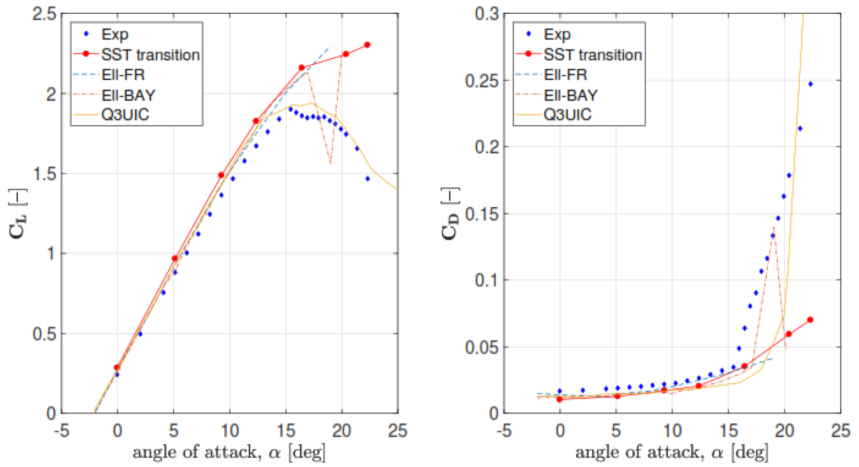

Figure 6.1 : Lift and drag polars for airfoil equipped with VGs at 20% c for conditions of free transition, an extract from [30]

On the other hand, Passoni [31] demonstrated that airfoil perfomance at all angles of attack can be accurately captured with $k-\omega$ SST turbulence model within SDES model (member of Scale – Resolving Simulation method). Thus, it is possible to employ SDES together with both Transition SST and $k-\omega$ SST models for simulations at different angles of attack. Since flow transition is more evident at lower angles of attack, $k-\omega$ SST model might be considered as appropriate choice for simulating controlled airflow at near – critical angles of attack.

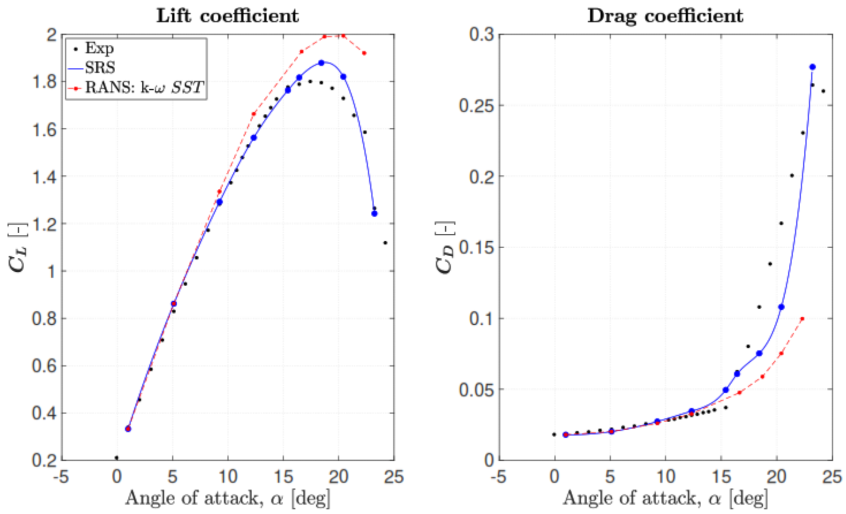

Figure 6.2 : Lift and drag polars for 30 % thick airfoil equipped with VGs at 20 % c in fully turbulent regime, an extract from [31]

In order to support the latter statement, a comparative analysis is performed at three angles of attack (table 6.1). The comparison shows slight improvement in accuracy at critical angle $\alpha = 18.513^{o}$ and $\alpha = 19.512^{o}$ for lift and drag coefficients. Obviously, flow transition at these angles becomes irrelevant and knowing that $k-\omega$ SST model deals with two additional equations instead of four (Transition SST), it may be concluded that SDES - $k-\omega$ SST model is the turbulence model of choice at critical and post – critical angles of attack. On the other hand, values of lift and drag coefficient at $\alpha = 17.493^{o}$ are clearly in favor of SDES – Transition SST model, which is the chosen turbulence model at angles lower than critical angle of attack.

			SDES - Transition SST				SDES - k-ω SST			
			AR = 0.16							
α [°]	C_{Lexp}	C_{Dexp}	C_L	C_D	δC_L[%]	δC_D[%]	C_L	C_D	δC_L[%]	δC_D[%]
17.493	2.0478	0.0405	**2.1195**	**0.0537**	**3.50**	**32.58**	1.8878	0.0622	-7.82	53.51
18.513	2.0753	0.0509	2.2056	0.06	6.28	17.87	**2.1713**	**0.0571**	**4.63**	**12.26**
19.512	2.0379	0.087	2.3035	0.0615	13.03	-29.31	**2.2028**	**0.0615**	**8.09**	**-29.31**

Table 6.1 : Comparison of results for different turbulence models

6.2 Span sensitivity analysis

The results of lift and drag coefficients may be subject of higher errors that do not depend on the choice of turbulence model, but the errors originate from too narrow geometry that suppresses correct formation of turbulence structures that occur at certain angles of attack. The recommended aspect ratio serving as base model for present CFD simulation is 0.16 (3 VG pairs). While this aspect ratio performs well for angles below critical angle of attack, it may not be valid at very high angles indicative of stall onset. This is the case for angles 19.512°, 20.467° and 21.443°, hence span sensitivity analysis has to be performed.

For angle 19.512° two aspect ratios were simulated, the base grid of AR = 0.16 and a grid of AR = 0.215. In case of lift coefficient, small improvement of 1% is present, whereas drag coefficient is notably improved, since relative error drops by roughly 20%.

			SDES - k-ω SST			
			AR = 0.16		AR = 0.215	
α [°]	C_{Lexp}	C_{Dexp}	δC_L[%]	δC_D[%]	δC_L[%]	δC_D[%]
19.512	2.0379	0.087	8.09	-29.31	**7.00**	**-8.42**

Table 6.2 : Comparison of relative errors at $\alpha = 19.512^\circ$ for different grid aspect ratios

Span sensitivity analysis was the most time consuming for angles 20.467° and 21.443° where four aspect ratios were investigated. Results of lift and drag coefficients eventually come to acceptable values at aspect ratio 0.48 (9 VG pairs) for $\alpha = 20.467^\circ$, although only slight improvement exists between results from AR = 0.38 and AR = 0.48. Unfortunately, sensitivity analysis for $\alpha = 21.443^\circ$ did not deliver lift and drag values that can be regarded as sufficiently accurate. Relative lift error never drops below 15 %, whereas drag error persists below – 45 %, even with grid with nine pairs of vortex generators. However, both relative lift coefficient error and relative drag coefficient error follow a decreasing trend for different grid aspect ratios.

			SDES - k-ω SST							
			AR = 0.16		AR = 0.27		AR = 0.38		AR = 0.48	
α [°]	C_{Lexp}	C_{Dexp}	δC_L[%]	δC_D[%]	δC_L[%]	δC_D[%]	δC_L[%]	δC_D[%]	δC_L[%]	δC_D[%]
20.467	1.9307	0.1327	17.77	-39.42	15.98	-37.69	12.16	-36.95	**12.02**	**-33.66**

Table 6.3 : Comparison of relative errors at $\alpha = 20.467^\circ$ for different grid aspect ratios

			SDES - k-ω SST							
			AR = 0.16		AR = 0.32		AR = 0.38		AR = 0.48	
α [°]	C_{Lexp}	C_{Dexp}	δC_L[%]	δC_D[%]	δC_L[%]	δC_D[%]	δC_L[%]	δC_D[%]	δC_L[%]	δC_D[%]
21.443	1.8392	0.1776	22.87	-55.47	21.95	-52.28	22.43	-48.19	20.82	-46.98

Table 6.4 : Comparison of relative errors at $\alpha = 21.443^{\circ}$ for different grid aspect ratios

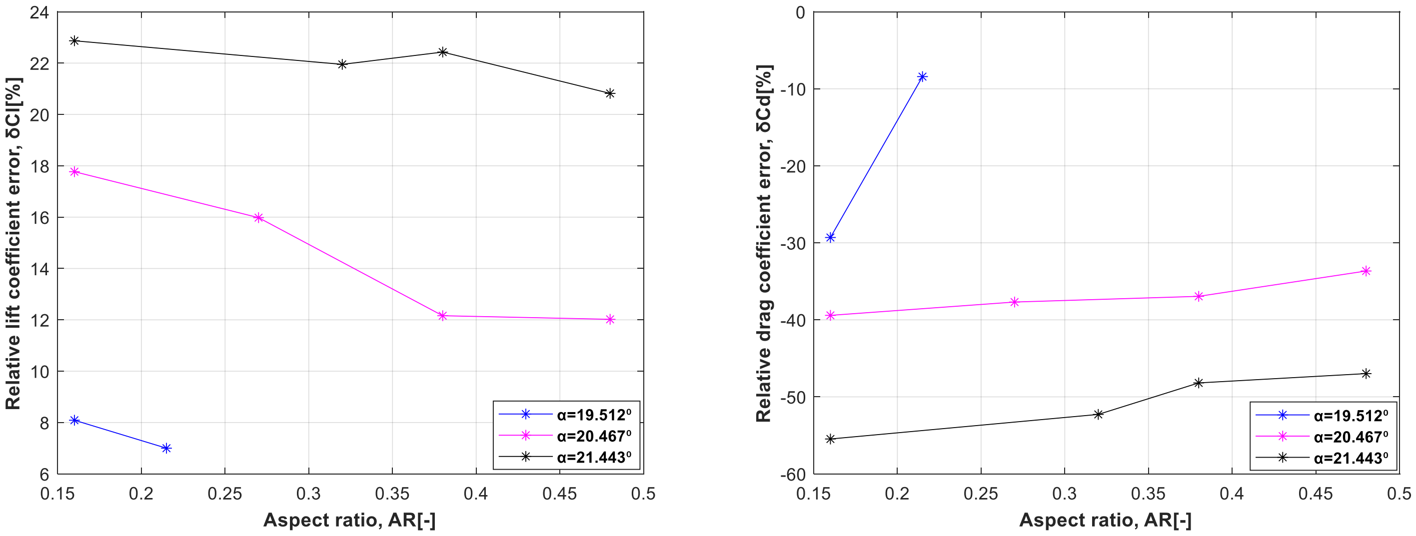

Figure 6.3 : Variation of relative error with grid aspect ratio for lift and drag coefficient

Graphs in figure 6.3 show consistent trends in relative error variation with different aspect ratios. In all three cases, relative errors decrease with increasing grid aspect ratio. Influence of AR is more emphasized with lift coefficient values, while the most prominent change in drag coefficient occurs for $\alpha = 19.512^{\circ}$. Probable cause for such behavior is the fact that both angles 20.467° and 21.443° fall within mild – stall region, an earlier segment of stall onset, therefore different flow conditions prevail than those at lower angles of attack. Despite not achieving desired accuracy at every angle of attack, the obtained results give certain insight for the expected error behaviors, which may serve as one of starting points for some future analysis deep – stall angles of attack with present airfoil and vortex generator configuration.

6.3 Resulting graphs of lift and drag coefficients

Span sensitivity analysis was the last step before composing the resulting lift and drag curves. Investigation of the effect of aspect ratio on lift and drag coefficients is not necessary for angles of attack below 19^0, where the recommended grid of $AR = 0.16$ proved to be sufficient. As the main focus of the thesis is on airfoil behavior at higher angles of attack, angles below 6^0 were not taken into consideration. Low angles of attack feature relatively low values of lift and drag coefficients, therefore, it is often highly ambitious to achieve the desired accuracy, especially in case of thick airfoil with blunt trailing edge. More appropriate choice for lower angles is found with other turbulence method (RANS method instead of SRS) and other type of computational grid, demonstrated by Mosca [30]. Table 6.5 lists all lift and drag coefficient values from current CFD simulation and figure 6.4 gives resulting lift and drag curves alongside the experimental ones.

α [°]	C_{Lexp}	C_{Dexp}	C_L	C_D	δC_L[%]	δC_D[%]	AR	Turbulence model
6.167	0.982	0.0198	1.0623	0.0217	8.18	9.62	0.16	SDES - Transition SST
11.317	1.5573	0.0245	1.5739	0.0327	1.07	33.64	0.16	SDES - Transition SST
14.409	1.8343	0.0326	1.849	0.0415	0.80	27.19	0.16	SDES - Transition SST
15.954	1.9551	0.0368	2.0034	0.0478	2.47	29.98	0.16	SDES - Transition SST
17.493	2.0478	0.0405	2.1195	0.0531	3.50	31.18	0.16	SDES - Transition SST
18.513	2.0753	0.0509	2.1713	0.0571	4.63	12.26	0.16	SDES - k-ω SST
19.512	2.0379	0.087	2.1805	0.0797	7.00	-8.42	0.27	SDES - k-ω SST
20.467	1.9307	0.1327	2.1627	0.0880	12.02	-33.66	0.48	SDES - k-ω SST

Table 6.5 : Resulting values of lift and drag coefficients

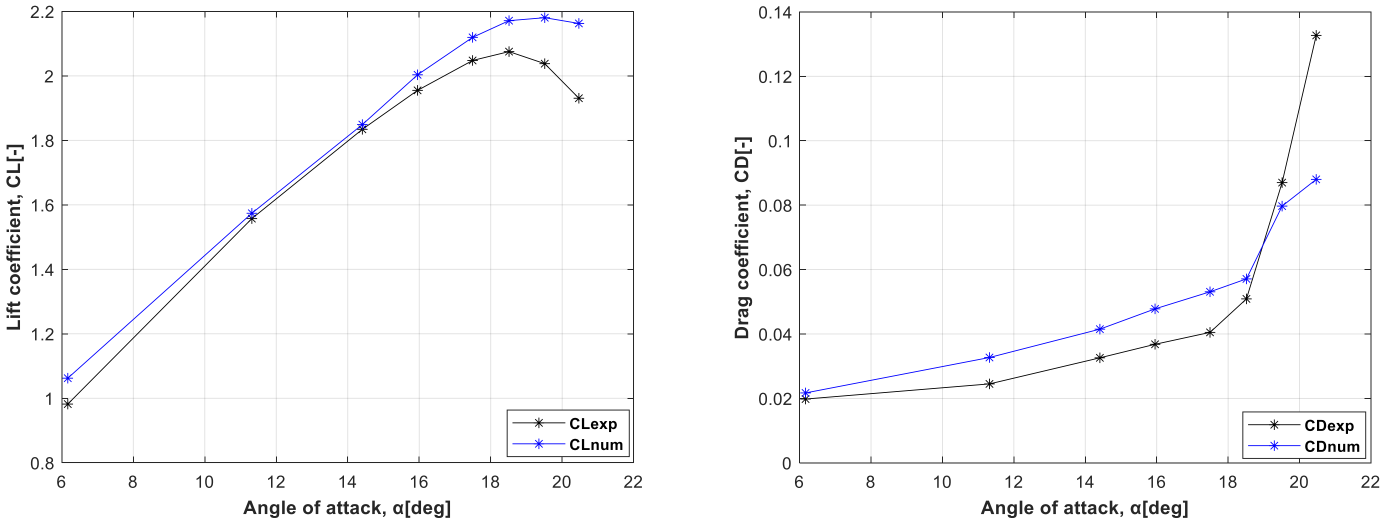

Figure 6.4 : Resulting graphs of lift and drag coefficients

The obtained values show that lift curve is decently simulated, the majority of the range exhibits relative error below 5 %, while post – critical angles are still reasonably well predicted with maximum error of 12 % at 20.467° (knowing the angle corresponds to stall region). At $\alpha = 6.167^{o}$ slightly higher lift error is encountered, however, this angle corresponds to lower portion of the lift curve where implementation of scale – resolving approach is questionable and low values are encountered, difficult for accurate estimation. Situation is different with drag coefficient. The results follow experimental drag curve for the most part, but relative errors are distinctly higher than those of lift coefficient. However, this doesn't mean serious problem immediately.

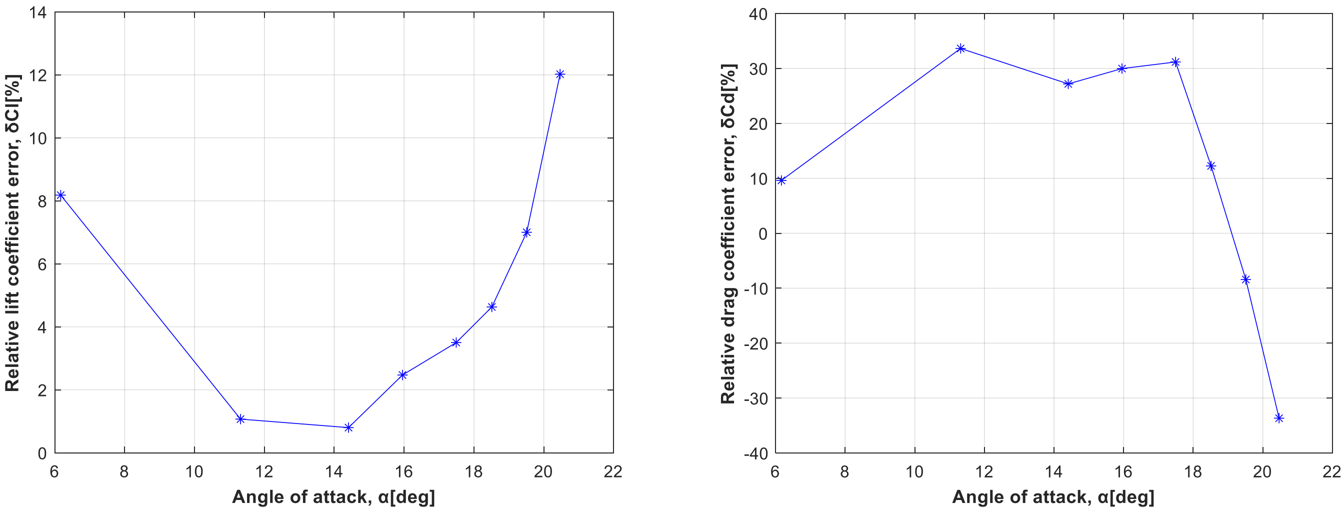

Figure 6.5 : Variation of relative error with angle of attack for lift and drag coefficient

Recent study of wind turbine airfoil with CtR – CU delta VG configuration [31] had to deal with the same problem. Several numerical results of drag coefficient exhibit similar errors, even though lift coefficient had been nicely captured (table 6.6). The author demonstrated that simulated pressure coefficient follows the experimental distribution with high accuracy (figure 6.6). It had been concluded that scale – resolving methods in conjunction with RANS models experience difficulties when simulating viscous effects. Thus, an incorrect skin friction is not unusual and overall drag gets miscalculated.

Unfortunately, experimental findings of pressure coefficient could not be found for the same airfoil with cropped – delta VG configuration and comparison between simulated and experimental pressure distribution on pressure and suction sides wasn't possible in present work. Nevertheless, important conclusions can be drawn from similar research and still be valid.

Controlled profile, VG20%c, SDES, AR=0.16						
α [°]	Method	AR	C_L [-]	C_D [-]	δC_L [%]	δC_D [%]
9.238	SDES	0.16	1.2919	0.0273	0.76%	1.87%
12.239	SDES	0.16	1.5629	0.0346	-0.27%	9.15%
15.409	SDES	0.16	1.7633	0.0496	-0.76%	33.33%
16.429	SDES	0.16	1.8171	0.0608	1.58%	-2.72%
18.426	SDES	0.16	1.8791	0.0753	4.66%	-30.28%
20.413	SDES	0.16	1.8207	0.1080	5.30%	-35.29%
23.225	SDES	0.49	1.2425	0.2769	-1.76%	4.81%

Table 6.6 : Lift and drag coefficients for 30 % thick airfoil with CtR – CU delta VGs, an extract from [31]

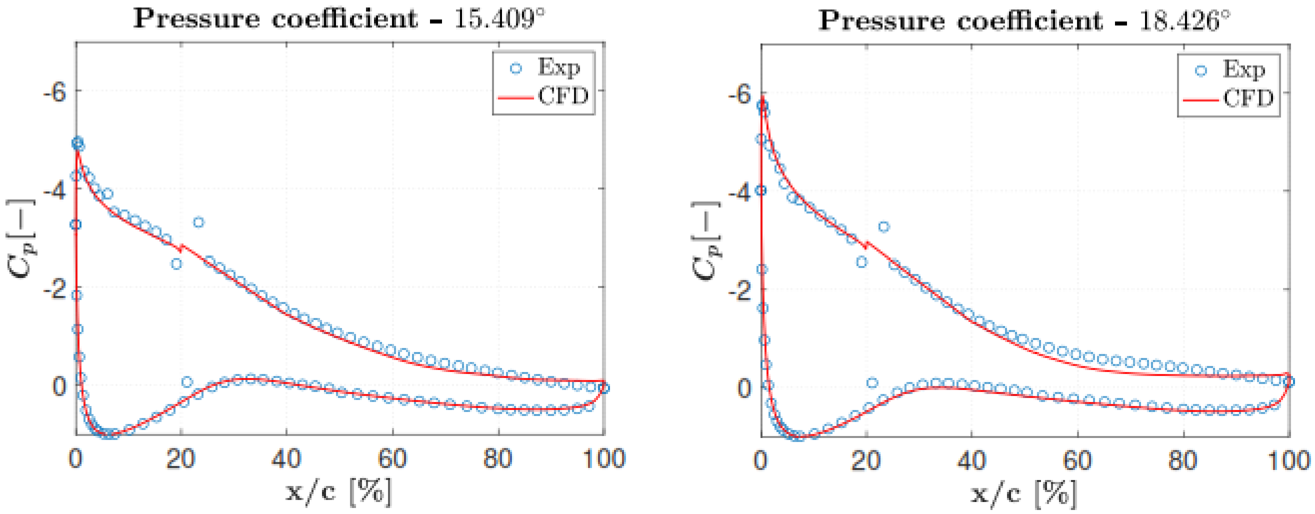

Figure 6.6 : Pressure coefficient distribution at different angles of attack for 30 % thick airfoil with CtR – CU delta VGs, an extract from [31]

Scale – Resolving Simulation emboddied in SDES – Transition SST/$k - \omega$ SST with ‘O’ – type grid proved to be an effective solution technique for flow around DU 97 – W – 300 airfoil equipped with cropped – delta vortex generators. The approach is most suitable at high, near – critical angles of attack (as well as critical), whereas simulations at angles in mild – and deep – stall regions can still make use of SRS method, although span sensitivity analyses to certain extent need to be carried out.

Chapter 7 - Inspection of simulated flow

7.1 Velocity and pressure fields

After pre – processing and solver execution, CFD simulation reaches post – processing stage, where investigation of relevant flow structures and flowfield in general, takes place. Post – processing can be done in several ways, depending on the type of flow problem. For the present case of controlled airflow around wind turbine airfoil with vortex generators, inspection of velocity and pressure fields should give some basic description of the flow physics. More advanced analysis is performed by looking into pathlines originating from vortex generators as well as visualizing turbulent structures through Q – criterion.

Velocity and pressure fields are provided in figure 7.1 for three different angles of attack, colored with velocity magnitude in the range 0 – 130 m/s and static pressure in the range - 5000 – 1300 Pa, respectively. Suction side of airfoil is characterized by increasing or adverse pressure gradient in downstream direction, causing flow deceleration and subsequent separation (dark blue). Pressure side contains stagnation zone (low velocities and high pressure values) and visualizes decreasing or favorable pressure gradient that enables the fluid to accelerate, so no separation takes place. Regions of high velocity increase with angle of attack, as well as regions of flow recirculation. Rising values of velocity in the vicinity of leading edge correspond to decreasing values in static pressure, explaining the rise in lift force with increasing angle, however, greater blue regions (low pressure) also justify rise in pressure drag component.

For a closer look into extent of separated flow it is always helpful to inspect negative x – velocity distribution around the airfoil (figure 7.2). Recirculation zone is almost non – existent at $\alpha = 11.317^{o}$ and gradually develops into a visible separation region, most notably displayed at $\alpha = 20.467^{o}$ (mild stall). Although 30% thick airfoil is the case, the extent of separation in mild stall region is unusually small, which explains the huge practical advantage that vane vortex generators provide. The extent of stagnation zone increases with angle of attack as well, since stagnation point slightly moves downwards with higher angle and portion of the flow that travels towards suction side must travel longer distance before reaching trailing edge.

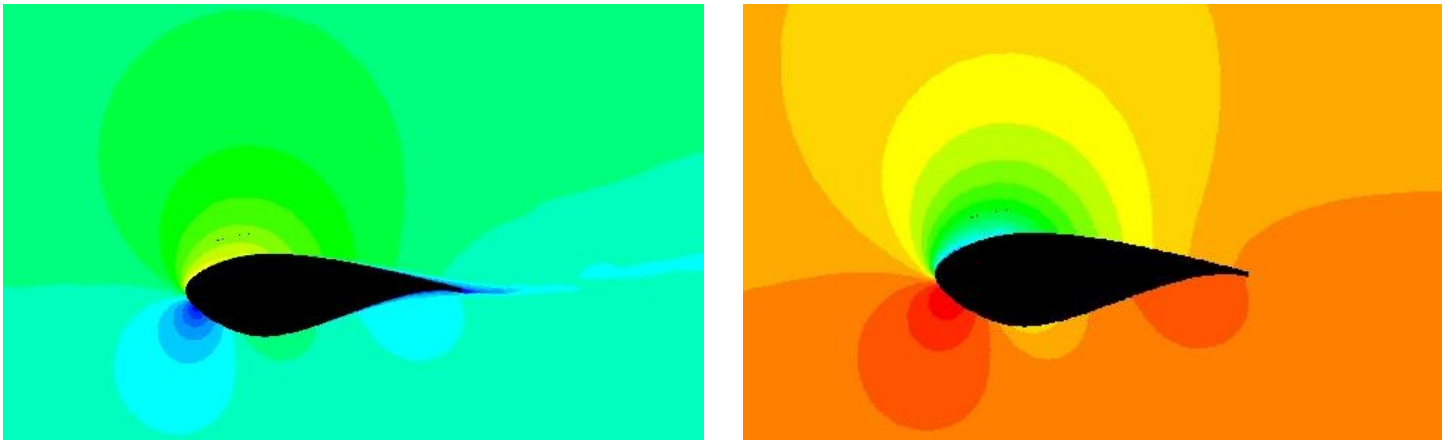

$\alpha = 11.317^0$

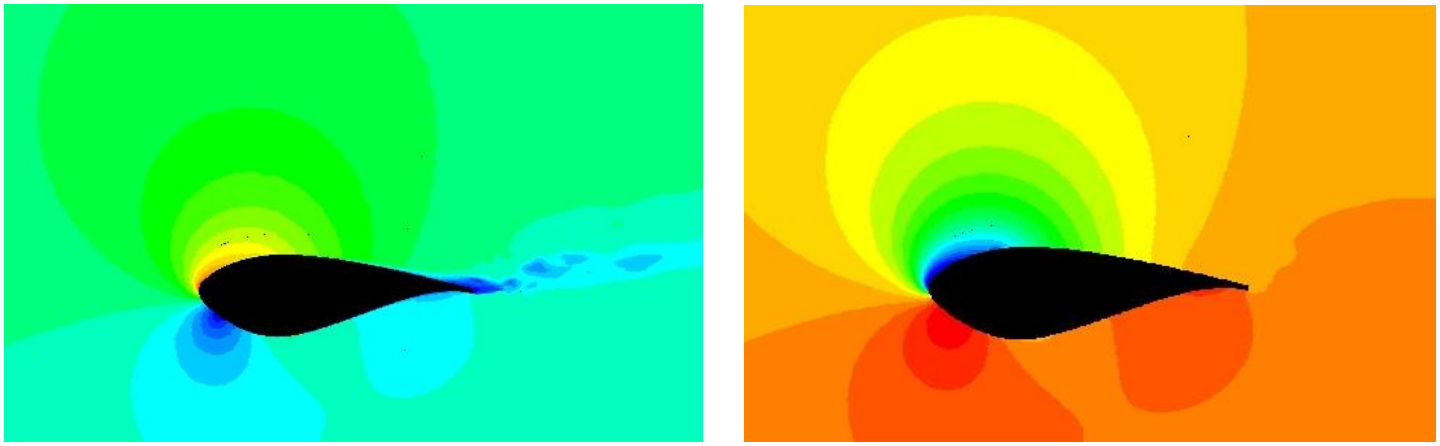

$\alpha = 15.954^0$

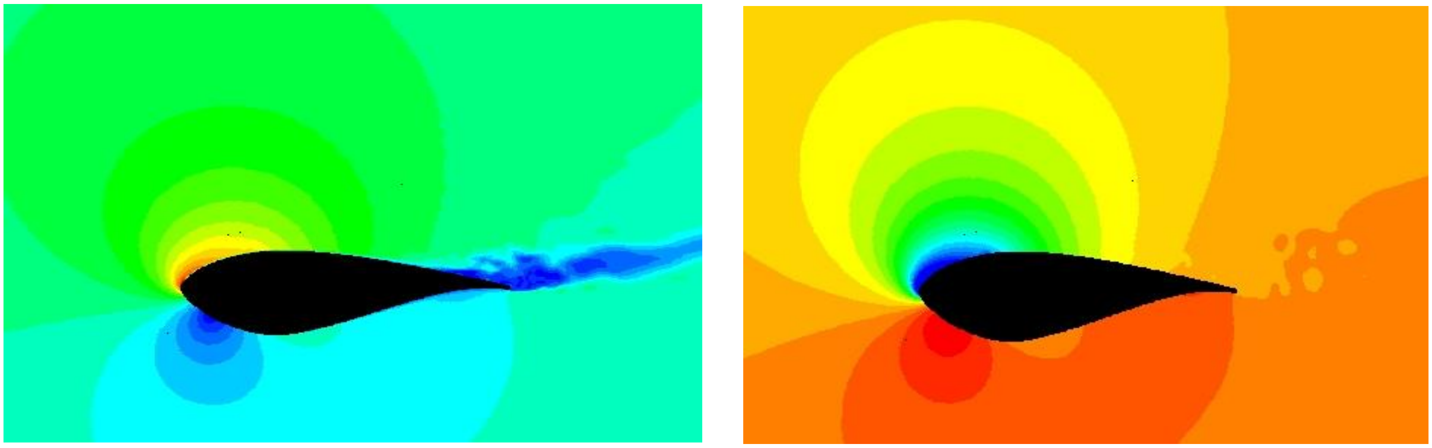

$\alpha = 20.467^0$

Figure 7.1 : Time – averaged velocity magnitude and static pressure fields at three different angles of attack

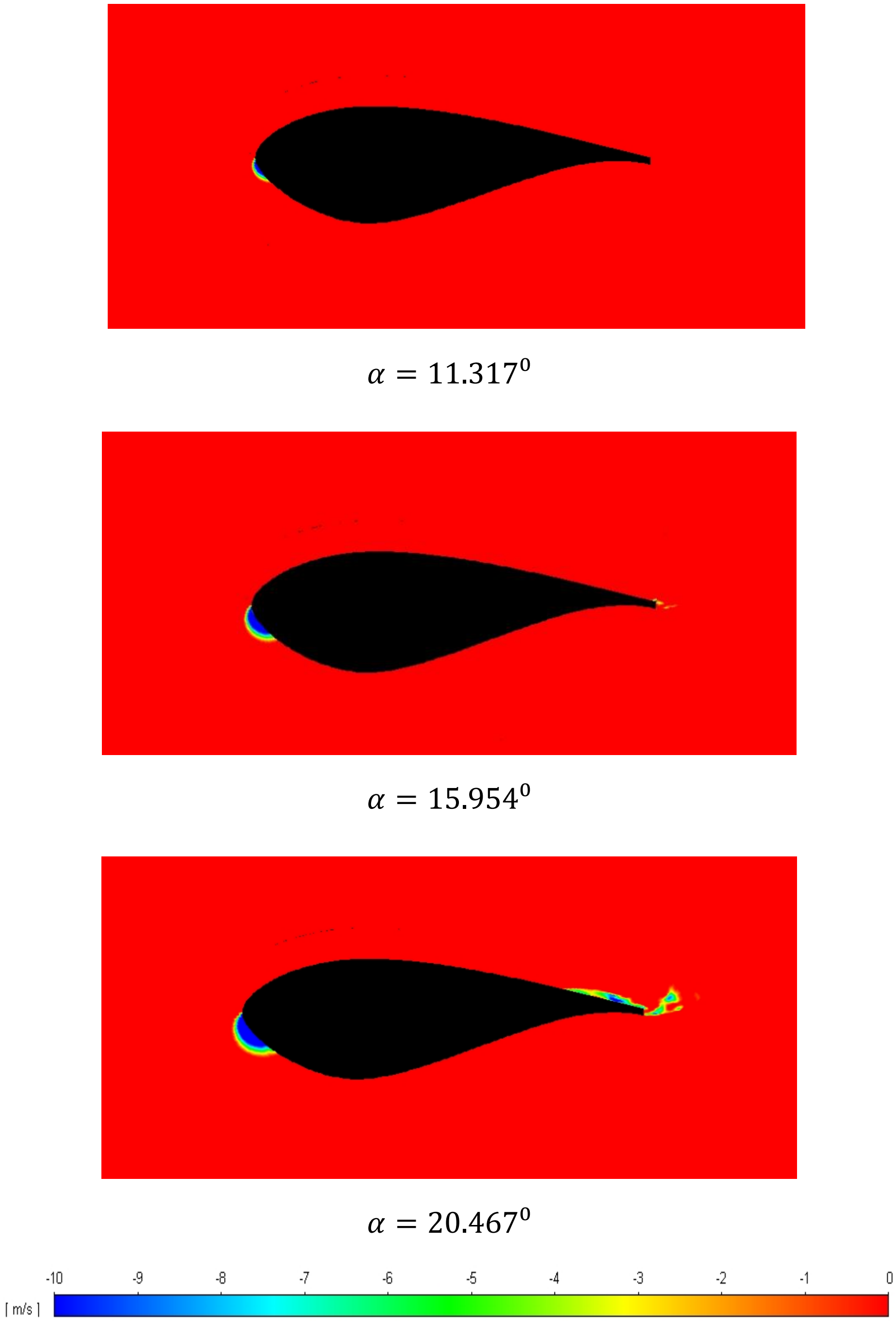

$\alpha = 11.317^0$

$\alpha = 15.954^0$

$\alpha = 20.467^0$

Figure 7.2 : Time – averaged negative x – velocity field at three different angles of attack

It is interesting to compare velocity and pressure fields around airfoils equipped with two vortex generator configurations, i.e. counter – rotating common – upwash (CtR – CU) delta VGs (graphs extracted from [31]) vs counter – rotating common – downwash (CtR – CD) cropped – delta VGs. Graphs are compared at $\alpha = 16^o$ (figure 7.3). It is evident that CtR – CD cropped – delta vortex generators are more effective in stall delay as flow recirculation zone drastically shrinks and separation line moves towards the trailing edge. This statement is even more evident when looking into negative x – velocity distributions around the airfoil (figure 7.4) for two different angles of attack. At 16^o recirculation zone is barely noticed for airfoil with cropped – delta VGs, whereas at 20^o recirculation zone is observed for both VG configurations, however the extent of separated flow is again distinctly in favor of cropped – delta vortex generators.

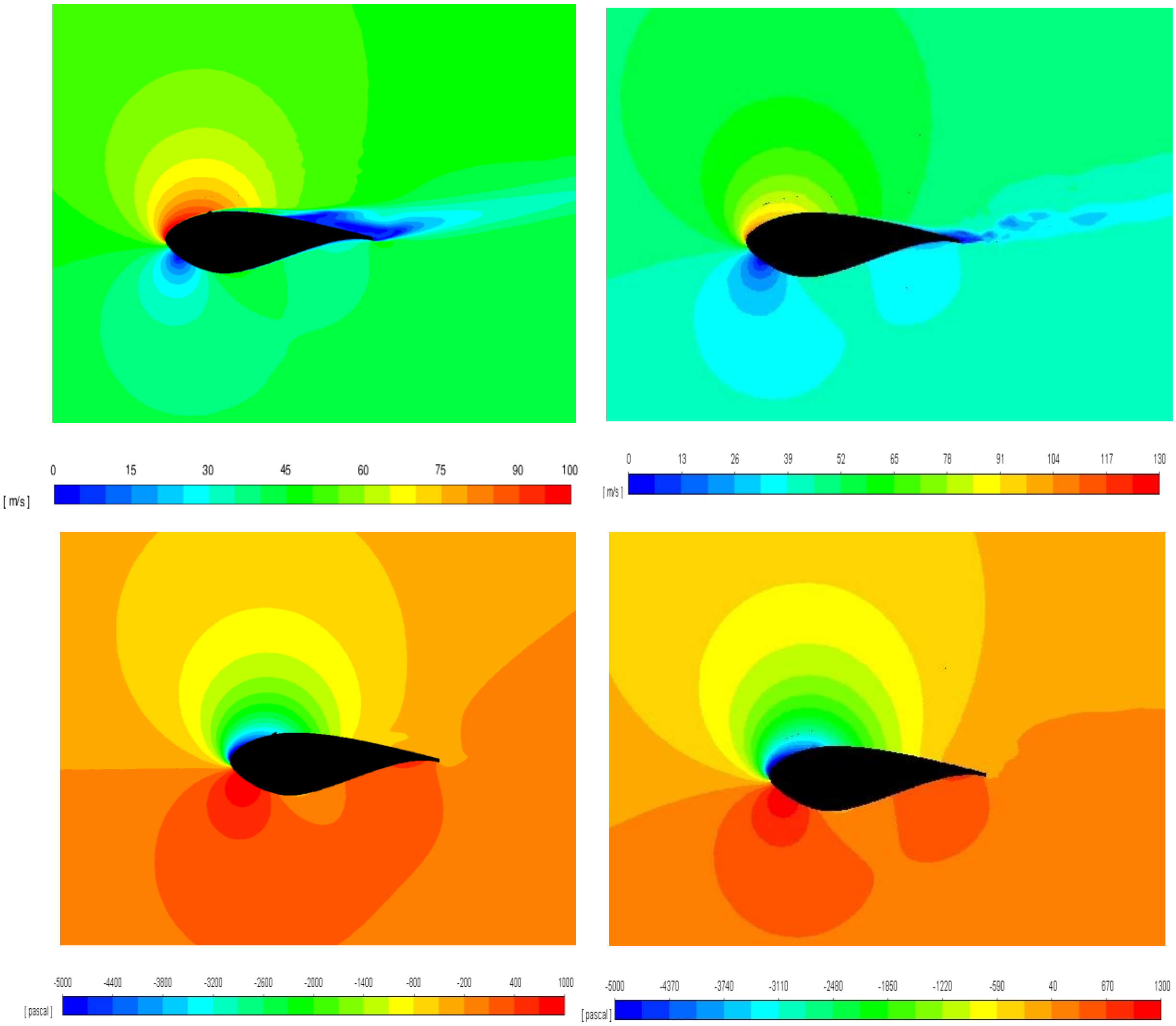

Figure 7.3 : Comparison of velocity and pressure fields between airfoils equipped with CtR – CU delta (left) and CtR – CD cropped – delta VGs (right) at $\alpha = 16^0$

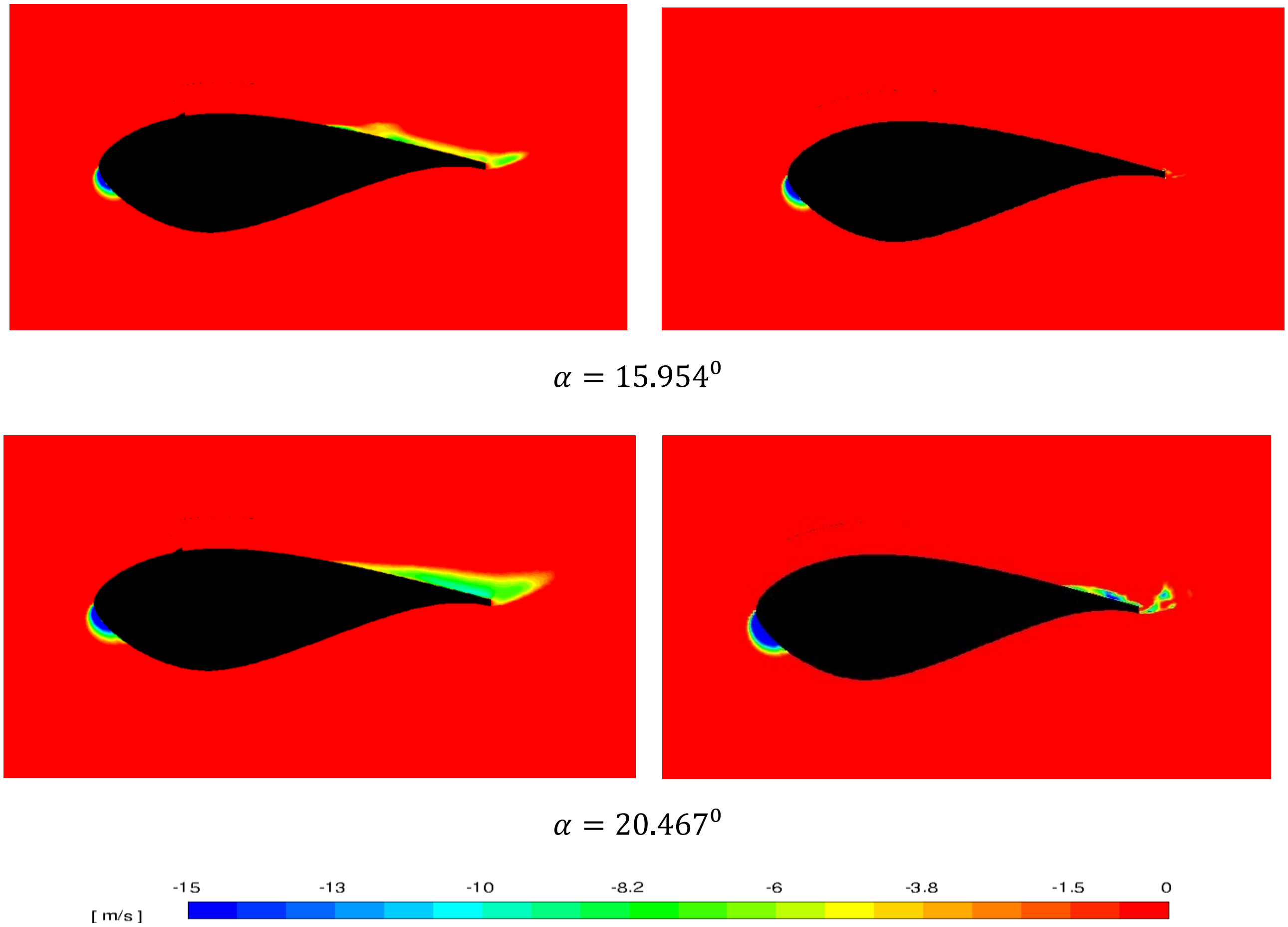

$\alpha = 15.954^0$

$\alpha = 20.467^0$

Figure 7.4 : Comparison of negative x – velocity fields between airfoils equipped with CtR – CU delta (left) and CtR – CD cropped – delta VGs (right) at two different angles of attack

7.2 Pathlines

Fluid kinematics makes use of three concepts for describing an unsteady flow :

- streamline → curve whose tangent at any point is in the direction of the velocity vector at that point ; mathematically, this means ($d\vec{s}$ – infinitesimal streamline vector):

$$d\vec{s} \times \vec{v} = \vec{0} \rightarrow \text{streamline equation}$$

- pathline or trajectory → represents the path that fluid particle takes through space as a function of time ; the equation of pathline of fluid particle P and associated initial condition are :

$$\frac{d\vec{x}_P(t)}{dt} = \vec{u}_P(\vec{x}_P(t), t)$$

$$\vec{x}_P(t_0) = \vec{x}_{P0}$$

- streakline → locus of fluid particles which earlier passed through a prescribed point
- timeline → curve formed by a set of fluid particles that were marked at previous time instant, thereby creating a line that is displaced in time as the particles move.

For a steady flow there is no difference between streamline, pathline and streakline, they are all the same curves in space. This can be very useful as often it is difficult to observe a particular field line, e.g. streamlines in an experiment, where streaklines are simpler to visualize and streamline pattern can be obtained. Such conclusion fails to hold for an unsteady flow. Moreover, in SRS calculations major portion of the flow and related turbulence are resolved (opposed to modeled structures below the grid scale), hence, pathlines exhibit valuable amount of flow information.

Three angles of attack can be considered in present study for inspection of pathlines originating from vortex generators. At angle 11.317^o pathlines extend almost along the entire length of the suction side. Eventually, flow detaches from the surface and pathlines in upward direction are detected. Situation is different for angle of attack 15.954^o where pathlines detach earlier than before and recirculation region is evident in the vicinity of trailing edge. Post – critical angle 20.467^o exhibits flow behavior in mild – – stall conditions, i.e. pathlines remain attached a certain distance along the suction side before setting free from airfoil surface at distance fairly close to flow control devices. This is accompanied by a significant recirculation zone over the rear part of airfoil surface.

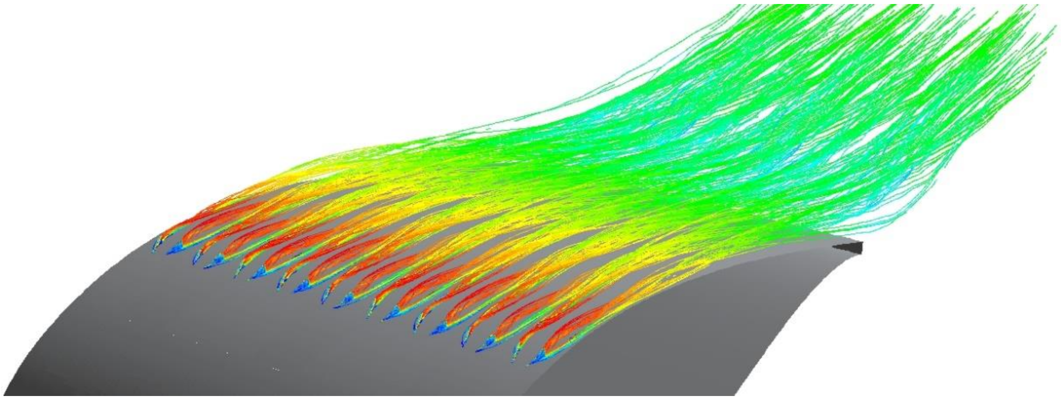

$\alpha = 11.317^o$

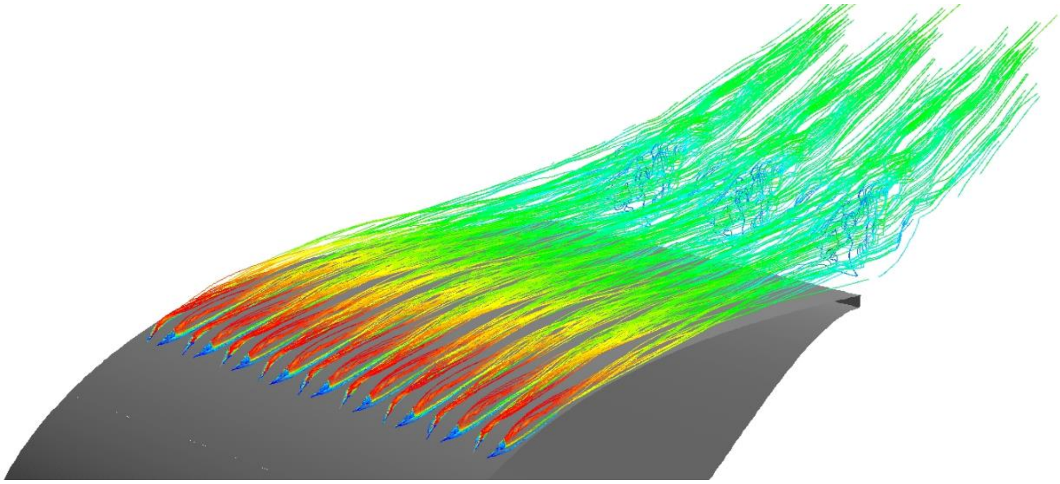

$\alpha = 15.954^o$

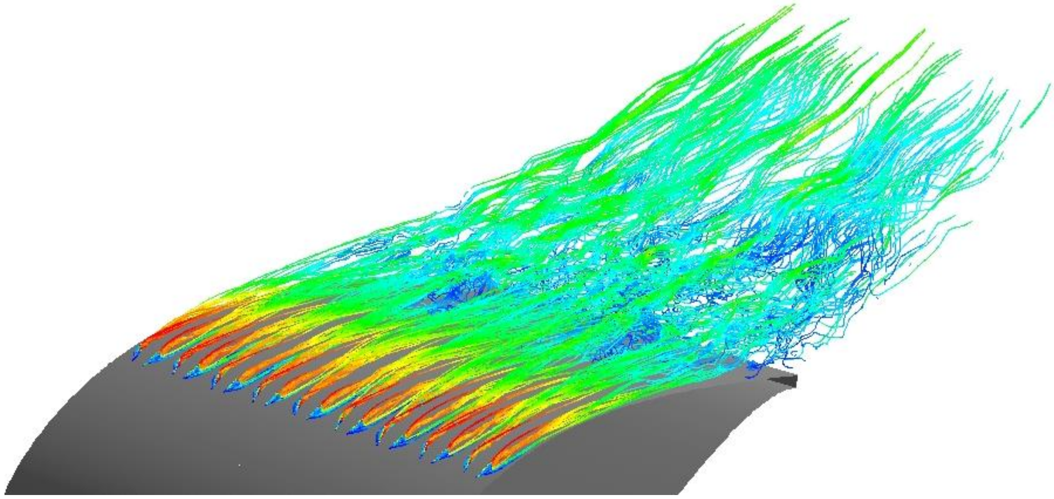

$\alpha = 20.467^o$

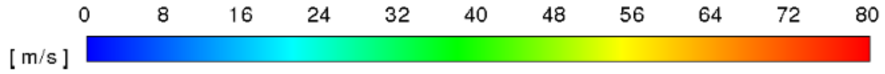

Figure 7.5 : Pathlines along airfoil suction side at three different angles of attack

It is interesting to comparise at angle of attack 20º the effectiveness of CtR – CU delta [31] and CtR – CD cropped – delta vortex generators (figure 7.6). Despite different boundary layer regimes, with fully turbulent in the first case and natural transition in the second, it seems that cropped – delta vortex generators in common – downwash orientation are more capable of reducing the influences of adverse pressure gradient and suppressing massive flow separation.

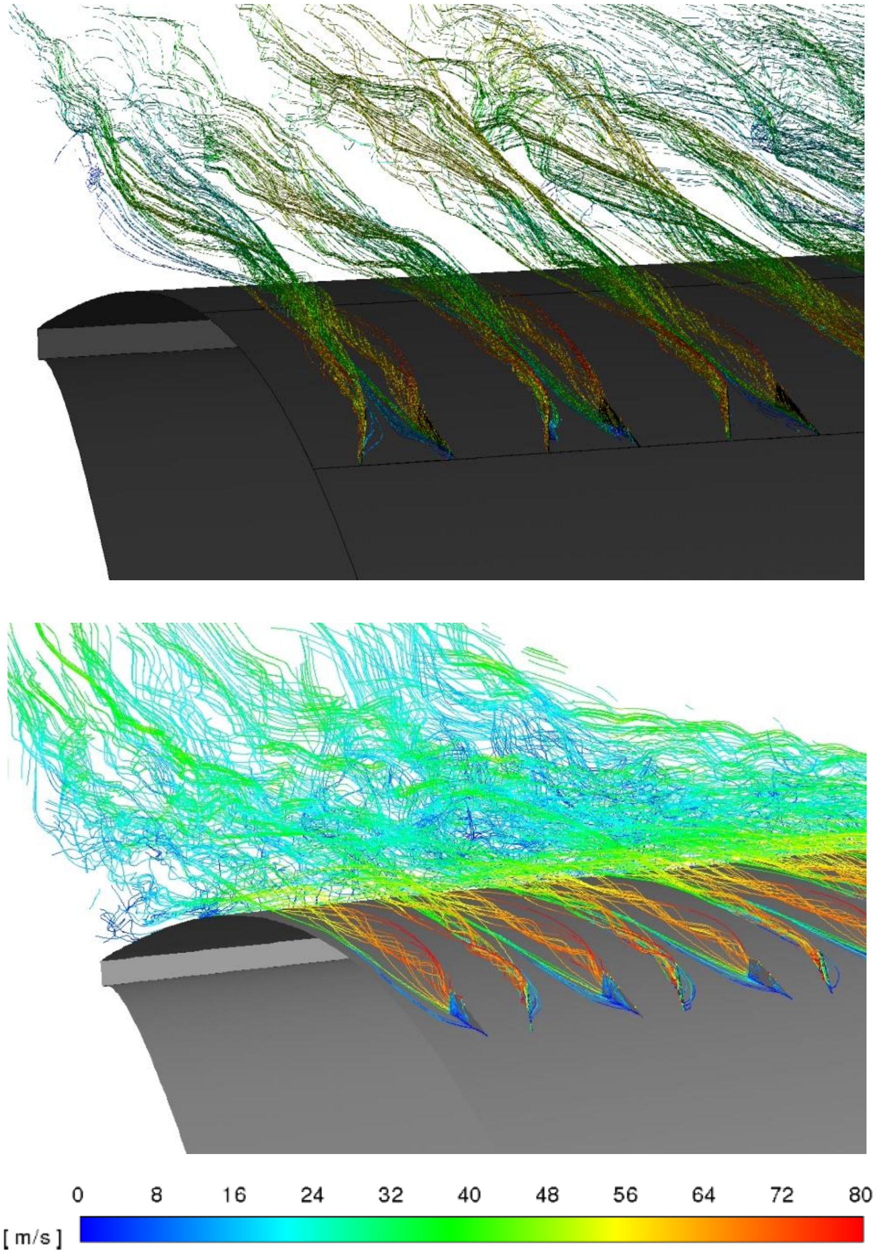

Figure 7.6 : Comparison of pathlines along airfoil suction side between CtR – CU delta VGs in fully turbulent [31] and CtR – CD cropped – delta VGs in free transition regime at $\alpha = 20$º

Subsequently, the view is zoomed to analyze pathlines around vane vortex generators themselves. Each vane of a VG pair shows its pressure and suction side. This is important as pressure side experiences higher pressure field, so fluid tends to ‘climb’ over the edge towards the vane suction side, hence vortical fluid motion is generated. Since both pairs are CtR oriented, the difference in behavior of fluid particles comes down to the influence of whether common – downwash or common – upwash is the relative direction of vortices. In common – upwash case both vanes produce vortices that are rotating in direction from the airfoil surface (upper picture), while common – downwash means resulting vortices are rotating in the same direction but downwards, i.e. towards the airfoil surface. Detrimental influence of common – upwash orientation is supplemented by delta shape, as the absence of tip chord serves as a ’launch’ mechanism for generated vortices that are set at higher trajectory in immediate vicinity of VG trailing edges.

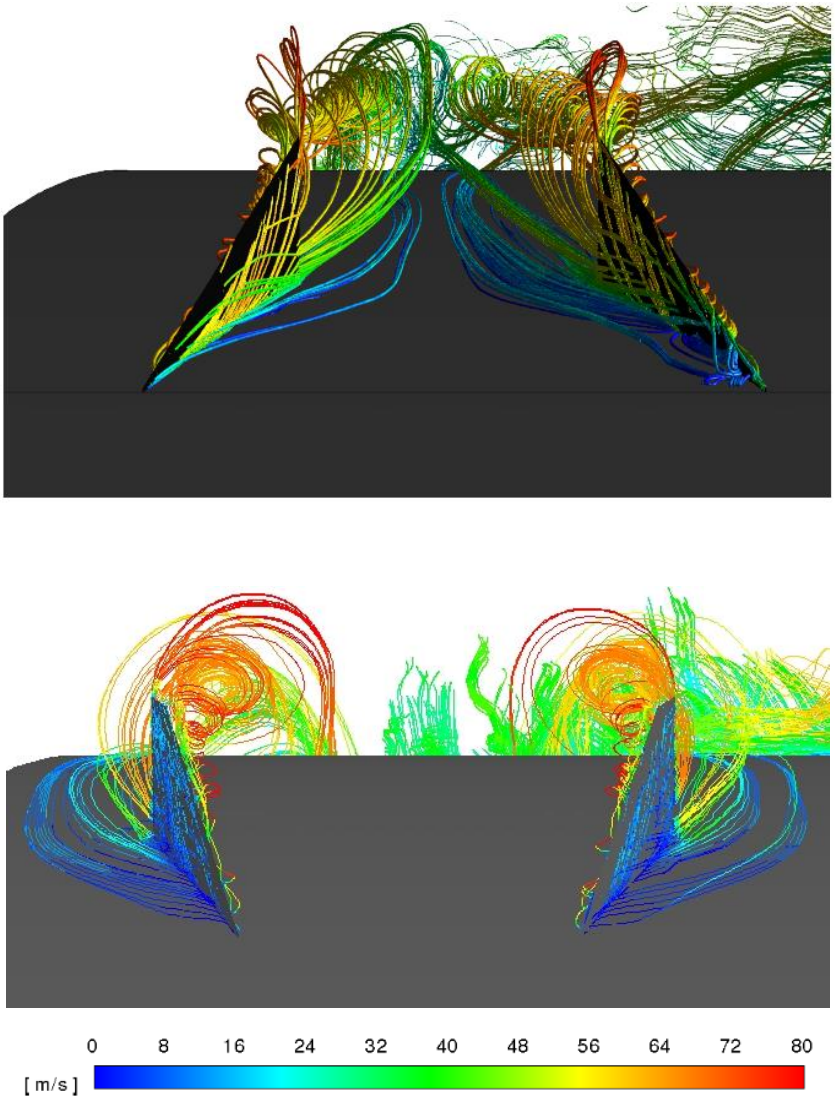

Figure 7.7 : Comparison of pathlines originating from common – upwash delta [31] and common – downwash cropped – delta vortex generators at $\alpha = 20^0$

7.3 Flow visualization by Q – criterion

As scale – resolving simulation was conducted, visualization of turbulence structures might even be considered as the most important step and is typically enabled by using an iso – surface of Q – criterion. Q – criterion is the first three – dimensional vortex criterion that defines a vortex as a spatial region where the Euclidean norm of the vorticity tensor dominates that of the rate of strain. Mathematically, this is expressed as :

$$\nabla\vec{v} = \bar{\bar{s}} + \bar{\bar{\omega}}$$

$$\bar{\bar{s}} = \frac{1}{2}[\nabla\vec{v} + (\nabla\vec{v})^T] \;\rightarrow\; \text{strain rate tensor}$$

$$\bar{\bar{\omega}} = \frac{1}{2}[\nabla\vec{v} - (\nabla\vec{v})^T] \;\rightarrow\; \text{vorticity tensor}$$

$$S = \sqrt{2\bar{\bar{s}}:\bar{\bar{s}}}\;\;[s^{-1}] \;\rightarrow\; \text{absolute value of strain rate}$$

$$\Omega = \sqrt{2\bar{\bar{\omega}}:\bar{\bar{\omega}}}\;\;[s^{-1}] \rightarrow \text{absolute value of vorticity}$$

$$Q = \frac{1}{2}(\Omega^2 - S^2) > 0$$

Typical values of Q range between $10^5 - 10^7$ for visualizing relevant turbulent structures. This value is necessary for the creation of corresponding iso – surface which is then colored by choosing one of several flow quantities, such as velocity magnitude, static pressure, turbulent or ‘eddy’ viscosity, turbulent viscosity ratio, etc. The most appropriate coloring in this case is performed with velocity magnitude, while the optimal iso – value of each iso – surface turns out to be 10^5. Figure 7.8 displays comparison of turbulent structures being created on the suction side of wind turbine airfoil for three angles of attack.

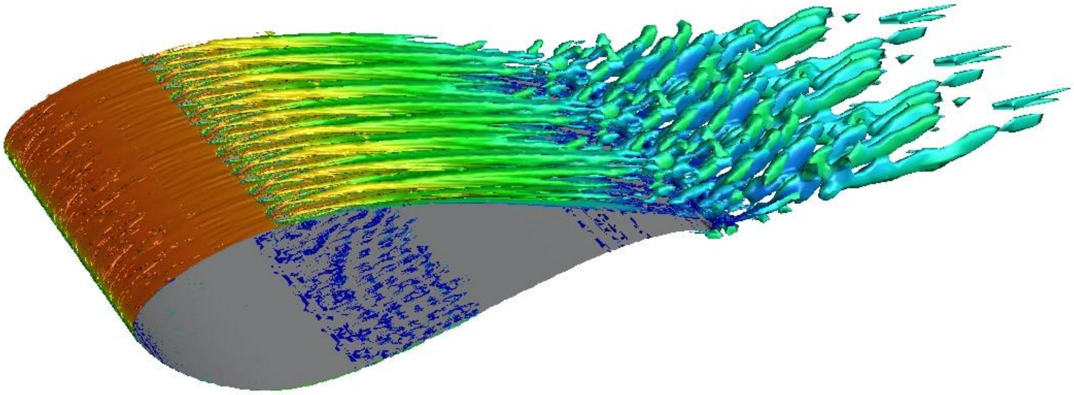

$\alpha = 11.317^0$

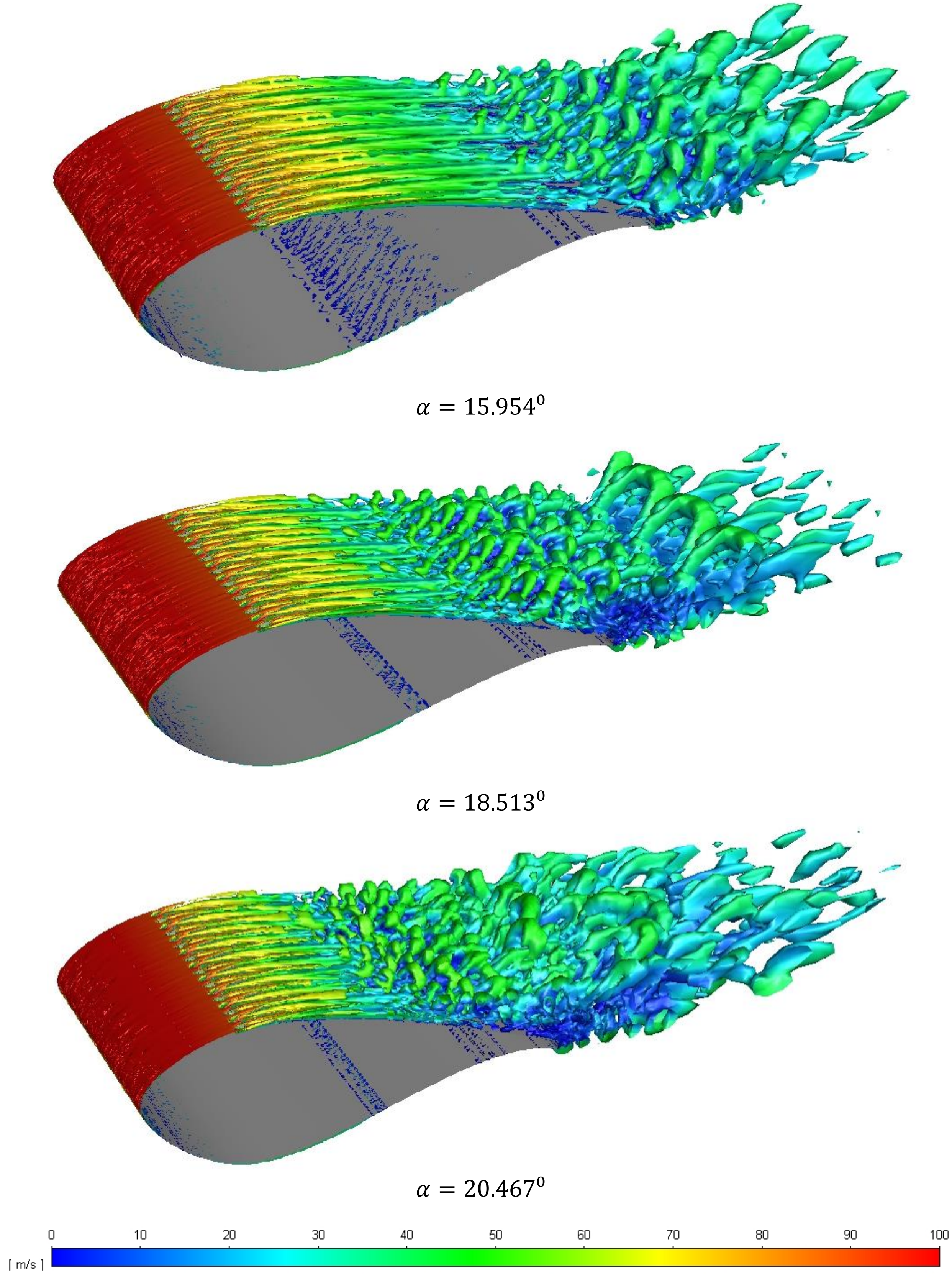

$\alpha = 15.954^0$

$\alpha = 18.513^0$

$\alpha = 20.467^0$

Figure 7.8 : Comparison of turbulent structures created on iso – surface of Q – criterion at three different angles of attack

Four different AoA are depicted in figure 7.8 making possible to visualize the evolution of flow separation and enlargement of turbulent structures. At angle 11.317º (start of non – linear region of the lift curve) flow separation takes place mainly from trailing edge, as well as from the rear portion of suction side by a small margin. Vortex tubes originating from VGs are easily noticed and follow the airfoil contour for the majority of suction side length. Situation slightly changes for 15.954º where the separation has slightly increased and separation line has moved closer to frontal part. Critical angle features significant turbulent structures separating from the surface, however, the persistence of vortices generated by passive control devices is evident, as vortex tubes remain firmly attached to the surface keeping the same flow direction as before. Angle of attack 20.467º is indicative of mild – stall region, however, mitigation of flow separation is evident here as well, despite large masses of airflow detaching from the airfoil surface.

Additionally, it is possible to compare turbulent structures generated by two different VG configurations in different regimes. In particular, angles of 16º and 20º are considered for inspection of different flow behavior with delta vanes in CtR – CU arrangement in fully turbulent [31] and cropped – delta vanes in CtR – CD arrangement in free transition regime. It is evident that common – downwash cropped – delta VGs are more effective at re – – energizing boundary layer and postponing massive flow separation during airfoil stall. Turbulence structures are smaller, detach at further distance and take lower streamwise trajectories (figures 7.9 and 7.10).

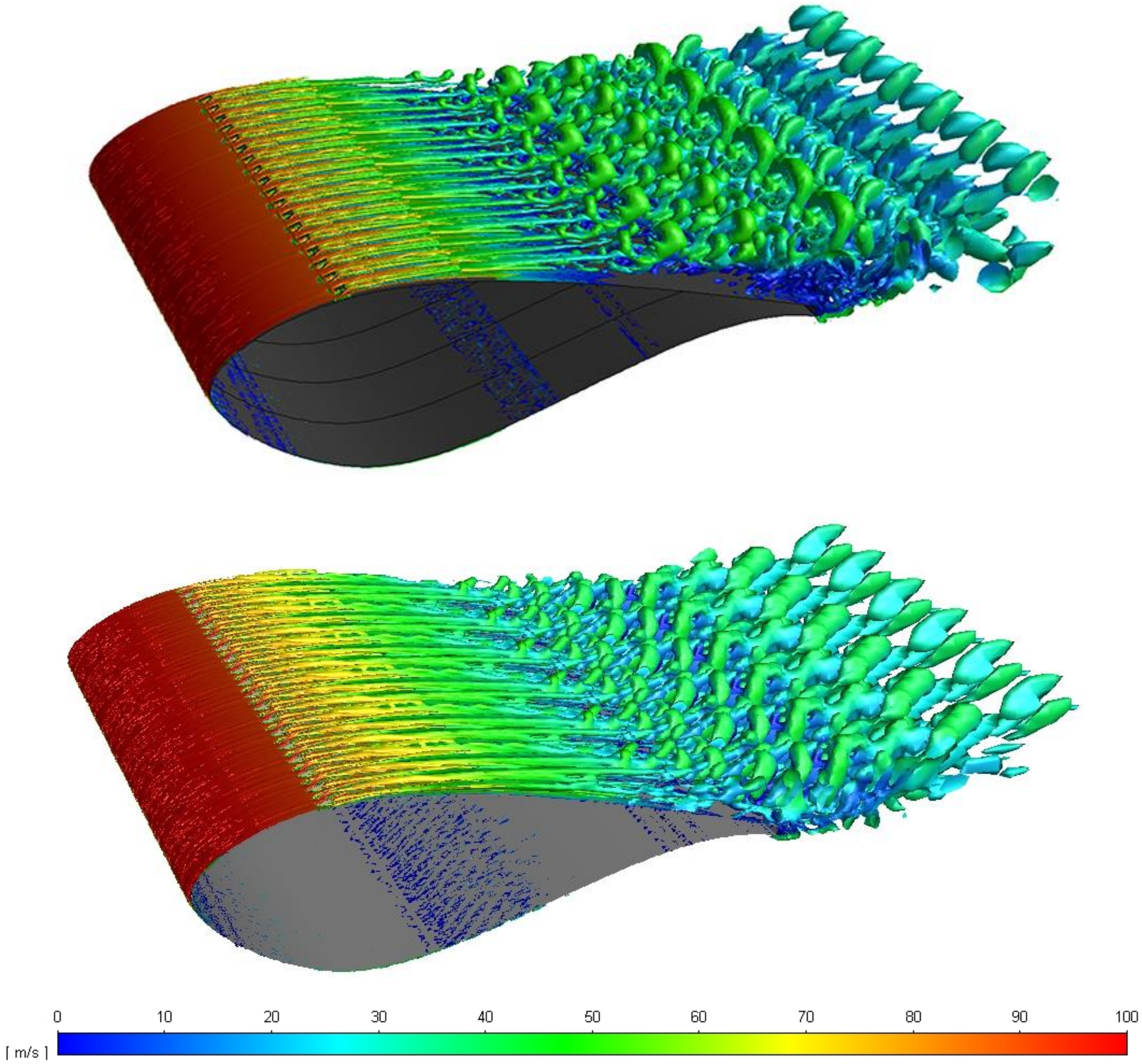

Figure 7.9 : Comparison of turbulent structures along airfoil suction side between CtR – CU delta VGs in fully turbulent [31] and CtR – CD cropped – delta VGs in free transition regime at $\alpha = 16^0$

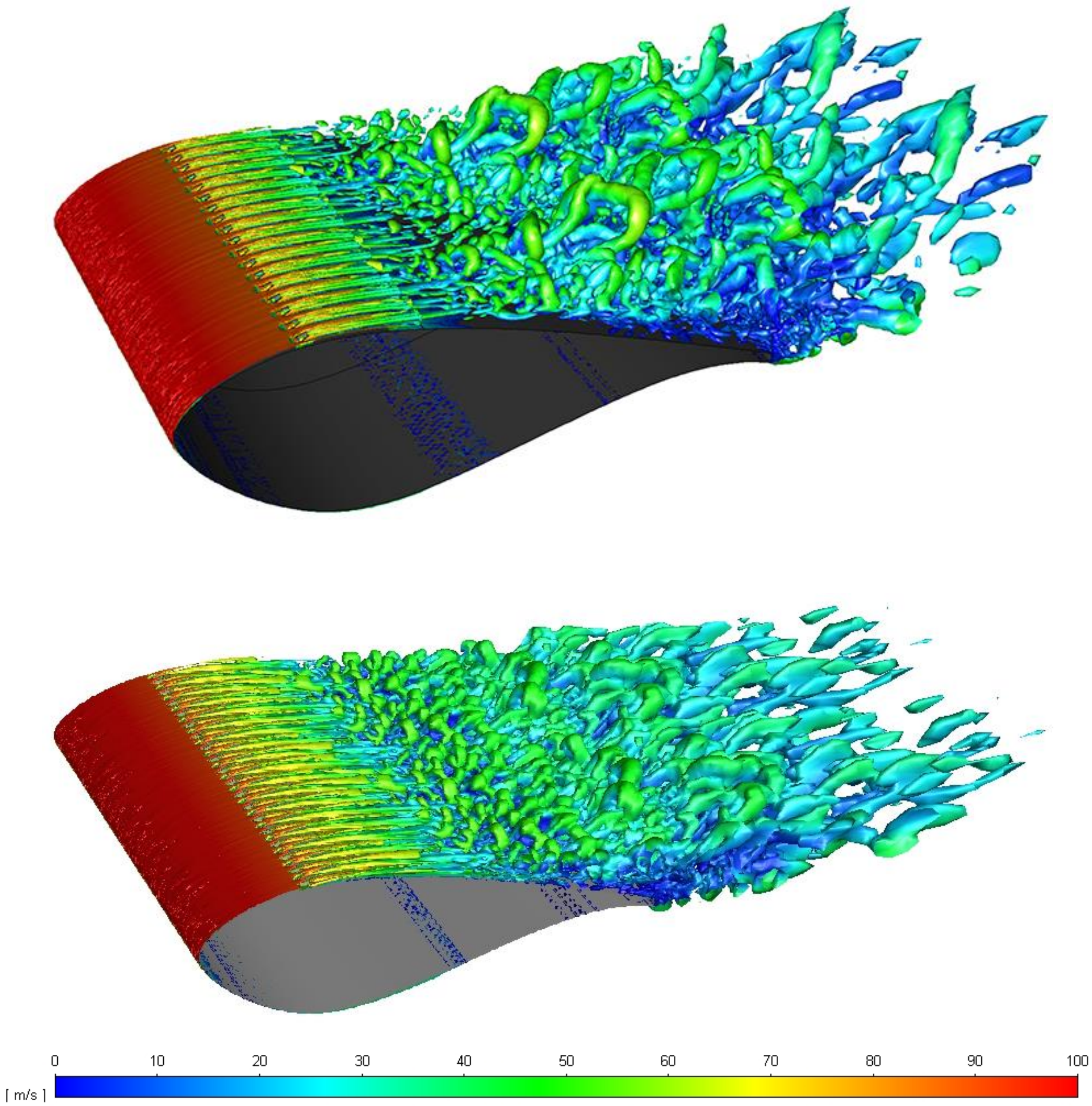

Figure 7.10 : Comparison of turbulent structures along airfoil suction side between CtR – CU delta VGs in fully turbulent [31] and CtR – CD cropped – delta VGs in free transition regime at $\alpha = 20^o$

Conclusion

Current trend in wind energy sector shows serious growth that is very clearly observed in growing tendency of wind turbine dimensions. Elongation of turbine blades unavoidably leads to bigger segments with problematic aerodynamic performance, which translates into insufficient torque that spins the rotor and lower power output. Solution is sought in flow control strategy, where two major approaches exist. Active control devices present the most concrete improvements in blade performance, however, they require energy source with controlling mechanism that is complex to integrate as well as maintain. Passive control devices avoid problems with blade integration, they are simply positioned on turbine blade even after assembly stage and require significantly less maintenance effort. Therefore, overall cost – effectiveness of passive devices is a big driving force behind extensive studies on different separation control concepts. One such concept was introduced in late 1940s and has experienced more than fifty years of research and development – vortex generator.

Vortex generator exists in many different geometrical figures and shapes. Vane vortex generator has been established as the most viable option that is relatively simple to manufacture and install on the blade and features no secondary flows that pose detrimental effect on the controlled flow. Parasitic drag of vane vortex generators does require attention, but in case of aerodynamic surfaces (wind turbine blade or aircraft wing) vanes are organized into arrays and their height is comparable to boundary layer thickness. These low – profile vortex generators do not represent any significant parasitic drag, but require the separation line to be predominantly fixed at a given angle of attack. Vane vortex generators also come in several different forms and the most common are triangular or delta, trapezoidal or cropped – delta and rectangular vane. Recently, the concept of aerodynamically shaped vortex generators has emerged, but hasn't been sufficiently explored yet and classically shaped vanes remain the preferred choice for passive flow control on aerodynamic surfaces. Experimental studies show that cropped– – delta vane vortex generators in counter – rotating, common – downwash array are the most effective solution for separation mitigation and stall delay of airfoil DU 97 – W – 300.

Scale – Resolving Simulations are versatile numerical tool for analyses of peculiar flow physics, such as considerable flow separation at high angles of attack. In fact, recent studies showed that Shielded Detached Eddy Simulation is a reliable turbulence method in case of thick airfoils equipped with vortex generators, opposed to widely – used RANS approach that gives drastic errors for aerodynamic coefficients. Hence, employed solution technique was Shielded Detached Eddy Simulation, alongside Transition SST model for flow simulations at lower angles and $k - \omega$ SST model for critical and higher angles of attack that fall within mild – stall region. Adopted computational domain is an O – type mesh, which includes fully resolved approach with non – conformal mesh interfaces in order to limit mesh refinement to the vicinity of vortex generators.

Scale – Resolving Simulation of airflow around wind turbine airfoil equipped with cropped – delta vane VGs provided sufficiently accurate results for lift coefficient. The results are satisfying particularly for pre – critical and critical angles where the relative error doesn't exceed 5 %. For post – critical angles several sensitivity analyses on grid span were necessary to perform. The analyses provided acceptable results for 19.512^{o} and 20.467^{o} with aspect ratios 0.215 (four VG pairs) and 0.48 (nine VG pairs), respectively, while at angle 21.443^{o} it was impossible to obtain reasonably accurate values. Nonetheless, sensitivity analyses demonstrated a decreasing trend of relative lift error for different aspect ratios. Slightly higher error at 6.167^{o} suggests that SRS approach and O – grid should be mainly focused on the portion of lift curve with higher angles of attack (i.e. above 11^{o} for present case).

On the other hand, the adopted SRS method and computational grid have not been able to provide drag coefficient values of similar accuracy as lift coefficient. Relative errors range from 34% at lower angles to -34 % at higher angles of attack. However, given the fact that lift coefficient is decently simulated, it is worth discussing that SDES in conjunction with Transition SST and $k-\omega$ SST models is capable of predicting correct pressure distribution, but fails when predicting skin friction. The same problem is also found in the work of Passoni [31], however, author showed that pressure coefficient distribution on pressure and suction sides very well follows the distribution obtained in wind tunnel. Unfortunately, experimental pressure coefficient distributions for present VG configuration are not available and the same comparison could not be performed. Sensitivity analyses on grid span gave decreasing trends for relative drag coefficient error as well.

Overall, SRS method again proved to be highly capable numerical tool for predicting correct airflow around thick airfoil equipped with vane vortex generators. Some future work might focus on simulating the same airfoil with the optimal VG configuration (again with cropped – delta vanes), both in free transition and fully turbulent conditions. Alternatively, more advanced research should consider numerical simulation around aerodynamically shaped cropped – delta vortex generators. However, such process may require serious adjustments to current mesh and chosen turbulence model, hence, it should be subject of a wider research project.

Appendix A

Experimental results from ,,Experimental Study on the Wake Characteristics of Vane – Type Vortex Generators in a Flat Plate Turbulent Boundary Layer” by Ho – Joon Shim, Ki – Jung Kwon and Seung – O Park

The formation of the streamwise vortex is clearly seen in figure B1. Vane pressure side corresponds to positive x coordinates, so rotational direction of streamwise vortex is counter – clockwise. The flow is swept upward in the pressure side region and downward in the suction side resulting in greater streamwise mean velocity in the suction side region.

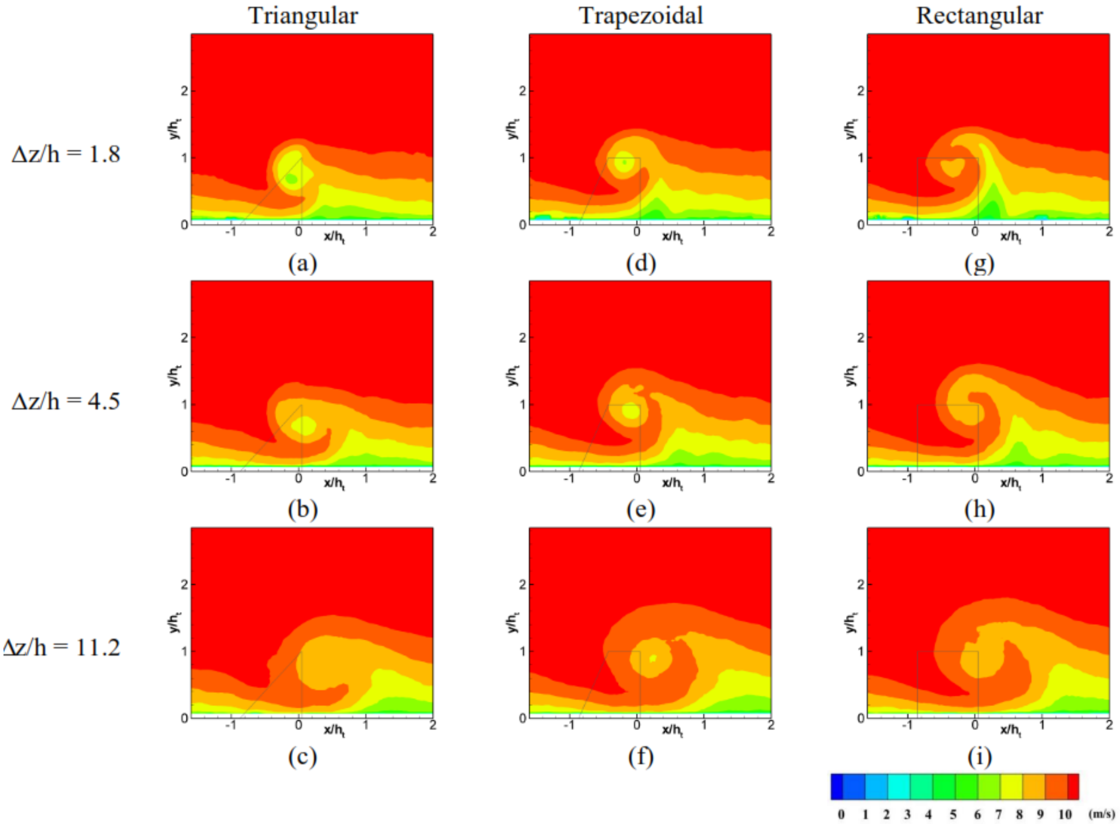

Figure A.1 : Mean streamwise velocity contours ($h/\delta = 1.0$, $l/h = 5$, $\beta = 10°$)

Table A.1 lists the streamwise peak vorticities of the three shapes of vortex generator at $\triangle z/h = 1.8$ (α stands for inflow angle that is elsewhere denoted as β), while figure A.2 shows peak vorticities downstream of the vane, divided by the peak vorticity at $\triangle z/h = 1.8$. Thus, streamwise vorticity distribution or vortex decay rate is also provided.

Length	α (deg.)	Triangular	Trapezoidal	Rectangular
l/h = 2	10	2044.9	1929.4	5062.7
	15	2739.9	2496.3	5455.3
	20	2740.7	2356.0	2903.2
l/h = 5	10	2831.2	3330.1	4451.0
	15	4711.5	6195.5	5821.4
	20	7158.8	5754.1	5705.7

Table A.1 : Peak vorticity of three basic vane VGs at $\triangle z/h = 1.8$ for the turbulent case

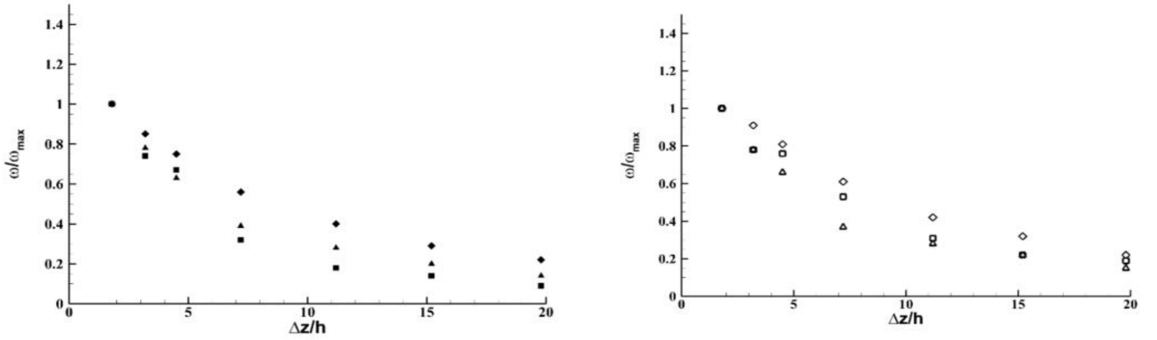

(a) l/h = 2 and α = 10 deg.

(d) l/h = 5 and α = 10 deg.

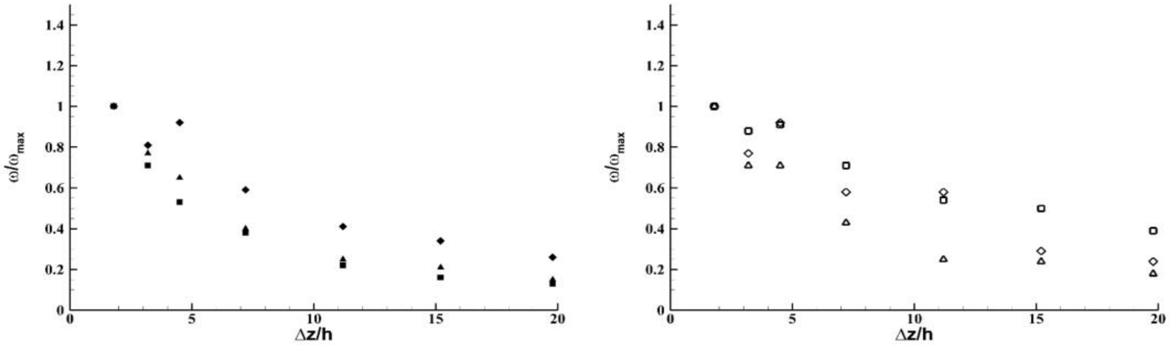

(b) l/h = 2 and α = 15 deg.

(e) l/h = 5 and α = 15 deg.

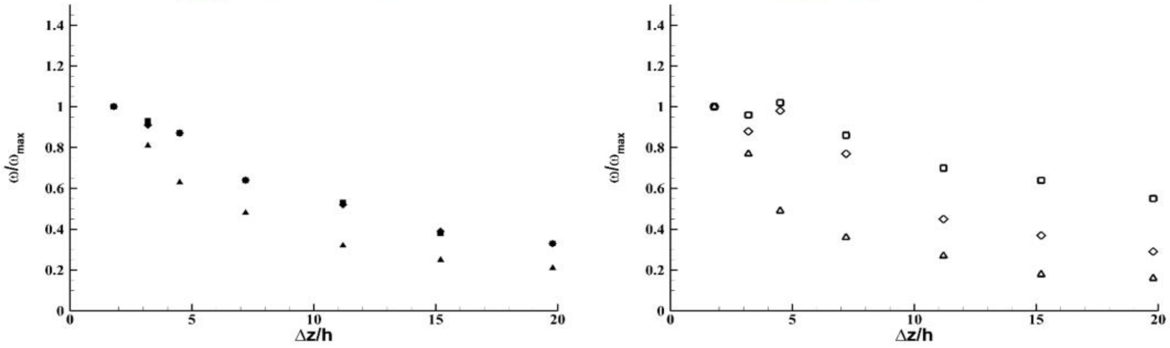

(c) l/h = 2 and α = 20 deg.

(f) l/h = 5 and α = 20 deg.

Figure A.2 : Peak vorticity variations of primary vortex of three shapes of vortex generator for turbulent flow case (▲: triangular, ◆: trapezoidal, □ : rectangular generator for $l/h = 2$; △ : triangular, ◇ : trapezoidal and □ : rectangular generator for $l/h = 5$)

Figure A.3 shows lateral and vertical path of vortex center for several values of relative length and inflow angle. Lateral position is observed by referring to vane trailing edge location. Positive Δx denotes the distance in direction of vane pressure side.

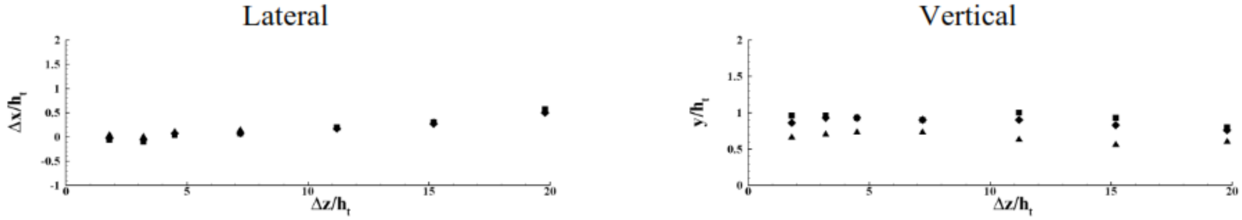

(a) lateral path; l/h = 2, α = 10° (b) vertical path; l/h = 2, α = 10°

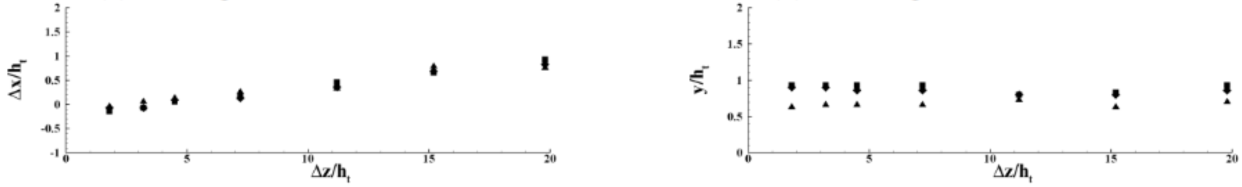

(c) lateral path; l/h = 2, α = 15° (d) vertical path; l/h = 2, α = 15°

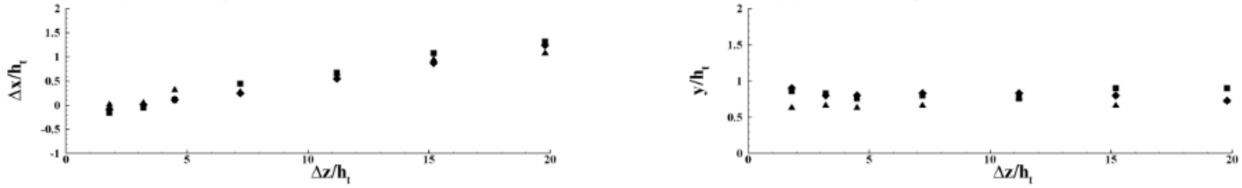

(e) lateral path; l/h = 2, α = 20° (f) vertical path; l/h = 2, α = 20°

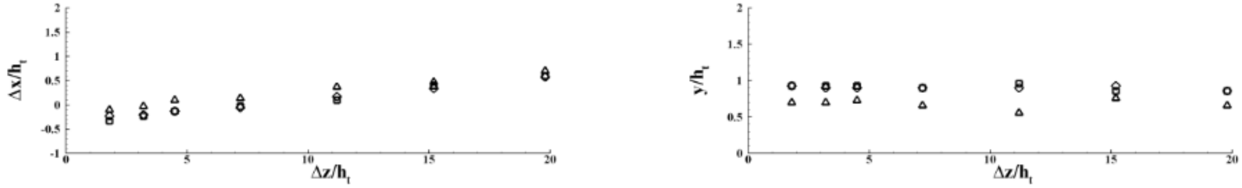

(g) lateral path; l/h = 5, α = 10° (h) vertical path; l/h = 5, α = 10°

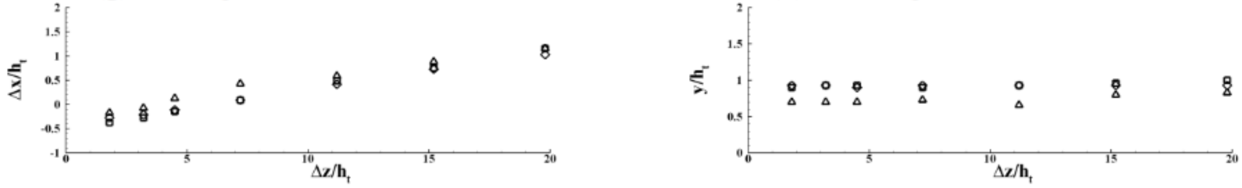

(i) lateral path; l/h = 5, α = 15° (j) vertical path; l/h = 5, α = 15°

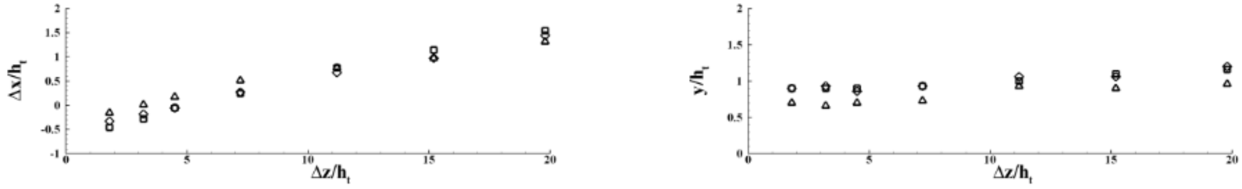

(k) lateral path; l/h = 5, α = 20° (l) vertical path; l/h = 5, α = 20°

Figure A.3 : Lateral and vertical paths of vortex center (Δ : triangular, ◇ : trapezoidal and □ : rectangular vane vortex generator)

Appendix B

Wind turbine airfoil sensitivity to different VG parameters

In the following page, lift and drag coefficients of controlled airflow of airfoil DU 97 – W – 300 are presented and sensitivity to following parameters of vane vortex generators is provided :

- vane inflow angle
- vane length
- vane planform geometry
- array configuration
- inter – vane spacing

The graphs are extracted from ,,Experimental parameter study for passive vortex generators on a 30% thick airfoil” by Baldacchino et al. [25].

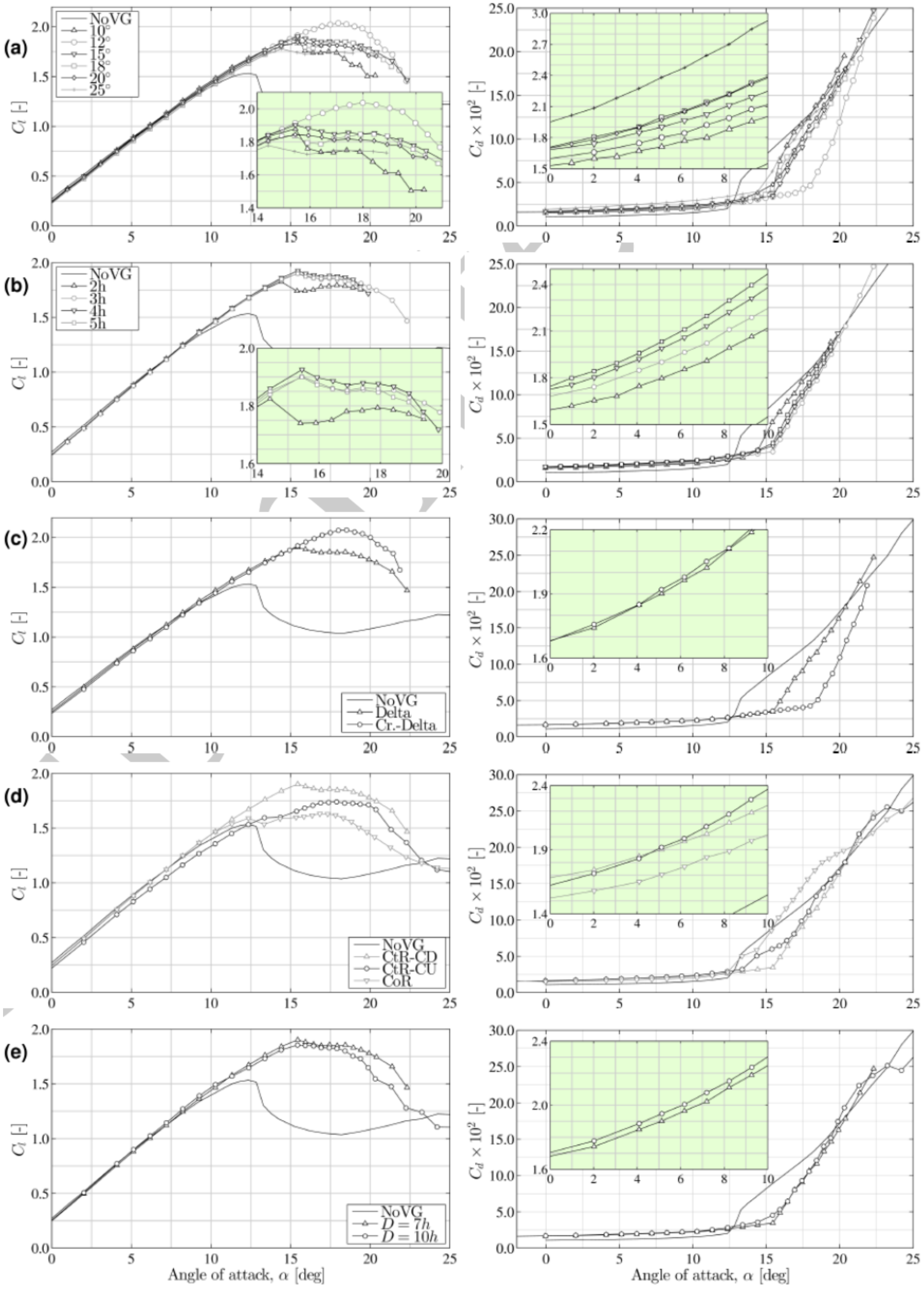

Figure B.1 : Airfoil performance sensitivity to parameters of vane vortex generators

Appendix C

Experimental data for case 038 in ,,Experimental parameter study for passive vortex generators on a thick airfoil" by D.Baldacchino and C.Ferreira

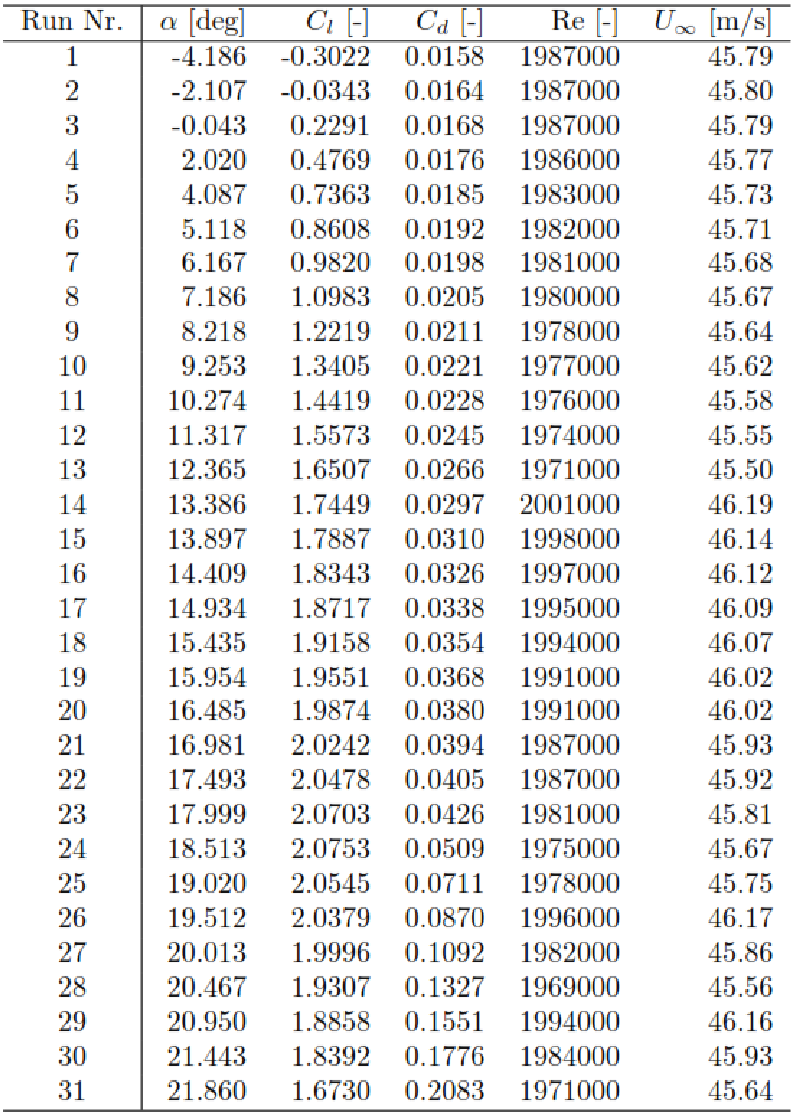

Run Nr.	α [deg]	C_l [-]	C_d [-]	Re [-]	U_∞ [m/s]
1	-4.186	-0.3022	0.0158	1987000	45.79
2	-2.107	-0.0343	0.0164	1987000	45.80
3	-0.043	0.2291	0.0168	1987000	45.79
4	2.020	0.4769	0.0176	1986000	45.77
5	4.087	0.7363	0.0185	1983000	45.73
6	5.118	0.8608	0.0192	1982000	45.71
7	6.167	0.9820	0.0198	1981000	45.68
8	7.186	1.0983	0.0205	1980000	45.67
9	8.218	1.2219	0.0211	1978000	45.64
10	9.253	1.3405	0.0221	1977000	45.62
11	10.274	1.4419	0.0228	1976000	45.58
12	11.317	1.5573	0.0245	1974000	45.55
13	12.365	1.6507	0.0266	1971000	45.50
14	13.386	1.7449	0.0297	2001000	46.19
15	13.897	1.7887	0.0310	1998000	46.14
16	14.409	1.8343	0.0326	1997000	46.12
17	14.934	1.8717	0.0338	1995000	46.09
18	15.435	1.9158	0.0354	1994000	46.07
19	15.954	1.9551	0.0368	1991000	46.02
20	16.485	1.9874	0.0380	1991000	46.02
21	16.981	2.0242	0.0394	1987000	45.93
22	17.493	2.0478	0.0405	1987000	45.92
23	17.999	2.0703	0.0426	1981000	45.81
24	18.513	2.0753	0.0509	1975000	45.67
25	19.020	2.0545	0.0711	1978000	45.75
26	19.512	2.0379	0.0870	1996000	46.17
27	20.013	1.9996	0.1092	1982000	45.86
28	20.467	1.9307	0.1327	1969000	45.56
29	20.950	1.8858	0.1551	1994000	46.16
30	21.443	1.8392	0.1776	1984000	45.93
31	21.860	1.6730	0.2083	1971000	45.64

Table C.1 : Experimental data corresponding to airfoil equipped with cropped – delta vane vortex generators of h = 5mm at 20% c in condition of free boundary layer transition

References

[1] U.S. Energy Information Administration, *International Energy Outlook 2019 with projections to 2050*, September 2019 (cit. on p. 1)

[2] J.D.Anderson, Jr, *Fundamentals of Aerodynamics*, 5th edition, 2011 (cit. on pp. 5, 6, 8, 9, 10)

[3] C.Crnojević, *Mehanika fluida*, Mašinski fakultet Univerziteta u Beogradu, 2014 (cit. on pp. 7, 8, 9)

[4] E.L.Houghton et al., Aerodynamics for Engineering Students, 6th edition, 2013 (cit. on pp. 10, 19)

[5] R. M. Wood, *A Discussion of Aerodynamic Control Effectors (ACEs) for Unmanned Air Vehicles (UAVs)*, AIAA's 1st Technical Conference and Workshop on Unmanned Aerospace Vehicles, May 2002

[6] S.J. Johnson et al., *Active Load Control Techniques for Wind Turbines*, Sandia Report, August 2008 (cit. on pp. 12, 13, 14)

[7] G.P.Corten, *Vortex blades*, oral presentation, WindPower 2007, 2007 (cit. on p. 14)

[8] G.Pechlivanoglou, *Passive and active flow control solutions for wind turbine blades*, Dissertation, Technische Universitat Berlin, 2013 (cit. on pp. 15, 16, 18)

[9] I. Aramendia et al., Chapter 21 : *Flow Control Devices for Wind Turbines*, Lecture Notes in Energy 37, 2017 (cit. on 16, 17)

[10] H.D.Taylor, *The elimination of diffuser separation by vortex generators*, United Aircraft Corporation Report No. R – 4012 – 3, June 1947

[11] J.C.Lin, Review of research on low – profile vortex generators to control boundary – – layer separation, Progress in Aerospace Sciences 38 (2002) 389 – 420, 2002 (cit. on pp. 20, 21, 26, 27, 28, 29)

[12] D.J.R.Tucker, *An Experimental Study of Hemispherical Vortex Generators for Separation Control over a NACA – 0012*, Master Thesis, University of Tennessee, 2013 (cit. on p. 24)

[13] J.Martinez Suarez et al., Streamwise vortex generator for separation reduction on wind turbine profile, Journal of Physics : Conference Series 760 (2016) 012018, 2016 (cit. on p. 25)

[14] H.H.Pearcey, *Shock – induced separation and its prevention by design and boundary layer control*, 1961 (cit. on pp. 25, 31)

[15] G.Godard and M.Stanislas, *Control of a decelerating boundary layer. Part 1 : Optimization of passive vortex generators*, Aerospace Science and Technology 10 (2006) 181 – 191, January 2006 (cit. on pp. 29, 30, 33)

[16] L.Zhang et al., *Effects of vortex generators on aerodynamic performance of thick wind turbine airfoils*, Journal of Wind Engineering and Industrial Aerodynamics, August 2016 (cit. on p. 32)

[17] H.J.Shim et al., *Experimental Study on the Wake Characteristics of Vane – Type Vortex Generators in a Flat Plate Turbulent Boundary Layer*, Recent Advances In Fluid Mechanics and Thermal Engineering, September 2015 (cit. on pp. 33, 34)

[18] J.Katz and F.Morey, *Aerodynamics of Large – Scale Vortex Generator in Ground Effect*, Journal of Fluids Engineering, July 2008 (cit. on p. 36)

[19] M.O.L.Hansen et al., *Aerodynamically shaped vortex generators*, Wind Energy, March 2015 (cit. on p. 37)

[20] O.M.Fouatih et al., *Design optimization of the aerodynamic passive flow control on NACA 4415 airfoil using vortex generators*, European Journal of Mechanics B/Fluids, 2015 (cit. on p. 40)

[21] C.Bak et al., *Wind tunnel tests of an airfoil with 18 % relative thickness equipped with vortex generators*, The Science of Making Torque from Wind (TORQUE 2018), 2018 (cit. on p. 40)

[22] H.Mueller – Vahl et al., *Vortex Generators for Wind Turbine Blades : A Combined Wind Tunnel and Wind Turbine Parametric Study*, Proceedings of ASME Turbo Expo 2012, June 2012 (cit. on p. 40)

[23] H.Wang et al., *Flow control on the NREL S809 wind turbine airfoil using vortex generators*, Energy, November 2016 (cit. on p. 40)

[24] C.M.Velte et al., *Evaluation of the Performance of Vortex Generators on the DU 91 – W2 – 250 Profile using Stereoscopic PIV*, June 2009 (cit. on p. 40)

[25] D.Baldacchino et al., *Experimental parameter study for passive vortex generators on a 30 % thick airfoil*, Faculty of Aerospace Engineering, Delft University of Technology, 2017 (cit. on pp. 40, 43, 44, 45)

[26] N.N.Sorensen et al., Prediction of the Effect of Vortex Generators on Airfoil Performance, Journal of Physics : Conference Series, 2014 (cit. on p. 40)

[27] D.Baldacchino and C.Ferreira, *Experimental parameter study for passive vortex generators on a thick airfoil*, Faculty of Aerospace Engineering, Delft University of Technology, March 2017

[28] H.K.Versteeg and W.Malalasekera, *An Introduction to Computational Fluid Dynamics: The Finite Volume Method*, 2nd edition, Pearson Education, 2007 (cit. on pp. 49, 50, 51, 52, 59, 60)

[29] F.R.Menter, *Best Practice : Scale – Resolving Simulations in ANSYS CFD*, ANSYS Germany GmbH, November 2015 (cit. on pp. 54, 55, 56, 57)

[30] A.Mosca, *CFD analysis of aerodynamic performance for wind turbine airfoils equipped with vortex generators*, Master thesis, Politecnico di Milano, April 2018 (cit. on p. 46)

[31] S.Passoni, *Scale – resolving CFD modeling of wind turbine airfoil with application of vortex generators*, Master thesis, Politecnico di Milano, April 2019

[32] M.Manolesos and J.Prospathopoulos, *CFD and experimental database of flow devices, comparison*, AVATAR Project, Task 3.1 report, February 2015

[33] D.Baldacchino et al., *Experimental benchmark and code validation for airfoils equipped with passive vortex generators*, Journal of Physics : Conference Series 753, September 2016

[34] A.Garbaruk et al., *Evaluation of Time Sample and Span Size Effects in DES of Nominally 2D Airfoils beyond Stall*, Progress in Hybrid RANS – LES Modeling, 2010

[35] H.Y.Xu et al., *Delayed detached eddy simulation of the wind turbine airfoil S809 for angles of attack up to 90 degrees*, Energy 118, 2017

[36] P.R.Ashill et al., *A review of recent developments in flow control*, The Aeronautical Journal, May 2005 (cit. on pp. 10)

[37] ANSYS Fluent Theory Guide, Release 19.0, *4.6.2 Transport Equations for the Transition SST Model*, January 2018 (cit. on p. 53)

[38] F.Inzoli, *Lecture 5 : Geometrical discretisation*, CFD for Energy Engineering, Department of Energy, Politecnico di Milano, 2017 (cit. on pp. 65, 66)

[39] M.Dodić and B.Krstić, *Teorija letenja. Metodički priručnik – rod avijacija*, Univerzitet odbrane, Vojna akademija, 2015 (cit. on p. 11)